PAIRWISE COULOMB INTERACTIONS IN DIVERGING ELECTRON AND ION BEAMS

Dale Lennart Larson
B.A., State University of New York at Plattsburgh, 1975

A dissertation submitted to the faculty
of the Oregon Graduate Center
in partial fulfillment of the
requirements for the degree
Doctor of Philosophy
in
Applied Physics

December, 1982

Errata

Dale L. Larson

Pairwise Coulomb Interactions in Diverging Electron and Ion Beams

Correct graduation date is October 1986.

Information from abstract page.

The dissertation "Pairwise Coulomb Interactions in Diverging Electron and Ion Beams" by Dale Lennart Larson has been examined and approved by the following Examination Committee:

Lynwood W. Swanson, Thesis Advisor

Paul R. Davis

Jon H. Orloff

James J. Huntzicker

The author acknowledges with pleasure his indebtedness to Professor Lynwood W. Swanson for his encouragement and untiring patience, as well as his academic expertise. Grateful acknowledgement is also given to the faculty and staff of the Oregon Graduate Center for their efforts on my behalf.

This dissertation is dedicated to the memory of my father,

Einar K. Larson

TABLE OF CONTENTS

1. Introduction 1

2. Review of Literature 5

2.1 Sommerfeld Free Electron Theory 5

2.2 Experimental TED Measurements for Electrons 7

2.2.1 The Energy Analyzer 7

2.2.2 TED Measurements 8

2.3 Experimental TED Measurements for Ions 10

2.4 Energy Broadening Mechanisms 12

2.4.1 Internal Broadening Mechanisms 13

2.4.2 External Broadening Mechanisms 13

3. The Pairwise Model 20

3.1 Introduction 20

3.2 Particle Equations of Motion 25

3.3 Electric Field Models 30

3.4 Energy Integrals 39

4. Numerical Methods 44

4.1 Introduction 44

4.2 The Runge-Kutta Algorithm 44

4.3 Integration Using a Cubic Spline Algorithm 48
4.4 Difficulties in Using the Numerical Methods 52
5. Presentation of Model Data 57
5.1 Introduction 57
5.2 Sphere Model Studies 61
5.2.1 Energy Broadening Studies 62
5.2.2 Average Energy Shift Studies 69
5.3 SOC Model Studies I: Colinear Emission 73
5.3.1 Energy Broadening Studies 77
5.3.2 Average Energy Shift Studies 84
5.4 SOC Model Studies II: Non-Colinear Emission 90
6. Results and Discussion 98
6.1 Introduction 98
6.2 Sphere Model Results 99
6.2.1 Energy Broadening Results 99
6.2.2 Energy Shift Results 102
6.2.3 Comparisons with Experimental Data 103
6.3 SOC Model Results 110
6.3.1 Energy Broadening Results 112
6.3.2 Energy Shift Results 113
6.3.3 Comparisons with Experimental Data 115
6.4 SOC Model Non-Colinear Results 119
6.5 Summary 120
References 123

Appendix 126

Biographical Note 130

LIST OF FIGURES

1. Spherical Emitter Model. 21

2. Sphere on Orthogonal Cone (SOC) Model. 22

3. Geometry of the SOC Model. 27

4. Components of Energy Spread. 43

5. Emitter Profiles. 60

6. Sphere Model Electron Energy Spread vs. Distance. 63

7. Sphere Model Electron Energy Spread vs. Emitter Radius. 64

8. Sphere Model Electron Energy Spread vs. Field Strength. 65

9. Sphere Model Ga^+ Energy Spread vs. Distance. 66

10. Sphere Model Ga^+ Energy Spread vs. Emitter Radius. 67

11. Sphere Model Ga^+ Energy Spread vs. Field Strength. 68

12. Sphere Model Energy Spread vs. Ionic Mass. 70

13. Sphere Model Energy Spread vs. Charge. 71

14. Sphere Model Energy Shift vs. Distance. 72

15. Sphere Model Electon Energy Shift vs. Field Strength. 74

16. Sphere Model Energy Shift vs. Ionic Mass. 75

17. Sphere Model Energy Shift vs. Charge. 76

18. SOC Model Electron Energy Spread vs. Distance. 78

19. SOC Model Electron Energy Spread vs. Emitter Radius. 79

20. SOC Model Electron Energy Spread vs. Field Strength. 80

21. SOC Model Ga^+ Energy Spread vs. Distance. 81

22. SOC Model Ga^+ Energy Spread vs. Emitter Radius. 82

23. SOC Model Ga^+ Energy Spread vs. Field Strength. 83

24. SOC Model Energy Spread vs. Ionic Mass. 85

25. SOC Model Energy Spread vs. Charge. 86

26. SOC Model Energy Shift vs. Distance. 87

27. SOC Model Electon Energy Shift vs. Field Strength. 88

28. SOC Model Energy Shift vs. Ionic Mass. 89

29. SOC Model Energy Shift vs. τ_0. 91

30. SOC Model Energy Shift vs. δ_0. 92

31. SOC Model Energy Spread vs. Emission Angle. 94

32. SOC Model Energy Shift vs. Emission Angle. 95

33. SOC Model Angular Spread vs. Emission Angle. 96

34. Experimental Energy Spread vs. Field Factor. 104

35. Experimental Energy Spread vs. Field Strength. 106

36. Experimental Energy Spread (Singly Charged) vs. Mass. 107

37. Experimental Energy Spread (Doubly Charged) vs. Mass. 108

38. Corrected Experimental vs. Sphere Model Predicted Energy Spread. 109

39. Electron Collision Regimes. 117

40. Experimental Energy Shift vs. Mass. 118

41. Experimental Angular Spread vs. Mass. 121

ABSTRACT

Pairwise Coulomb Interactions in Diverging Electron and Ion Sources

Dale Lennart Larson, Ph. D.
Oregon Graduate Center, 1986

Supervising Professor: Lynwood Swanson

The formation of high intensity electron beams by means of field emission is well known. Recently, high intensity ion beams have been formed by the application of electric fields of the order of 1 to 5V/Å to liquid metal surfaces. Intensities of greater than 20μA/sr have been reported for various metals such as gallium, indium, aluminum and bismuth. In focused beam applications such as scanning microscopy, inspection and testing, ion implantation and mask repair, the energy broadening and angular beam spreading are important parameters which impose fundamental limits on the focused spot size. These parameters depend on both deterministic and randomly produced forces, as well as upon the geometry of the beam. The purpose of this investigation is to study the energy exchange and trajectory perturbations attending the Coulomb interaction between a pair of electrons or ions which happen, by random fluctuation in the emission process to be in close proximity to

each other.

To this end, a numerical solution of the equations of motion of the particles moving in the external field of an emitter was performed. Two emitter field models were studied: the field produced by a spherical conductor, and the field produced by a conducting sphere whose center is at the apex of a conducting cone. By suitable choices of cone half-angle and sphere radius, an equipotential can be found whose shape closely approximates either a solid field electron emitter or the surface of a liquid metal ion source. Emitter radii r_a from 10^2 to 10^4 Å and emitter field strengths F_0 from 0.01 to 1.0 V/Å were examined.

The influence of initial relative position, particle mass m and charge n on the energy and trajectory broadening was investigated for electrons and the ionic species Li^+, Al^+, Ga^+, Bi^+, Bi^{+2} and Bi^{+3}. Relationships between the time spacing between emission events and other parameters of interest were obtained. The sphere model was found to predict the following dependencies for the energy spread:

$$\Delta E \propto I^{1/2} (m r_a F_0)^{1/4} n^{3/4}$$

where I is the total current. The SOC model was found to predict the same current and mass dependencies, but a more complex relationship for emitter radius, field strength and charge was obtained. The functional relationship for these parameters depends on the emitter shape and on the current.

A mechanism for the observed shift in peak energy was also found in these studies: the conversion of the initial Coulomb potential energy between the pair into kinetic energy.

In summary, the pairwise Coulomb interaction is able to produce energy and angular beam spreading of the magnitude observed in electron and LMIS experimental data, even in the absence of beam crossovers.

CHAPTER ONE

Introduction

The formation of high intensity electron beams by means of field emission is well known. Recently, high intensity ion beams have been formed by the application of electric fields of the order of 1 to 5 V/Å to liquid metal surfaces. Ion emission has been obtained from liquid gallium, cesium, indium, bismuth, gold, tin, silver, lead, aluminum, mercury, silicon, germanium, uranium, platinum and iron.[1-4] In some cases low melting point alloys have been used as a source for several ionic species. Intensities of greater than 20 μA/sr have been reported for various liquid metal ion sources (LMIS) such as gallium, indium, aluminum and bismuth from a film of the liquid metal supported by a solid needle.

In focused beam applications such as scanning microscopy, mask repair, microfabrication and ion implantation, the energy broadening and angular beam spreading are important parameters which impose fundamental limits on the focused beam size. These parameters depend on both deterministic and randomly produced forces, as well as upon the geometry of the beam. Deterministic effects are those produced by electric fields associated with the average current density distributed throughout the beam. The primary result of these fields is the expansion of the beam cross-section along the length of the beam. As shown by Massey and co-workers[5] essentially no contribution to the energy broadening is made by the distributed field which, being stationary and conservative, accelerates all particles uniformly.

Random effects include microfluctuations of the particle density which bring pairs of particles unusually close together such that their mutual Coulomb repulsion is appreciable, as well as the redistribution of the initially tangential thermal energy according to the equipartition of energy principle. Random effects contribute to both energy broadening and beam divergence. In focused beam work, random Coulomb effects occur in three regions of the beam: 1) in the acceleration region near the emitter, 2) in the field free drift region and 3) in regions containing a focal plane. Random events in Region 2 and Region 3 are collisional in nature in that the particles involved are on trajectories that happen to bring them into close proximity. In Region 1 the nearness of the particles is the result of the statistical fluctuations in the emission process. This region is also characterized by a rapidly changing external electric field which modifies the effect of the pairwise Coulomb interaction by controlling the length of time during which particles may interact. In all three regions the magnitudes of the broadening effects vary directly with the path length of the region. The effect of the accelerating field is in addition to the path length effect.

The purpose of this investigation is to study the energy exchange and trajectory perturbations attending the Coulomb interaction which occurs in Region 1 for both sphere and cone shaped emitters and to evaluate the sensitivity of these perturbations to changes in current, charge, mass, field strength and emitter radius.

To this end the equations of motion of a pair of particles moving in the external field of an emitter were derived for two diode geometries and numerical solutions for these equations were determined. The emitter models studied were the spherical conductor, and a conducting sphere whose center is at the apex of a conducting orthogonal cone (SOC). By suitable choices of cone half-angle and sphere radius, an equipotential can be found whose shape closely approximates either a solid field electron emitter, or the surface of an LMIS.

The particle parameters include their initial relative position, their initial thermal energy, their mass and charge. Trajectories for electrons and for the ionic species Li^+, Al^+, Ga^+, In^+, Bi^+, Bi^{+2} and Bi^{+3} were calculated.

The remainder of this paper is organized as follows. A chronological review of related literature is presented in Chapter 2. The model equations are derived in Chapter 3 and a discussion of the numerical methods used to solve them is presented in Chapter 4. The results of the model calculations are shown in graphical form in Chapter 5 and discussed at length in Chapter 6. A comparison of the model predictions with experimentally obtained data is also presented in Chapter 6 as well as a summary of the conclusions that may be drawn as a result of this study. A set a flow charts of the trajectory calculating program is provided as an Appendix.

CHAPTER TWO

Review of Literature

2.1 Sommerfeld Free Electron Theory

The work reported in the present paper was in large part prompted by the studies performed by Bell and Swanson[6] and others who reported anomalous broadening of the total energy distribution (TED) of field emitted electrons and very broad energy distributions for liquid metal ion sources. In the case of the electron data, the anomalies are those deviations of the experimental TED with respect to the Fowler-Nordheim theory[7] based on the Sommerfeld free-electron model as modified by Good and Müller[8] to include the effect of temperature. For the case of field ion emission there has not yet appeared an undisputed explanation of the emission process, let alone a satisfactory theory of the TED.

In a review paper by Gadzuk and Plummer[9] the historical development of the theory is presented in some detail. Summarized here are the major points of the derivation.

The TED for field emitted electrons is a measurement of a barrier penetration problem. A supply function N(E,W) describing the density of electrons within the metal incident upon the barrier with total energy E and normal energy W is multiplied by the barrier transmission probability function D(W) and integrated over all normal energies:

$$\frac{dj}{dE} = N(E,W)\ D(W)\ dW \tag{1}$$

where dj/dE is the differential change in current density with respect to energy at total energy E. The supply function is approximately equal to the product of a Fermi function

$$f(E) = \frac{1}{1+\exp[(E-E_f)/kT]} \tag{2}$$

times the arrival rate which is the normal component of the group velocity times the normal component of a density of states.

Fowler and Nordheim used a wave matching technique in their derivation of the penetration probability D(W) and later workers[10] used the WKB approximation. Others have refined the calculations of D(W) in various ways[11-16], but the result obtained by Young[17] has become the standard form of the TED:

$$\frac{df}{d\epsilon} = \frac{J_0 e^{\epsilon/d}}{d} f(\epsilon) \tag{3}$$

where

$$J_0 = \frac{4\pi med^2}{h^3}\exp[-0.683\phi^{3/2}v(y)/F]$$

$$\epsilon = E-E_f$$

$$y = 3.79F^{1/2}/\phi$$

and v(y) is a tabulated function, E_f is the Fermi energy, F is the electric field strength and ϕ is the work function.

2.2 Experimental TED Measurements for Electrons

2.2.1 The Energy Analyzer

In 1959 Young and Müller[18] described a retarding energy analyzer used to make their measurements of the TED of tungsten. Their analyzer was the first to have sufficient accuracy to record a TED. It was Young who realized in a companion paper[17] that the energy distribution being measured was a total energy distribution as opposed to a normal energy distribution as had previously been thought. In order to overcome some of the disadvantages of this analyzer, Plummer and Young[13] developed a cylindrically symmetric analyzer where the radially diverging beam is collimated beneath the imaging screen and retarded by a series of rings and a very fine flat mesh. The previous analyzer was spherically symmetric and suffered from secondary emission from the retarding elements, as well as poor sensitivity and a long time constant. Swanson and Crouser[19] modified a design of van Oostrom[20] which is spherically symmetric and employs a focusing element which creates a crossover near the center of the collector. In 1968 Young and Kuyatt[21] described a method for determining the energy resolution of a field emission energy analyzer. Lea and Gomer[22] added an electron multiplier to the

Swanson-Crouser analyzer and were able to achieve an energy resolution of about 0.030 eV, comparable to that of Plummer and Young.

2.2.2 TED Measurements

Using a thermionic cathode Börsch[23] took several energy distribution measurements and calculated the apparent source temperature from the Maxwell-Boltzmann theory which relates the width of the energy distribution to the source temperature. He used a retarding grid placed in front of a Faraday cup to obtain an integral curve. He made measurements for emitter voltages between 20 kV and 100 kV, and actual emitter temperatures from 2100°C to 3000°C as measured with an optical pyrometer. For the low temperature, low current case he found the distribution to be in agreement with the Maxwellian theory. At higher beam currents the width of the distribution broadened to approximately twice the predicted width. He found that the broadening was a function of current density and current intensity, and showed that focusing a beam increased the width of the distribution even though the emitter temperature remained constant. He concluded that there was no broadening in the acceleration region and postulated waves in the space charge field emanating from the crossover regions.

Young and Müller[18] confirmed the presence of anomalous broadening in their measurements on tungsten. They also noted that the distributions being measured were total energy distributions which for field emission are much narrower than the normal distribution which had previously been thought to be the measured spectrum. Simpson and Kuyatt[24] reported measurements on a planar thermionic emitter operating in a much better vacuum environment than previous work. Whereas Börsch, for example, was working at pressures in excess of 1.0 x 10^{-6} Torr, Simpson and Kuyatt conducted their work with a vacuum better than 1.0 x 10^{-7} Torr. They reported however, that the energy spread is independent of vacuum for the range 1.0 x 10^{-5} to 1.0 x 10^{-9} Torr. They concluded that the significant parameter is the current density rather than current and that ΔE is proportional to J and inversely proportional to the voltage. They expressed a great deal of uncertainty in these dependencies, however. The dependence on voltage was determined to be somewhere between $V^{-1/6}$ and $V^{-3/2}$ and the dependence on current density was estimated to be either J^1, $J^{1/2}$ or $J^{1/3}$.

Beck and Mahoney[25] were unable to measure the Börsch effect. Ichinokawa[26] also had trouble finding the effect, and found the theories of Börsch[23] and Löffler[27] to be unsatisfactory, asserting instead that the effect is caused by the analyzer and is not physically significant.

Lea and Gomer[28] found a high energy tail in the TED of electrons emitted from tungsten even at 20°K, clearly in the field emission domain. Gadzuk and Plummer published two papers in 1971[29,30] in which they confirm the measurements of Lea and Gomer. Also in 1971 Lea and Gomer[22] reported TED measurements from a tungsten cathode operating

In 1977 Kawasaki and coworkers[31] measured the TED for electrons emitted from a TiC single crystal and found that it also was not in accordance with the free electron theory, but rather exhibited a broadened distribution with a hump which they speculated to arise from band structure effects.

Also in 1977 Wolfe[32] noted that the Börsch effect was present even without a crossover in the electron optics. He pointed out that the acceleration region of a field emission gun was like a crossover in that the full current intensity of the beam was present in a very small cross-sectional area. Bell and Swanson[6] reported anomalous broadening of the TED at high current densities for an electron gun without a crossover. They found deviations from the free electron model at energies both above and below the Fermi energy.

In 1981 Essig and Geiger[33] studied the field electron emission from carbon fibers. At low currents on the order of 1.0 nA the measured energy spread agrees with the free electron model at room temperature. At higher currents they found broadened TEDs which they attributed to Coulomb interactions in regions of high current density in the optical system.

2.3 Experimental TED Measurements for Ions

The first measurements of the energy distribution from an LMIS were made by Krohn and Ringo[1] in 1975. They reported work on gallium, mercury and cesium. In their experimental setup, they formed a cone on a liquid surface at the end of a hollow needle by the application of an approximately spherical electrostatic field. The ions were emitted from the tip region of the cone. An interesting feature of their source was that "it was frequently necessary to tap the source with a hammer in order to start it."

Clampitt and Jeffries[2] described the use of a needle to support a liquid metal film for obtaining ion emission. They noted that the impression of an electrostatic force on a flat liquid surface leads to cusp-like filamentary protusions. Curved surfaces reduce the voltage required to produce the cusps, and can be shaped in such a way as to encourage the formation of a single cusp. In their arrangement, the needle protruded through the surface of a pool of liquid metal. They pointed out that the radius of curvature of the needle and the length of the shank protruding above the liquid surface are critical parameters, in that multiple cusp formation is to be avoided, and the length must be small enough to permit adequate viscous flow to replenish the emitting region, while long enough to avoid problems with the meniscus at the needle-pool interface. They were successful in obtaining emission from Cs, Ag, Au, Ga, In, Sn, Pb, Al, Hg, Si, Ge, U, Pt, Fe and Bi. They did not report any TED measurements.

In 1979 Seliger and coworkers[34] produced a gallium source and reported an intensity of 1.5 A/cm^2 in a 1000 Å focused spot. The following year, Swanson, Schwind and Bell[3] reported measurements of the energy and angular broadening of liquid gallium ions as functions of emission current. Their source configuration consisted of a tungsten field emitter with a cone half angle and radius of 23 ± 2° and 5 ± 2 μm respectively. A film of gallium several microns thick was coated onto the tungsten emitter. By warming the emitter above the melting point of gallium, a liquid film was produced from which a cusp could be formed by the application of an electrostatic field. They measured TED values for a variety of current and temperature conditions. Values for the full width at half maximum (FWHM) ranged from 4.5 eV for low current and temperature to about 30 eV for high current and temperature. Swanson and coworkers[35] published energy and angular broadening results for both a gallium and a bismuth LMIS. They have also been able to make similar measurements on indium and aluminum.[36]

Dixon and coworkers[4] studied the ionic emission from a tin LMIS. In this metal, multiply charged species are found in relatively great abundance. They found that the energy spread for singly charged tin ions was greater than that for doubly charged ions of the same mass, and also investigated the relationship of mass to the energy spread for diatomic species.

2.4 Energy Broadening Mechanisms

Discussion of the theories of broadening mechanisms that follows will be restricted to the case of electrons emitted from a solid cathode.

2.4.1 Internal Broadening Mechanisms

In 1970, T. Fischer[37] suggested that the high energy tail found in the field emission energy distribution was attributable to the Auger filling of holes in the Fermi gas which are produced when electrons with energy less than the Fermi energy are field emitted. Lea and Gomer[28] supported this theory which was further elaborated by Gadzuk and Plummer[29]. Later, in 1973, Gadzuk and Lucas[38] showed that the J^2 dependence of the energy spread reported by Lea and Gomer and others was not sufficient evidence to prove the multi-particle process theory. They proposed that the energy spread arises from the uncertainty in the tunneling lifetime of the electron through the surface potential barrier. They summarized four different scenarios of the tunneling which predict various lifetimes having the incredible range of 1 to 1×10^{-16} seconds. They favored an estimate on the order of 1×10^{-12} seconds and showed that the dependence on current density found experimentally for the high energy tail can be derived from the quantum mechanical uncertainty in the tunneling lifetime.

2.4.2 External Broadening Mechanisms

Börsch[23] was, of course, the first to discuss the broadened electron distribution. He found that the broadening was a function of current density and showed that focusing a beam increased the TED width even though the cathode temperature remained constant. He concluded that there was no broadening in the acceleration region, and postulated waves in the space charge field emanating from the crossover regions in the optical column.

Löffler[27] suggested that the energy spread observed by Börsch was the result of pairwise interactions at the crossover and gave an analytic treatment . He assumed that the initial axial energy spread was zero and that the axial separation between pairs of electrons remained constant. He concluded that a relaxation of the thermal energy was not needed to explain energy broadening, and that the largest contribution to the broadening was from near-neighbor interactions. His analysis predicts the following dependencies for ΔE:

$$\Delta E \propto I^{1/2} / V^{1/4} r_0 \, \alpha_0 \tag{4}$$

where r_0 is the crossover radius and α_0 is the angle of divergence. Löffler's analysis cannot be used to investigate energy spreading in a beam having no crossover, such as in a field emission electron gun (which does display energy broadening).

In 1970 Zimmerman[39] produced a general theory of the Börsch effect. He also showed that the Coulomb interaction between individual electrons (as opposed to the interaction of a test electron with the average space charge created by the surrounding electrons in the beam) is primarily responsible for the energy spread in high current electron beams. He discussed the equilibration of the transverse components of the thermal energy which, because of the acceleration by the electric field, are more significant than the axial component. Knauer[40] pointed out by way of example in this context that the compression of the axial energy spread from a cathode at 1750° K by an acceleration through 10 kV results in a thermal equivalent beam temperature of 0.35° K as compared to the transverse thermal energy which, although initially is approximately the same as the tip temperature, becomes 50,000 times greater after acceleration. In the post acceleration region the Coulomb interaction between the electrons will act to restore the equipartition of the internal energy of the electrons.

M. Fischer[41] proposed an alternate theory for the energy distribution from hot cathodes. He restricted himself to the drift region of the beam and assumed that the electrons were neutralized by a positive background of stationary ions arising from the ambient gas in the chamber. In his model the energy spread is the result of the noise fed into the beam by resistors in the circuit and from the gun itself.

Crewe published two papers[42,43] in which he criticized Löffler for his "many severe approximations" and for the reciprocal dependence on the angle of convergence of the crossover. Löffler[27] and also Zimmermann[39] had analyzed multiple small-angle scatterings. Crewe considered only single Coulomb deflections and arrived at the following expression for the energy spread:

$$\Delta E = 17.8 \frac{I}{\beta_0} \left[\frac{\alpha_0^3}{\alpha^4 + 3.14 \times 10^{-9}\, I^2/\beta_0^6} \right] \qquad (5)$$

where β_0 is the ratio of the electron velocity to the speed of light.

El-Kareh and Smither[44] developed two computer models using Monte Carlo techniques. In the first model, the beam is directed to converge to a point, and the effect of the interactions is calculated for a series of initial conditions. In the second program, an actual electron gun is simulated, and the analysis of the Börsch effect made for a diverging beam without crossover. In the first case, they found their model to be in agreement with theory in predicting the space charge effects on the beam at the crossover, and also compared their calculations with Zimmermann's theory and found reasonable agreement. Their energy broadening results were lower than Zimmermann's results because they did not include any initial thermal energy. They then proceeded with their second program to show that large amounts of spreading can occur in a gun assembly which has no crossovers.

Knauer[40] showed that "the number of large-angle deflections along the length of a typical beam is less than one per particle, while the number of small angle scattering events significantly exceeds one. Furthermore, multiple scatterings are found to be far more effective in transferring momentum." He therefore favored the approaches taken by Löffler and Zimmermann over that taken by Crewe. Knauer also showed that pairwise interactions are the dominant ones, and attempted to clarify the role of the several competing processes and indicate the types of beams and beam geometries for which they apply. He considered external mechanisms only.

In 1979 another paper using Monte Carlo simulation appeared. Groves, Hammond and Kuo[45] constructed a model of the electron beam which they described as being free of approximations. However they excluded the acceleration region of the beam, and instead assumed a uniform initial distribution of the electron energies in both the axial and transverse directions. The electrons were randomly distributed in a cone-shaped region of space, random in position and in velocity within the limits of the energy distribution. The resulting ensemble of particles was then traced through an optical system and a record made of the particle positions and energies at various locations. In this way a distribution describing the spot size and beam energy characteristics was obtained. The paper presented studies of the effect of source magnification, of mutual repulsion and of the spherical and chromatic aberrations on the spot size.

DeChambost and Hennion[46] analyzed energy broadening in the tip region and at a half-crossover, attempting to find a simple analytic relationship involving easily measured column parameters. Their result differed from experiment by a factor of two and they concluded that the statistical model chosen to represent the electron density of the beam strongly influences the resultant equation, and that differences in the statistical models chosen by various authors accounts for the disparities found in the literature. They also found that the geometry of the beam, particularly in the tip region, must be accurately represented in the calculations, in order to obtain useful results, contrary to the calculations of Groves et al.

Rose and Spehr[47] attributed the Börsch effect to statistical fluctuations in the spatial distribution of the electrons, which by means of Coulomb interactions between the particles alters the energy distribution. With small currents, there are few collisions and a non-uniform transfer of energy and this leads to a non-gaussian energy distribution. Crossovers especially favor a non-gaussian form. They pointed out that because the TED is non-gaussian, the ratio of the FWHM to the root-mean-square depends on the current density and on the form of the crossover. For this reason the assignment of beam temperature based on the distributions should not be made.

Massey and coworkers[5] studied the photoemission from a flat surface and in their theoretical discussion distinguished between the average and fluctuating forces acting upon the electrons. The average force arising from the space charge of the ensemble of electrons leads to broadening of the beam radius, but not to energy broadening. The fluctuating component, on the other hand, leads to both energy and radial beam broadening by way of both potential and thermal energy relaxation. In a uniformly accelerating field they calculated ΔE and Δr by considering fluctuations in the beam. The initial potential energy of the electrons is converted to kinetic energy and this effect in their case is large because of the energy provided by the exciting laser. Their analysis, which is comparable to Knauer's[40] leads to the following expressions for the energy and radial broadening:

$$\Delta E = 0.61\ (\pi\epsilon_0)^{-5/6}\ m^{1/4}\ e^{13/12}\ D^{2/3}\ J^{1/2}\ \phi_a^{-1/12}$$

$$\Delta r_f = 0.61\ (\pi\epsilon_0)^{-5/6}\ m^{1/4}\ e^{1/12}\ D^{5/3}\ J^{1/2}\ \phi_a^{-13/12}$$

$$\Delta r_S = (J\ r\ D^2 / \epsilon_0)(m/2e)^{1/2}\ \phi_a^{-3/2}$$

where D is the diode spacing, ϕ_a is the anode potential and r_f is the trajectory aberration arising from the fluctuating forces, and r_S is the trajectory aberration arising from the space charge.

In 1981 Knauer[48] conducted an analysis of the energy spread from point sources using a sphere model for the emitter. He considered both electrons and ions. Because of the radial paths taken by the particles, this model is collision free and the largest contribution to the energy spread occurs in the inital acceleration region. Also in real applications, apertures cut off much of the beam current downstream. He found ΔE proportional to the two thirds power of the current.

CHAPTER THREE

The Pairwise Model

3.1 Introduction

Energy broadening in charged particle beams occurs primarily by means of the relaxation of initial potential energy through energy exchange between pairs of unusually close particles or by means of the relaxation of initial transverse energy through collisional equilibrations. In field electron and ion emission the primary means of energy broadening is via potiential energy relaxation[40]. For low currents, where the average interparticle separation $<\delta_0>$ is greater than the beam radius, the particles lie in what Knauer defines as the single file regime. It is this regime which will be explored by means of a simple two-particle numerical model.

In this model an electric field distribution is selected to represent the field in space between the emitter and collector surfaces of a field electron emitter or a liquid metal ion source. In these studies, analytic expressions describing a spherical field, Figure 1, and the field of a sphere-on-orthogonal-cone (SOC) geometry, Figure 2, were used.

A pair of charged particles representing a fluctuation in the emission process are introduced into the electric field at the emitter

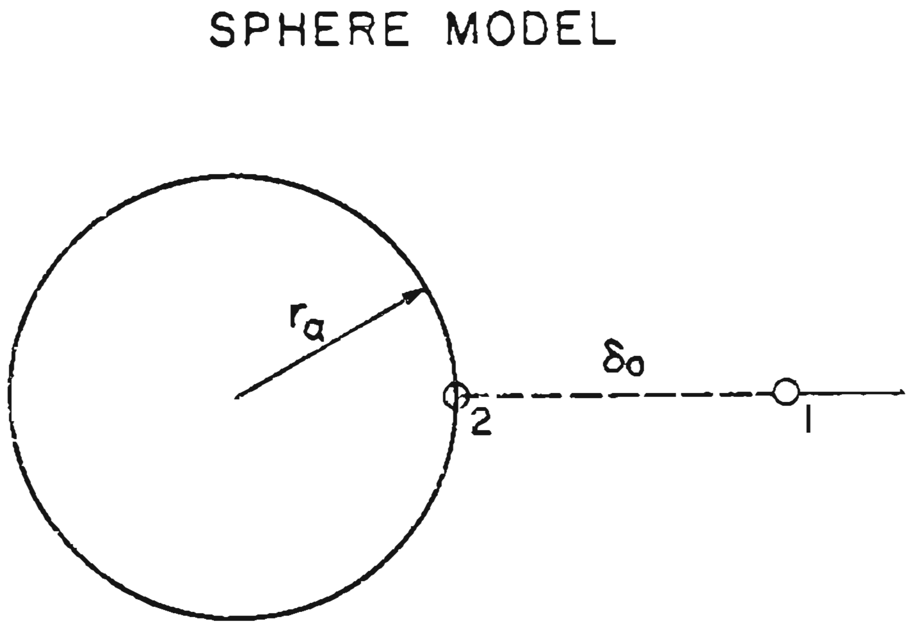
SPHERE MODEL
r_a
δ_0
2
1

Figure 1. Spherical Emitter Model. The radius of the sphere is r_a, particle 1 has traversed a distance of δ_0 in time τ_0 and particle 2 is shown at the moment of emission. The trajectories of the two particles are colinear.

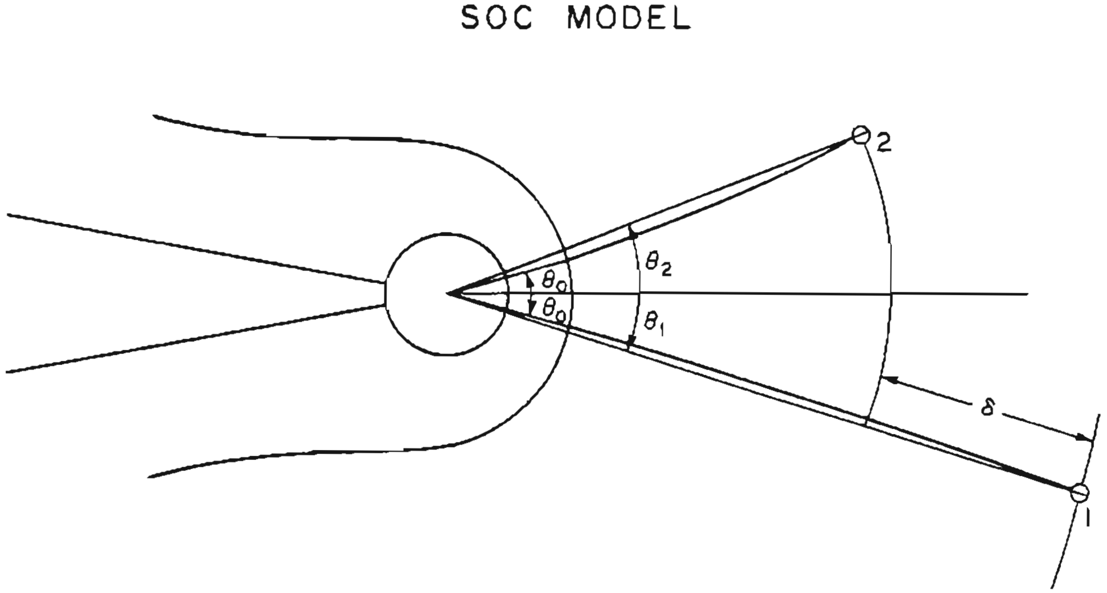

Figure 2. Sphere on Orthogonal Cone (SOC) Model. The radius of the emitter is measured from the center of the core sphere to the apex of the emitter surface. The particles are shown at some time τ having been emitter from points equidistant from the emitter apex lying in the same plane. The half-angle of emission is θ_0, the angular coordinates of the particles are measured with respect to the center of the core sphere, and δ measures the difference in the radial coordinate between the two particles.

surface, generally one at a time. The equations of motion for the particles are then solved numerically, as will be described in Chapter 4.

The overall emission process is assumed to follow a Poisson distribution with the time between successive emission events being exponentially distributed.[49] Accordingly, the probability function for the interevent time τ_0 is given by

$$P(\tau_0) = 1 - \exp(-\lambda\tau_0) \tag{9}$$

with λ, the rate of emission, defined as

$$\lambda = I/ne \tag{10}$$

Also, with this assumption the probability density function, which is the derivative $dP(\tau_0)/d\tau_0$ is given by

$$f(\tau_0) = \lambda\exp(-\lambda\tau_0) \tag{11}$$

Now from the probability density function for some parameter p, the mean value of the parameter is given by

$$\langle p\rangle = \int_{-\infty}^{\infty} pf(p)dp \tag{12}$$

In these studies model calculations will be used to determine the functional relationships of various quantities to the interevent time τ_0. By substitution into Equation (9), the probability density function (PDF) for each quantity will then be determined and the mean value calculated from Equation (12). Since all the quantities are functions of time, the lower limit in Equation (12) becomes zero.

As an illustration of this procedure, the mean initial spacing between particle pairs will be calculated. Each particle has charge ne, mass m and for this example, is being accelerated by the electric field outside a spherical emitter of radius a and electric potential V_0. Within time τ_0 the first particle will traverse distance δ_0. For the cases where $\delta_0 < a$, the field F(r) can be approximated by $F_0 = V_0/a$ so that

$$\delta_0 = neF_0\tau_0^2/2m \tag{13}$$

Substitution of Equation (13) into Equation (9) and differentiating yields the PDF of δ_0:

$$f(\delta_0) = (k/2)\ \delta_0^{-1/2} \exp(-k\ \delta_0^{\ 1/2}) \tag{14}$$

where $k = I(ne)^{-3/2}\ (2m/F_0)^{1/2}$. The expected value of the initial interparticle spacing can be calculated from

$$<\delta_0>= \int_0^\infty \delta_0\ f(\delta_0)d\delta_0$$

$$= \int_0^\infty (k/2)\delta_0^{\ 1/2} \exp(-k\delta_0^{\ -1/2})d\delta_0 \tag{15}$$

Substituting $\delta_0 = x^2 = g(x)$ and $d\delta_0 = 2xdx$ results in

$$<\delta_0>= \int_0^\infty (kx/2)\exp(-kx)(2x)dx$$

$$=k\int_0^\infty x^2 \exp(-kx)dx$$

$$= k(2/k^3)$$

$$= (ne)^3\ F_0/m/I^2 \tag{16}$$

This example furnishes a means of relating the observed current I to the initial particle spacing $<\delta_0>$. The trajectories of pairs of electrons or ions whose initial spacings are significantly less than the mean spacing will be studied by means of the model calculations. However, it will be assumed that the fluctuation in spacing used in the model may be expressed as a percentage of the mean spacing, so that Equation (16) applies with the inclusion of a proportionality factor.

For the remainder of this chapter the focus will be on the two particle model itself, proceeding with a derivation of the equations of motion of the particles traveling in an unspecified electric field, followed by a description of the two fields considered in this present work, and concluding with a discussion of the means of calculating the energy spread in the two particle model.

3.2 Particle Equations of Motion

The expressions for the electric potential of a pair of point charges in the presence of a conducting spherical emitter will now be derived using a spherical emitter model to develop expressions that include image charges. These image terms will also be approximately correct for the SOC model because only emission on or near the axis of symmetry will be considered where, for the distances over which the image terms are non-negligible, the SOC surface is very nearly spherical. Although the image terms were included in this part of the derivation for completeness, they were omitted from the machine calculations because of their very limited contribution. Over the region where they are significant, their influence can be thought of as balanced by an initial radial kinetic energy. The effect of having a net radial or transverse initial kinetic energy is best handled by Monte Carlo techniques and was not studied with this two particle model.

According to the nature of the geometries of the problem, spherical coordinates will be used. However, because of the azimuthal symmetry, only the (r,θ) coordinates need be considered. From Figure 3 the following relationships are obtained:

$$r_{12} = (r_1{}^2 + r_2{}^2 - 2r_1r_2 \cos\theta_{12})^{1/2}$$

$$r_{12}' = (r_1{}^2 + r_2'^2 - 2r_1r_2' \cos\theta_{12})^{1/2}$$

$$r_1'{}_2 = (r_1'^2 + r_2{}^2 - 2r_1'r_2 \cos\theta_{12})^{1/2}$$

Noting that $r_1' = r_0{}^2/r_1$ and $r_2' = r_0{}^2/r_2$ the last two equations may be rewritten as

$$r_{12}' = [r_1{}^2 + r_0{}^4/r_2{}^2 - (2r_1r_0{}^2/r_2) \cos\theta_{12}]^{1/2}$$

$$r_1'{}_2 = [r_0{}^4/r_1{}^2 + r_2{}^2 - (2r_2r_0{}^2/r_1) \cos\theta_{12}\}^{1/2}$$

The electric potential at p_1, the position of particle 1 arising from the other particle and image charges is:

$$\phi_1 = \frac{Q_2}{4\pi\epsilon_0 r_{12}} + \frac{Q_1(-r_0/r_1)}{4\pi\epsilon_0(r_1 - r_1')} + \frac{Q_2 r_0/r_2}{4\pi\epsilon_0 r_{12}'}$$

$$= \frac{Q_2}{4\pi\epsilon_0 r_{12}} - \frac{Q_1 r_0}{4\pi\epsilon_0(r_1 - r_0{}^2/r_1)r_1} - \frac{Q_2 r_0}{4\pi\epsilon_0 r_{12}'}$$

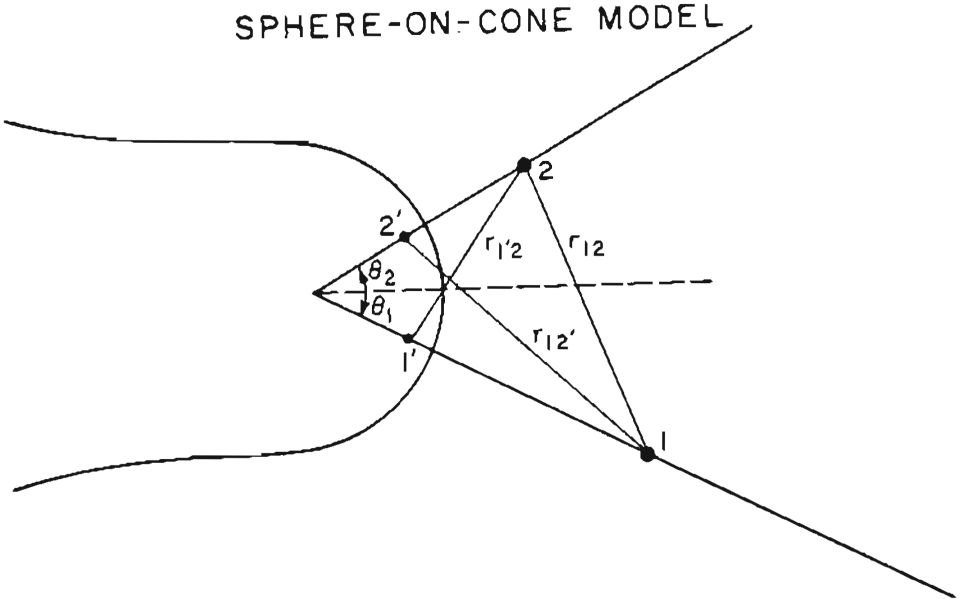
SPHERE-ON-CONE MODEL
2
2'
θ_2
θ_1
1'
$r_{1'2}$
r_{12}
$r_{12'}$
1

Figure 3. Geometry of the SOC Model. Shown are the particles 1 and 2, and their image charges, 1' and 2' along with the vectors joining them.

$$= \frac{1}{4\pi\epsilon_0}\left[\frac{Q_2}{r_{12}} - \frac{Q_1 r_0}{r_1^2 - r_0^2} - \frac{Q_2 r_0}{r_2 r_{12}'}\right] \tag{17a}$$

where Q_1 and Q_2 are the charges on particles 1 and 2. Similarly the electric potential at p_2 is given by

$$\phi_2 = \frac{1}{4\pi\epsilon_0}\left[\frac{Q_1}{r_{12}} - \frac{Q_2 r_0}{r_2^2 - r_0^2} - \frac{Q_1 r_0}{r_1\, r_{12}'}\right] \tag{17b}$$

The equations of motion for the particles in an external electric field can be obtained from the Lagrangian for the system:

$$L = T - V$$

where T, the total kinetic energy is given by

$$T = \{\, m_1[\, \dot{r}_1^2 + (r_1\dot{\theta}_1)^2 \,] + m_2[\, \dot{r}_2^2 + (r_2\dot{\theta}_2)^2 \,] \,\}/2 \tag{18}$$

and where V, the total potential energy is given by

$$V = V_{ext} + V_1 + V_2 \tag{19}$$

where V_{ext} is the potential energy of the external field, and V_1 and V_2 are the potential energies of the two particles. The equations of motion in r and θ for each particle are then as follows:

$$\frac{d}{dt}\left[\frac{\partial L}{\partial \dot{r}_i}\right] = \frac{\partial L}{\partial r_i}, \qquad \frac{d}{dt}\left[\frac{\partial L}{\partial \dot{\theta}_i}\right] = \frac{\partial L}{\partial \theta_i} \tag{20}$$

Substitution from Equations (17)-(19) into (20) for particle 1 results in:

$$\frac{d}{dt}\left[\frac{\partial L}{\partial \dot{r}_1}\right] = \frac{\partial L}{\partial r_1} = m_1\ddot{r}_1$$

$$= m_1\dot{\theta}_1{}^2 r_1 + \frac{\partial V_{ext}}{\partial r_1}$$

$$- \frac{Q_1}{4\pi\epsilon_0}\left[\frac{(r_1 - r_2\cos\theta_{12})Q_2}{r_{12}{}^3} - l_{r1}\right] \qquad (21a)$$

$$\frac{d}{dt}\left[\frac{\partial L}{\partial \dot{\theta}_1}\right] = \frac{\partial L}{\partial \theta_1} = m_1 r_1{}^2\ddot{\theta}_1 + 2m_1 r_1\dot{r}_1\hat{\theta}_1$$

$$= r_1 \frac{\partial V_{ext}}{\partial \theta_1} - \frac{Q_1}{4\pi\epsilon_0}\left[\frac{r_1 r_2 Q_2}{r_{12}{}^3} - l_{\theta 1}\right]\sin\theta_{12} \qquad (21b)$$

and for particle 2:

$$\frac{d}{dt}\left[\frac{\partial L}{\partial \dot{r}_2}\right] = \frac{\partial L}{\partial r_2} = m_2\ddot{r}_2$$

$$= m_2\dot{\theta}_2{}^2 r_2 + \frac{\partial V_{ext}}{\partial r_2}$$

$$- \frac{Q_2}{4\pi\epsilon_0}\left[\frac{(r_2 - r_1\cos\theta_{12})Q_1}{r_{12}{}^3} - l_{r2}\right] \qquad (21c)$$

$$\frac{d}{dt}\left[\frac{\partial L}{\partial \dot{\theta}_2}\right] = \frac{\partial L}{\partial \theta_2} = m_2 r_2^2 \ddot{\theta}_2 + 2 m_2 r_2 \dot{r}_2 \dot{\theta}_2$$

$$= r_2 \frac{\partial V_{ext}}{\partial \theta_2} - \frac{Q_2}{4\pi\epsilon_0}\left[\frac{r_1 r_2 Q_1}{r_{12}^3} - I_{\theta 2}\right]\sin\theta_{12} \tag{21d}$$

where the image terms are

$$I_{r1} = \frac{2 r_0 Q_1}{(r_1^2 - r_0^2)^2} + Q_2\left[\frac{r_0 r_1 - (r_0^3/r_2)\cos\theta_{12}}{r_2\, r_{12'}^3} + \frac{r_0}{r_1^2\, r_{1'2}} + \frac{r_0}{r_1\, r_{1'2}^3}\left[\frac{r_0^2\, r_2 \cos\theta_{12}}{r_1^2} - \frac{r_0^4}{r_1^3}\right]\right] \tag{22a}$$

$$I_{\theta 1} = Q_2\left[\frac{r_0^3 r_1}{r_2^2\, r_{12'}^3} + \frac{r_0^3 r_2}{r_1^2\, r_{1'2}^3}\right] \tag{22b}$$

and where I_{r2} and $I_{\theta 2}$ are analogous to I_{r1} and $I_{\theta 1}$ (the subscripts on the charges and radial variables being interchanged).

3.3 Electric Field Models

In the present studies two types of electric field models were used: the spherical charged conductor, and the sphere-on-orthogonal-cone

(SOC) model. For the sphere model the particles were also confined to single-file trajectories ($\theta_1 = \theta_2 = 0$). The SOC model was selected in order to more accurately represent the emitter surface of both electron emitters and LMIS. For the SOC model, both single-file and off-axis trajectories were produced.

The sphere model equations are presented first, and then the SOC model equations are derived. From this point on the image terms of Equation (22) will be omitted as discussed in Section 3.1.

For single-file emission, with a concentric spherical emitter/ collector field, Equations (21) become

$$m_1 r_1 = \frac{\partial V_{sphere}}{\partial r_1} + \frac{Q_1 Q_2}{4\pi\epsilon_0}\left[\frac{1}{(r_1 - r_2)^2}\right]$$

$$= \frac{Q_1 E r_0^2}{m r_1^2} + \frac{Q_1 Q_2}{4\pi\epsilon_0 \delta_0} \qquad (23a)$$

$$m_2 r_2 = \frac{Q_2 E r_0^2}{m r_2^2} - \frac{Q_1 Q_2}{4\pi\epsilon_0 \delta_0} \qquad (23b)$$

where $\delta_0 = r_2 - r_1$. In these equations the zero potential is at infinity.

The SOC electric field model is a solution to a problem posed by Smythe[50]. The problem statement and solution are as follows.

A conducting sphere of radius r_a is supported by an orthogonal cone (also conducting) whose exterior half-angle is α. This system is charged, with the zero potential surface on the conductors. The problem is to find the potential V at an exterior point p.

In spherical coordinates V = 0 for $r = r_a$ and also for $\theta = \alpha$. Laplace's equation in spherical coordinates is

$$\frac{\partial}{\partial r}\left[r^2 \frac{\partial V}{\partial r}\right] + \frac{1}{\sin\theta}\left[\sin\theta \frac{\partial V}{\partial r}\right] + \frac{1}{\sin^2\theta} \frac{\partial^2 V}{\partial \phi^2} = 0 \tag{24}$$

This equation can be solved by the separation of variables technique, and by applying power series solutions to the separated expressions.

Setting $V = R(r)\Theta(\theta)\Phi(\phi) = R(r)S(\theta,\phi)$, substituting V = RS and dividing by RS yields

$$\frac{1}{R}\frac{d}{dr}\left[r^2 \frac{dR}{dr}\right] + \frac{1}{S\sin\theta}\frac{\partial}{\partial\theta}\left[\sin\theta \frac{\partial S}{\partial\theta}\right] + \frac{1}{S\sin^2\theta} \frac{\partial^2 S}{\partial \phi^2} = 0 \tag{25}$$

Set the first term in r equal to K, and the last two terms in S equal to -K.

If a power series solution in r:

$R = \sum a_n r^n$

is assumed, then

$$\begin{aligned} RK &= \sum n(n+1)a_n r^n \\ &= \sum K a_n r^n \end{aligned} \tag{26}$$

Thus if $K = n(n + 1)$, then $R = a_n r^n$ and any sum $\sum a_n r^n$ or integral $\int a_v r^v dv$ is also a solution.

To find the second independent solution let

$R^* = \sum b_m r^{-m}$

Then

$$\frac{d}{dr}\left[r^2 \frac{dR^*}{dr} \right] = \sum (-m(1 - m))b_m r^{-m}$$

$$= \sum K b_m r^{-m}$$

$$= \sum n(n + 1)b_m r^{-m} \qquad (27)$$

Thus $m(m - 1) = n(n + 1)$. Solving for m by means of the quadratic formula gives the two roots $m_1 = -n$, $m_2 = n + 1$. The case m_1 is identical to the previous solution, while the case m_2 can be written as

$$R = \sum b_n r^{-n-1}$$

The general solution is then

$$R = \sum (a_n r^n + b_n r^{-n-1}) \qquad (28)$$

and any linear combination involving non-integral n is also a solution. If the value $K = n(n+1)$ is substituted into the equation involving θ and ϕ, and then multiplied by S the result is

$$n(n + 1)S + \frac{1}{S\sin\theta}\frac{\partial}{\partial\theta}\left[\sin\theta \frac{\partial S}{\partial\theta} \right] + \frac{1}{S\sin^2\theta}\frac{\partial^2 S}{\partial\phi^2} = 0 \qquad (29)$$

For the next step Equation (29) is divided by $\Theta\Phi/\sin^2\theta$:

$$n(n+1)\sin^2\theta + \frac{\sin\theta}{\Theta}\frac{d}{d\theta}\sin\theta\frac{d\Theta}{d\theta} + \frac{1}{\phi}\frac{\partial^2\Phi}{\partial\phi^2} = 0 \qquad (30)$$

Set the terms in ϕ equal to $-K_1$, and the terms in θ equal to $+K_1$. Then

$$\frac{\partial^2\Phi}{\partial\phi^2} = -K_1\Phi$$

If $K_1 = m$ then

$$\begin{aligned}\Phi &= \sum [c_m\cos(m\phi) + d_m\sin(m\phi), && m \neq 0\\ &= C\phi + D \quad , && m = 0\end{aligned} \qquad (31)$$

In this problem V is independent of Φ since there is azimuthal symmetry. Therefore $\Phi = D$ and $m = 0$. Inserting this result into Equation (30) results in:

$$n(n+1)\sin^2\theta + \frac{\sin\theta}{\Theta}\frac{d}{d\theta}\sin\theta\frac{d\Theta}{d\theta} - m^2 = 0 \qquad (32)$$

Multiplying by $\Theta/\sin^2\theta$ and making the substitution $\mu = \cos\theta$, $d\mu = \sin\theta d\theta$ yields

$$n(n+1)\Theta + \frac{d}{d\mu}\left[(1-\mu^2)\frac{d\Theta_n}{d\mu}\right] = 0 \qquad (33)$$

which is Legendre's equation and which can be solved by series solution to obtain $\Theta_n = P_n(\mu)$. Thus the electric potential

$$V = R\Theta\Phi$$
$$= D \sum [a_n r^n + b_n r^{-n-1}]\, P(\mu)$$

Next the boundary conditions are to be applied. When $\theta = \alpha$ then $V = 0$, since the conducting surfaces are at ground potential. Thus

$$D \sum [a_n r^n + b_n r^{-n-1}]\, P(\cos \alpha) = 0$$

which implies that $P_n(\cos \alpha) = 0$. But for $\alpha \neq \theta$ and for arbitrary r the potential $V \neq 0$. Examination of the Legendre functions shows that for a given $\alpha > \pi/2$ only one value of n will satisfy these boundary conditions and that $0 > n > 1$. Therefore the summation can be dropped to obtain

$$V = D \sum [a_n r^n + b_n r^{-n-1}]\, P_n(\cos\theta) \qquad (34)$$

At $r = r_a$ the potential also equals zero which leads to the condition

$$a_n r_a{}^n = -b_n r_a{}^{-n-1} \qquad (35)$$

and therefore

$$b_n = -a_n r_a{}^{2n+1} \qquad (36)$$

Setting $A = Da_n$ gives

$$V = A[r^n - r_a{}^{2n+1}\, r^{-n-1}]P_n(\cos\theta) \qquad (37)$$

Suppose that an equipotential surface is fixed at some voltage V_R and passes through the point $(r,\theta) = (R,0)$. $P_n(\cos(0)) = 1$ and

$$V_R = A[R^n - r_a{}^{2n+1}\, r^{-n-1}]$$

This then determines the value of A to be

$$A = V_R/[R^n - r_a{}^{2n+1}\, r^{-n-1}] \qquad (38)$$

For $R >> r_a$ then $R^n >> - r_a^{2n+1} r^{-n-1}$ and thus $A = V_R/R^n$.

In justification of this approximation, observe the following typical examples. For $n = 0.5$, $r_a = 10^{-7}$m and $R = 10^{-2}$m, $r_a^{2n+1} r^{-n-1} = 10^{-11}$ while $R^n = 10^{-1}$. For $n = 0.15$, $r_a = 10^{-7}$m and $R = 10^{-2}$m, $r_a^{2n+1} r^{-n-1} = 1.6 \times 10^{-7}$ while $R^n = 0.5$.

Substituting V_R/R^n for A gives

$$V = V_R \left[\frac{r_a}{R}\right]^n \left[\left[\frac{r}{r_a}\right]^n - \left[\frac{r_a}{r}\right]^{n+1} \right] P_n(\cos\theta) \tag{39}$$

Again at $r = r_0$ the parameter $\gamma = r_0 / r_a$ is defined and when $\theta = 0$

$$V_0 = V_R \left[\frac{r_a}{R}\right]^n \left[\gamma^n - \left[\frac{1}{\gamma}\right]^{n+1} \right] \tag{40}$$

Using this potential as the reference voltage results in

$$V = V_R \left[\frac{r_a}{R}\right]^n \left[\left[\frac{r}{r_a}\right]^n - \left[\frac{r_a}{r}\right]^{n+1} \right] P_n(\cos\theta) - V_0 \tag{41}$$

The electric field components for this potential in the radial (r) and tangential (θ) directions may be found from the relations

$$E_r(r,\theta) = \frac{-\partial V}{\partial r} \tag{42a}$$

$$E_\theta(r,\theta) = -\frac{1}{r}\frac{\partial V}{\partial \theta} \tag{42b}$$

The radial component is

$$E_r = -V_R \left[\frac{r_a}{R}\right]^n \left[\frac{n}{r_a}\left[\frac{r}{r_a}\right]^{n-1} - \frac{n+1}{r_a}\left[\frac{r_a}{r}\right]^{n+2} \right] P_n(\cos\theta) \qquad (43)$$

For the tangential component the Legendre function may be expressed in terms of the hypergeometric series:

$P_n(\cos\theta) = F\{-n,1+n,1;(1-\cos\theta)/2\}$

where

$$F\{a,b,c;z\} = 1 + \sum_{k=1}^{\infty} \frac{a(a+1)\cdots(a+k-1)\ b(b+1)\cdots(b+k-1)\ z^k}{c(c+1)\cdots(c+k-1)\ k!}$$

Now the derivative of F with respect to z, $dF(a,b,c;z)/dz$ equals $(ab/c)F(a+1,b+1,c+1;z)$. With $z(\theta) = (1-\cos\theta)/2$ the result is

$$\frac{dF(z(\theta))}{dz} = \frac{dz}{d\theta}\frac{dF}{dz} = \frac{\sin\theta}{2}\ \frac{ab}{c} F(a+1,b+1,c+1;z)$$

Therefore the tangential component of the electric field is given by

$$E_\theta(r,\theta) = -\frac{V_R}{r}\left[\frac{r_a}{R}\right]^n \left[\left[\frac{r}{r_a}\right]^n - \left[\frac{r_a}{r}\right]^{n+1} \right]$$

$$\times \frac{\sin\theta}{2}\ \frac{d}{d\theta} F\left[-n,n+1,1; \frac{1-\cos\theta}{2} \right]$$

$$= -\frac{V_R}{r_a}\left[\frac{r_a}{R}\right]^n \left[\left[\frac{r}{r_a}\right]^{n-1} - \left[\frac{r_a}{r}\right]^{n+2} \right]$$

$$\times \frac{(-n)(n+1)\sin\theta}{2}\ F\left[1-n,n+2,2; \frac{1-\cos\theta}{2} \right]$$

$$= \frac{V_R}{r_a}\left[\frac{r_a}{R}\right]^n \frac{n^2+n}{2}\left[\left[\frac{r}{r_a}\right]^{n-1} - \left[\frac{r_a}{r}\right]^{n+2}\right]$$

$$\times \sin\theta\ F\left[1\text{-}n,n+2,2;\frac{1-\cos\theta}{2}\right] \tag{44}$$

Substitution of Equations (43) and (44) into Equation (21) yields the equations of motion for the SOC model

$$\ddot{r}_1 = r_1\dot{\theta}_1^{\,2} - \frac{Q_1Q_2}{4\pi m_1\epsilon_0}\ \frac{r_1 - r_2\cos\theta_{12}}{r_{12}^{\,3}} -$$

$$\frac{Q_1V_R}{m_1r_a}\left[\frac{r_a}{R}\right]^n\left[n\left[\frac{r_1}{r_a}\right]^{n-1} + (n+1)\left[\frac{r_a}{r_1}\right]^{n+2}\right]P_n(\cos\theta_1) \tag{45a}$$

$$\ddot{r}_2 = r_2\dot{\theta}_2^{\,2} - \frac{Q_1Q_2}{4\pi m_2\epsilon_0}\ \frac{r_2 - r_1\cos\theta_{12}}{r_{12}^{\,3}} -$$

$$\frac{Q_2V_R}{m_2r_a}\left[\frac{r_a}{R}\right]^n\left[n\left[\frac{r_2}{r_a}\right]^{n-1} + (n+1)\left[\frac{r_a}{r_2}\right]^{n+2}\right]P_n(\cos\theta_2) \tag{45b}$$

$$\ddot{\theta}_1 = \frac{\dot{r}_1\dot{\theta}_1}{r_1} - \left[\frac{Q_1Q_2\sin\theta_{12}}{4\pi m_1\epsilon_0}\ \frac{r_1r_2}{r_{12}^{\,3}} + \right.$$

$$\frac{Q_1V_R}{m_1r_1r_a}\left[\frac{r_a}{R}\right]^n\frac{(n+n^2)}{2}\left[\left[\frac{r_1}{r_a}\right]^{n-1} - \left[\frac{r_a}{r_1}\right]^{n+2}\right]\times$$

$$F[\,1\text{-}n,\ 2+n,\ 2;\ (1-\cos\theta_1)/2\,]\ \sin\theta_1 \tag{45c}$$

$$\ddot{\theta}_2 = \frac{\dot{r}_2\dot{\theta}_2}{r_2} - \left[\frac{Q_1Q_2\sin\theta_{12}}{4\pi m_2\epsilon_0}\ \frac{r_1r_2}{r_{12}^{\,3}} + \right.$$

$$\frac{Q_2 V_R}{m_2 r_2 r_a} \left[\frac{r_a}{R}\right]^n \frac{(n + n^2)}{2} \left[\left[\frac{r_2}{r_a}\right]^{n-1} - \left[\frac{r_a}{r_2}\right]^{n+2} \right] \times$$

$$F[\,1-n,\ 2+n,\ 2;\ (1 - \cos\theta_2)/2\,]\ \sin\theta_2 \tag{45d}$$

This system of second order differential equations, as well as Equations (23) for the sphere model can be solved numerically by the Runge-Kutta method if they are first transformed into an equivalent system of first order differential equations. The following simple transformation yields such a system with time as the independent variable:

$$\begin{aligned}
&d\tau/d\tau = 1 && d\theta_1/d\tau = v_{\theta_1}\\
&dr_1/d\tau = v_{r_1} && d\theta_2/d\tau = v_{\theta 2}\\
&dr_2/d\tau = v_{r2} && dv_{\theta_1}/d\tau = d^2\theta_1/d\tau^2\\
&dv_{r_1}/d\tau = d^2r_1/d\tau^2 && dv_{\theta_2}/d\tau = d^2\theta_2/d\tau^2\\
&dv_{r_2}/d\tau = d^2r_2/d\tau^2 &&
\end{aligned} \tag{46}$$

3.4 Energy Integrals

This chapter will now be closed with a discussion of the calculation of the energy broadening for the two particle case.

The calculation of the energy spread ΔE entails the calculation of the change in the kinetic energy experienced by each particle as it moves under the influence of the forces generated by the emitter-collector electric field, and by the Coulomb field of the other particle. The change in the kinetic energy of a particle moving from point A to point B under the influence of external forces is given by the path integral:

$$\Delta E = E_B - E_A = \int_{A_{\text{path}}}^{B} \mathbf{F} \cdot d\mathbf{l}$$

which in spherical coordinates may be expressed as

$$\Delta E = \int_{A_{\text{path}}}^{B} F_r dr + \int_{A_{\text{path}}}^{B} r F_\theta d\theta \qquad (47)$$

The energy change caused directly by the change in potential energy between the emitter surface and the collector surface, which acts equally on both particles is not of concern in this study. The imparted energy is $Q(V_B - V_A)$ where Q is the particles' charge and V_A and V_B are the potentials at points A and B. It is rather the effect of the Coulomb force acting between the unusually proximate pair that is being computed. For the SOC model, the forces acting on each particle are given by:

$$\mathbf{F}_1 = m_1 \mathbf{a}_1 = m[(r_1 - r_1 \theta_1^2)\underline{r} + (r_1 \theta_1 + 2 r_1 \theta_1)\underline{\theta}]$$

$$= \frac{Q_1 Q_2}{r_{12}^3 4 \pi \epsilon_0} [(r_2 \cos\theta_{12} - r_1)\underline{r} - (r_2 \sin\theta_{12})\underline{\theta}] \qquad (48)$$

$$\mathbf{F}_2 = \frac{Q_1 Q_2}{r_{12}^3 4 \pi \epsilon_0} [(r_1 \cos\theta_{12} - r_2)\underline{r} - (r_1 \sin\theta_{12})\underline{\theta}] \qquad (49)$$

The change in kinetic energy due to the Coulomb interaction for particle 1 and 2 is given by:

$$\Delta E_1 = C\left[\int_{r_0+\delta_0}^{r_f} \frac{r_2\cos\theta_{12} - r_1}{r_{12}^3}\,dr_1 + \int_{\theta_{\delta 0}}^{\theta_f} \frac{r_1 r_2 \sin\theta_{12}}{r_{12}^3}\,d\theta_1\right] \tag{50a}$$

$$\Delta E_2 = C\left[\int_{r_0}^{r_f} \frac{r_1\cos\theta_{12} - r_2}{r_{12}^3}\,dr_2 + \int_{\theta_0}^{\theta_f} \frac{r_1 r_2 \sin\theta_{12}}{r_{12}^3}\,d\theta_2\right] \tag{50b}$$

where $C = Q_1Q_2/4\pi\epsilon_0$, r_0 = emitter radius, r_f = collector radius, δ_0 = radial separation $(r_1 - r_2)$ when $r_2 = r_0$, $\theta_{\delta 0} = \theta_1$ when $r_1 = r_0 + \delta_0$, θ_0 = emission angle, θ_f = final angle, $\theta_{12} = (\theta_1 - \theta_2)$ and $r_{12} = (r_1^2 + r_2^2 - 2r_1r_2 \cos\theta_{12})^{1/2}$.

For the sphere model with the restrictions of colinear emission ($\theta_1 = \theta_2 = 0$), Equations (50) simplify to

$$\Delta E_1 = C\int_{r_0+\delta_0}^{r_f} \frac{dr_1}{(r_1 - r_2^2)} \tag{51a}$$

$$\Delta E_2 = C\int_{r_0}^{r_f} \frac{dr_2}{(r_1 - r_2^2)} \tag{51b}$$

The limits on the integrals reflect the fact that the Coulomb force acts only when both particles are present.

The total energy spread ΔE of the two particles is

$$\Delta E = \Delta E_1 - \Delta E_2 \tag{52}$$

At each point along the trajectories, values for the integrands appearing in the energy spread Equations (50) or (51) were computed and stored on disk along with the spatial and time coordinates of each particle. Figure 4 shows the components ΔE_1 and ΔE_2 as a function of distance for a typical set of gallium ion trajectories from an SOC model emitter.

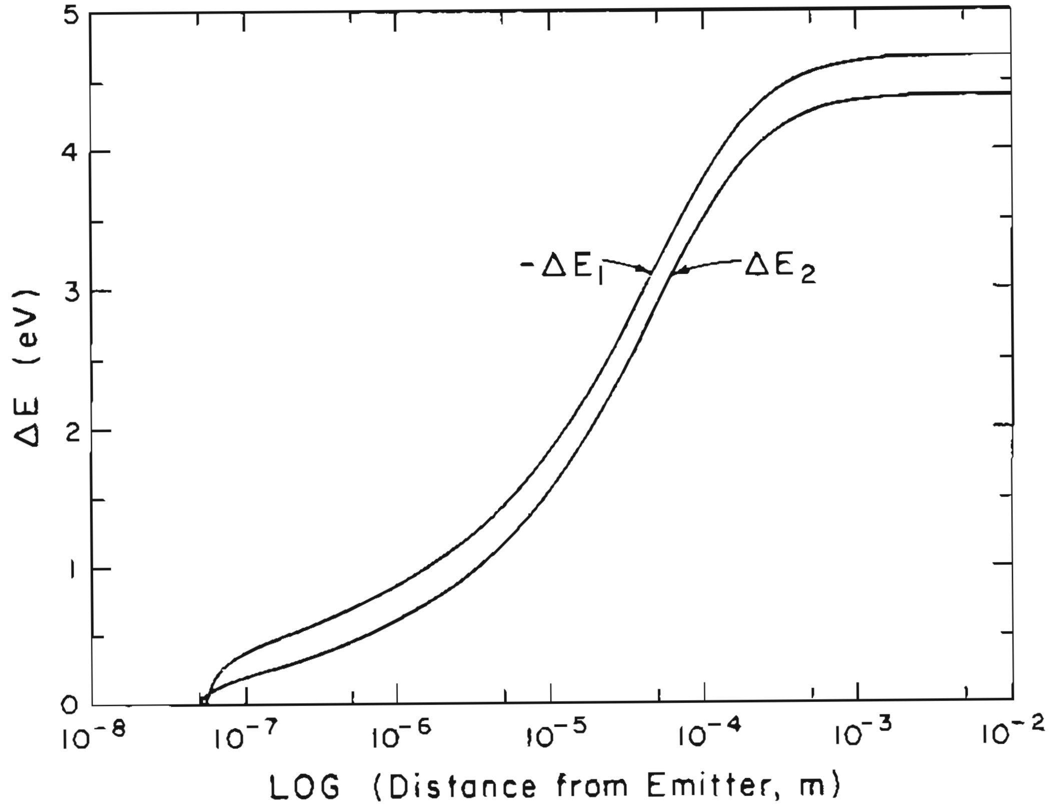

Figure 4. Components of Energy Spread. An Example of the contributions ΔE_1 and ΔE_2 to the total energy spread, ΔE_{Tot} is shown as a function of radial distance from the emitter core sphere. These data are from Ga^+ ions emitted colinearly from an emitter of radius $r_a = 5\times10^{-2}\mu m$, $\gamma=3.0$, $n=0.5$ and $\delta_0 = 5\times10^{-3}\mu m$.

CHAPTER FOUR

Numerical Methods

4.1 Introduction

The major numerical techniques used in the solution of the equations of motion (23) and (45), and the techniques used in the integration of Equations (50) and (51) are discussed in this chapter.

4.2 The Runge-Kutta Algorithm

A fourth-order Runge-Kutta method[51] was used to solve the system of equations (23) and also (45). A Runge-Kutta method is designed to approximate the Taylor series solutions of the system without explicit definitions of, nor evaluations of derivatives other than the first. A fourth-order method agrees with the Taylor series solution through terms of order h^4 where h is the increment in the independent variable in the series expansion.

Symbolically then, given the system of first order ordinary differential equations:

$$\begin{aligned} x_1(t) &= f_1(t, x_1(t), x_2(t), \ldots, x_n(t)) \\ x_2(t) &= f_2(t, x_1(t), x_2(t), \ldots, x_n(t)) \\ x_n(t) &= f_n(t, x_1(t), x_2(t), \ldots, x_n(t)) \end{aligned} \tag{53}$$

with the initial conditions $x_i(t_0) = x_{i0}$; for $i = 1, \ldots, n$, a Runge-Kutta algorithm provides estimates $x_i^e(t_0+h)$ to the exact values $x_i(t_0+h)$, where h is an arbitrary increment in t. These estimates are equal to the Taylor series expansion:

$$x_i^e(t_0+h) = \sum_{k=0}^{4} \frac{h^k}{k!} \frac{dx_i(t_0)}{d^k t}$$

There are two disadvantages associated with Runge-Kutta methods. A fourth-order method requires four evaluations of the expressions (53) in order to advance the solution one incremental step in the independent variable. Since the sphere model and the SOC model involve complicated expressions for the derivatives, the Runge-Kutta method is relatively time consuming in comparison to other methods such as predictor-corrector methods. A second disadvantage is that estimation of truncation errors arising from the limited number of terms computed in the Taylor series is not obtained in the calculation procedure, and errors are therefore difficult to estimate.

The first disadvantage is offset by the following considerations. In both the sphere and SOC models, the functions representing the derivatives change very rapidly, and are functions of a variable whose domain must therefore span as many as ten orders of magnitude. Since the ultimate goal is not to produce particle trajectories as functions of time, but rather to produce data from which other quantities of interest are to be derived by integration, a major concern is the ability to easily change step size whenever necessary for providing accurate data to the integration algorithm. The Runge-Kutta method does allow changes in the step size at any time, with basically no overhead. Furthermore it is easy to set up meaningful criteria within the procedure for determining when to make such changes dynamically while the solution advances.

Runge-Kutta methods are also self-starting, that is, the values for the vector **x** need only be specified at one point in time. Other methods of comparable accuracy require knowledge of the solution at four equally spaced points in t. A Runge-Kutta method is often used to provide these four sets of starting values and the second method used to continue the solution. If the step size changes, four new sets of starting values are required. Because the step size in this problem changes so often during the solution, it is more convenient to use the Runge-Kutta method throughout.

Furthermore, Runge-Kutta methods are stable: a small error at one point in the calculations, such as a roundoff truncation error, will tend to decay through successive iterations, rather than propagate.

The system of equations from which Runge-Kutta methods are derived contain eight equations in ten unknown parameters. There are therefore two degrees of freedom in specifying the solution of these equations. By imposing one arbitrary condition, and expressing the solution in terms of one of the unknowns, a particular Runge-Kutta method is obtained. It is possible to select a condition which minimizes the amount of computer memory required for execution of the algorithm, and then select a value for the free parameter which reduces the truncation error. It is also possible to incorporate a "feed-back" technique which compensates for roundoff errors.[51] These features were incorporated in the algorithm used in this study.

One procedure for estimating truncation errors is to perform the calculations using two different step sizes over the same interval. The truncation errors are then approximately $[x_i(h_1) - x_i(h_2)]/15$. It was determined that the truncation errors were negligible during the computations for both the sphere and SOC models.

There are two requirements pertaining to step size selection. The step size must be small enough to allow the Runge-Kutta solution to accurately reproduce the particle trajectories in regions where they are rapidly changing, and also to allow the energy integrations to be accurately performed. In order to meet these requirements, the step size was adjusted logarithmically according to the following scheme. Within a preselected distance r_S from the emitter surface, usually within one emitter radius, the time increment was selected such that for each decade of distance 300 samples of the trajectory were computed. The first 100 were equally spaced out to 20% of the distance. The second were equally spaced between 20% and 50% of the distance, and the last 100 samples spanned the last half of the distance. Beyond r_S 100 samples per decade of distance out to the collector surface were taken, except that 100 closely spaced samples were taken in the neighborhood of the collector surface.

In order to determine the amount of time required to traverse each distance, an estimate, based on the velocity of particle 1, was made for the time to traverse the distance in twenty steps. The estimate was iteratively refined until it was within 1% accuracy and then the solution was recomputed with one fifth of the step size. For the special case of attaining δ_0, the accuracy of the step size was set to 10 ppb.

4.3 Integration Using a Cubic Spline Algorithm

The integrations of the output data of the Runge-Kutta program were performed by a second, independent program also developed by the author. This program provides general purpose interactive graphical and numerical data processing capabilities. Integrations available with this program are performed by means of the integral formulas for a cubic spline approximation to given data sets. The cubic spline algorithm used in this program was adapted from a subroutine used by Hesse and coworkers[52] for background subtraction and area determinations in quantitative Auger electron spectroscopy. A spline function is a composite formula consisting of a sequence of low-order polynomials interpolating on a given set of ordered pairs[53]. This is as opposed to a single high order polynomial fit over the entire domain of the data. In the case of a cubic spline, each element of the sequence is a cubic equation covering a four-point subinterval of the data set:

$$f_k(x) = a_k(x - x_k)^3 + b_k(x - x_k)^2 + c_k(x - x_k) + d_k; \quad k = 1, 2, \ldots, n - 1 \tag{54}$$

where n is the number of data pairs (x_k, y_k) in the given set. The cubic spline interpolating function is then:

$$f(x) = \begin{cases} f_1(x) & x < x_1 \\ f_k(x) & x_k < x < x_{k+1} \\ f_{n-1}(x) & x_{n-1} < x \end{cases}$$

In order to determine the coefficients a_k, b_k, c_k and d_k several conditions must be applied. Different types of conditions are possible and lead to differences in the behavior of the spline function at the ends of the data interval and near discontinuities within the data. Among the conditions applied in this study, the following are of importance.

Three levels of continuity are required from one subinterval to the next, namely continuity in the function, and in its first and second derivatives:

$$y_k = f_k(x_k) \qquad k = 1, \ldots, n-1$$

$$= f_{k-1}(x_k) \qquad k = 2, \ldots, n \tag{55a}$$

$$f'_{k-1}(x_k) = f'_k(x_k) \qquad k = 2, \ldots, n-1 \tag{55b}$$

$$f''_{k-1}(x_k) = f''_k(x_k) \qquad k = 2, \ldots, n-1 \tag{55c}$$

A fourth condition incorporates a set of smoothing factors, p_k, into the algorithm for determining F(x). This allows for some control over the accuracy with which the spline function approaches the given data base. This condition is expressed as follows:

$$f_k(x_k) - y_k\, p_k = \begin{cases} \dfrac{d^3 f_k(x_k)}{dx^3} & k = 1 \\ \dfrac{d^3 f_k(x_k)}{dx^3} - \dfrac{d^3 f_{k-1}(x_k)}{dx^3} & k = 2, \ldots, n-1 \\ \dfrac{d^3 f_{k-1}(x_k)}{dx^3} & k = n \end{cases} \tag{56}$$

This condition maximizes the integral

$$\int_{x_1}^{x_n} \left[\frac{d^2F(x)}{dx^2} \right]^2 dx$$

subject to the condition that

$$\sum_{k=1}^{n} [f_k(x_k) - y_k] p_k < \epsilon$$

where ϵ is some given optional amount. In Hesse's application to Auger spectra, random noise in the measurement could be smoothed out while retaining the peak structure by careful selection of the p_k. In the present study, the p_k were always chosen so as to reproduce the Runge-Kutta program output as accurately as possible.

The representation of a set of data in terms of the cubic spline function renders the numerical evaluation of the integrals and derivatives particularly easy. Writing $h_j = x_{j+1} - x_j$, $h_{k+1} = x - x_{k+1}$ and referring to Equations (54) and (55), the integral formula is:

$$\int_{x_1}^{x} f(x)dx = \sum_{j=1}^{k-1} (a_j h_j^4/4 + b_j h_j^3/3 + c_j h_j^2/2 + d_j h_j) + a_{k+1} h_{k+1}^4/4 + b_{k+1} h_{k+1}^3/3 + c_{k+1} h_{k+1}^2/2 + d_{k+1} h_{k+1} \qquad (57)$$

for k such that $x_{k+1} < x < x_{k+2}$ and for $x < x_n$.

The derivative formula is given by:

$$f'(x) = 3a_k(x - x_k)^2 + 2b_k(x - x_k) + c_k; \;\; x_k < x < x_{k+1} \qquad (58)$$

for the range $x_1 < x < x_n$. The program developed by the author provides interactive access to any of the operations of interpolation, integration and differentiation, each with controllable smoothing, and each capable of handling any data set from four data points to five thousand or more data points.

The program provides the standard error of the estimate as a measure of the accuracy of the spline fit. The standard error of the estimate is defined as:

$$\epsilon_s = \frac{1}{n}\left[\sum_{k=1}^{n} [y_k - f(x_k)]^2 \right]^{1/2} \qquad (59)$$

During the investigation of the sphere model program it was found that, because of the extreme variations in magnitude displayed by the model output over very short intervals, the model data resembles a discontinuous function in some regions of interest. A single cubic spline function covering the whole domain was not capable of adequately representing the model output. In view of this fact, provision was made to partition a given data set into as many as thirty-two subsets, and the integration was performed in piecewise fashion using a separate spline fit for each subset. The value of the integral and error ϵ_S are displayed for each subinterval and the integral values are accumulated towards a total value for the entire set by the program. In this way ϵ_S could be reduced to less than 0.1 ppm.

A demonstration of the accuracy of the entire method of solution to the energy integral evaluation was provided by a comparison of the potential energy between the particles at the moment particle 2 is emitted, and the net kinetic energy of the particles at the collector surface. From the shape of the integral curve, Equations (50) or (51), those cases where essentially all of the potential energy had been converted to kinetic energy could be distinguished by their constant amplitude near the extractor electrode surface, which is evidenced by the insignificance of the contributions of the areas of the last few subintervals in time to the value of the total integral. In these cases, the net final kinetic energy, to at least four digits of accuracy, was equal to the initial potential energy arising from the Coulomb force at the moment of emission of the second particle. This observation will be discussed in more detail in Section 5.2.

4.4 Difficulties in Using the Numerical Methods

Most of the features of the numerical methods employed have been explained in detail in the preceding section. Noted here are some of the difficulties which were encountered, first during the development of the Runge-Kutta algorithm, and then during the integration procedure. The extreme differences in scale presented by both the electric field model geometries create the need for frequent changes in the step size of the advancing solution. The Runge-Kutta technique handles varying step sizes easily, but does not, of course, suggest appropriate step size values. Furthermore, the rapidly changing acceleration caused by the spherical field coupled with Coulomb interaction severely limited the predicting capabilities of known quantities to a very local neighborhood.

The following scheme was devised to overcome these difficulties. An attempt was made to advance the solution to a given distance, usually to a point lying an order of magnitude (less in the tip region) away from the present position. An estimate was made of the step size required for a total of twenty steps to cover the distance. This estimate was based on present acceleration and velocity. The Runge-Kutta algorithm was written as a subroutine whose calling sequence contains several control parameters. The step size and number of steps to advance the solution are supplemented by a key identifying one of the dependent variables in the system of equations, and by a constant. The subroutine was designed so that at every step of the solution, the key variable was compared to the constant. If the key variable was found to be greater than or equal to the constant, the Runge-Kutta subroutine immediately returned to the calling procedure; otherwise it continued to advance the solution until the requested number of steps had been computed.

By means of these control variables, the main program could search for the step size required to advance the solution a specified distance in a given number of steps automatically.

Another problem occurred with small values of δ_0. A limit is reached when the Coulomb force overcomes the force exerted by the cathode thereby driving the second particle back into the emitter. This effect places an upper limit on the total current able to be modelled by single-file emission. When angular separations are permitted, this limit varies depending on the emitter radius.

A third problem with early versions of the Runge-Kutta program occurred at large values of δ_0 and small radius emitters. Subdivisions of the trajectory had been based on the position of particle 1. For large values of δ_0 the force exerted by the emitter on particle 2 greatly exceeded the force on particle 1, and during the iteration process particle 2 would unexpectedly have overtaken particle 1. In single-file emission, this is clearly not possible. It was this problem that led to the finer resolution based on the position of particle 2 within the region between the emitter and δ_0. This and other refinements in the interpolation techniques eliminated this problem.

With respect to the cubic spline integration procedure, the major problems centered around obtaining a highly accurate fit to the Runge-Kutta data. The effect of the smoothing factors p_K depends on the magnitude of the domain and range of the input data and on the spacing between consecutive data points.

Preprocessing of input data was incorporated into the spline algorithm which rescales the data into a neighborhood around 1 in order to standardize the effect of p_k as much as possible. The scaling factors used were always powers of ten. Negative powers of ten are irrational numbers when expressed in the binary system of the computer, but positive powers are not. Therefore, division by the reciprocal of the factor was used if the factor was less than 1, otherwise multiplication by the factor was used in order to retain the maximum accuracy of representation of the source data.

The smoothing factors behave acceptably for data sets which span less than about three orders of magnitude. The Runge-Kutta data typically span sixteen to twenty orders of magnitude. The host program in which the spline algorithm is implemented is able to split its data storage into independent sets. Therefore, consideration was given to dividing the Runge-Kutta data into sections, integrating each section and then summing the result. In so doing each section was able to be accurately fitted and an integral obtained. However, the sum of the integrals of each set does not give the correct total for the entire domain unless special care is taken to include the pieces of the curve which lie between the sets. Provision for the inclusion of these pieces was therefore incorporated into the procedure for performing piecewise integrals.

The calculations of the Runge-Kutta program were all carried out in double precision arithmetic whereas the final integrations were carried out in single precision arithmetic. Because of this reduction in precision, occasionally two or more data points near the beginning of the trajectories were spaced so closely in distance that, in single precision they became equal. The spline algorithm used in the integrations requires that input data represent a function in the algebraic sense: for each abscissa there must be one and only one ordinate. When multiple ordinates were presented to the spline algorithm, and optional feature was invoked to discard all but the first of the multiple points. This was done rather than, say, taking an average value for the abscissae in order to preserve the lower limit of the integration.

CHAPTER FIVE

Presentation of Model Data

5.1 Introduction

The presentation of the various cases put to the model equations for solution will now be given. The two particles, whose trajectories were being determined, could be characterized by their charge and mass, and by their initial positions and velocities. The particle types used with the model studies include e^-, Li^+, Al^+, Ga^+, In^+, Bi^+, Bi^{+2} and Bi^{+3}.

The initial position of all particles in all test cases was a point lying on the emitter surface. For the sphere model studies, all particles were emitted from the same point on the sphere and traced colinear trajectories. Colinear studies were performed with the SOC model with trajectories lying on the axis of symmetry of the emitter, for comparison with the sphere model results. Emission points lying off the axis of symmetry were also tested with the SOC model.

Although the algorithm provided the capability for using non-zero initial radial and tangential velocities, this feature was not invoked in the present studies. The principal reason for studying initial velocity effects is the characterization of the virtual source size, as in the work of Weisner[54], and requires a large number of trajectory calculations. Multi-particle Monte-Carlo methods are better suited for this kind of study and were not attempted in the present work. Qualitatively, if particle 1 is given an initial radial velocity relatively greater than that of particle 2, then the effect would be similar to increasing the initial particle spacing. Directing the particles tangentially away from each other would have an effect similar to increasing their initial angular separation. Both of these examples would diminish the potential energy exchange and weaken the observed energy and radial beam spreading.

The electric potential models are characterized by the radius of the emitter, the electric field strength at the emitter surface, the emitter to collector separation and, in the case of the SOC model, by the values of n and γ, where, as discussed in Chapter 3, the parameter n selects from among the family of solutions for the SOC electric potential and γ is the ratio of the emitter axial radius to the radius of the core sphere. The ranges selected for each of these model parameters is discussed in the following paragraphs.

The emitter radii chosen for study range in value from 0.01 to 1.0 microns in accordance with the values used in electron field emitters and suspected in LMIS. Electric field strengths in the range of 0.05 to 1.0 V/Å were used paralleling practical values.

As mentioned previously, the values measured for the energy and angular beam broadening depend on the path length of the trajectories.

Although the location of the collector surface could be set to any position during the execution of the Runge-Kutta program, early studies with the sphere model indicated that nearly all of the potential energy stored in the system by virtue of the initial particle separations is converted to kinetic energy within about 10 microns of the emitter surface. An emitter-collector separation of 10 mm was therefore chosen to further guarantee that the energy exchange would be complete and was also chosen as representative of spacings in practical focusing systems. As will be shown, this distance is not sufficient for complete potential energy relaxation for all choices of n and γ for the SOC model. Nonetheless, the value of 10mm was used throughout these studies.

The SOC model parameters n and γ described above were determined for this work by comparing plots of the equipotential shapes to SEM micrographs of field emitter tips and optical photographs of the liquid surface of an LMIS during ion emission. For the field electron studies the selected values are $n = 0.15$ and $\gamma = 2.0$, while for the ion emission studies the values are $n = 0.5$ and $\gamma = 3.0$. Figure 5 compares the SOC equipotentials with the sphere model.

In addition to the parameters characterizing the electric potential models, other parameters that are controllable during execution of the trajectory calculation program include the particle mass and charge and the initial radial and angular separation between the particles. The program itself regards time as the fundamental independent parameter, and therefore provides the ability to measure the time between emission

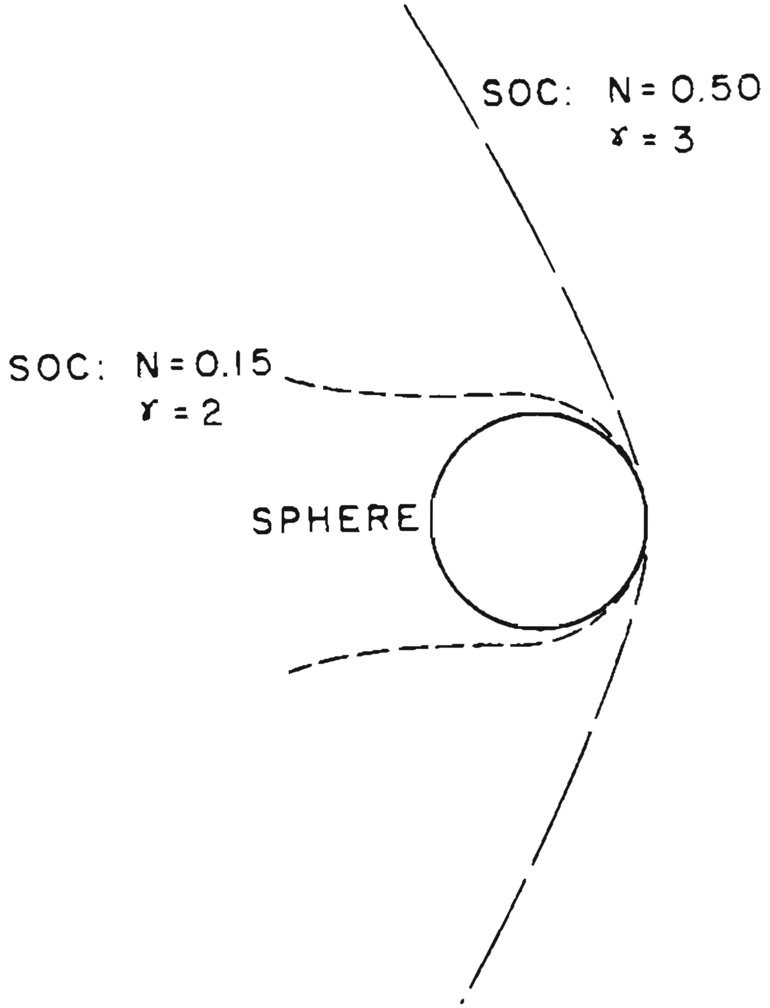
SOC: N = 0.50
γ = 3
SOC: N = 0.15
γ = 2
SPHERE

Figure 5. Emitter Profiles. This diagram compares the profiles of a sphere and two SOC emitters having the same apex radius.

events.

The remainder of this chapter is subdivided according to the model used: Section 5.2 covers sphere model results, Section 5.3 covers the SOC model results for non-colinear emission, and Section 5.4 covers the SOC model results for non-colinear emission. Within each section energy broadening data is presented first, followed by energy shift data. In Section 5.4 data for angular broadening is also presented after the energy shift data. Finally, within each of these subdivisions electron data is presented first, followed by data for Ga$^+$ ions (as representative of the ionic studies as a group) and then data showing the results for various ionic species are given. Discussion and interpretation of the data are reserved for Chapter 6.

5.2 Sphere Model Studies

The first electric field model investigated in this project was the sphere model described in Chapter 3. The primary objectives in this phase of the study were twofold: to develop the numerical methods for handling problems of this nature, and to compare the model results for the energy spread with experimental data published by Bell and Swanson[6] for electrons. Such parameters as total current, field strength and emitter radius were particularly of interest.

An unexpected result was obtained from the sphere model with respect to the observed shift in the peak position in the energy distribution measurements. The sphere model predicts that the exchange of energy between two particles is asymmetric: the first particle acquires more energy than the second particle loses when compared to the energy they each acquire as they traverse the electric potential field between the emitter and the collector surfaces.

The energy broadening data for electrons and for ions, which were also studied with the sphere model are presented in Section 5.2.1. The energy peak shift data are presented in Section 5.2.2.

5.2.1 Energy Broadening Studies

In Figure 6 the component of the energy spread contributed by the first emitted electron ΔE_1 as a function of its radial distance from the center of the emitting sphere is shown. Each of the curves shown represents data for a different initial inter-particle separation. The curve with the highest energy values derives from the shortest initial separation.

Figure 7 shows the total energy spread ΔE (from Equation (52)) for three different emitter radii, while Figure 8 presents similar data for four different values of emitter field strength.

Figure 9 is analogous to Figure 6 in showing the development of ΔE_1 with distance from the emitter, this time for the case of Ga^+ ion emission. Corresponding to Figures 7 - 8 are the data for Ga^+ ions presented in Figures 10 - 11, where the dependence of ΔE first on

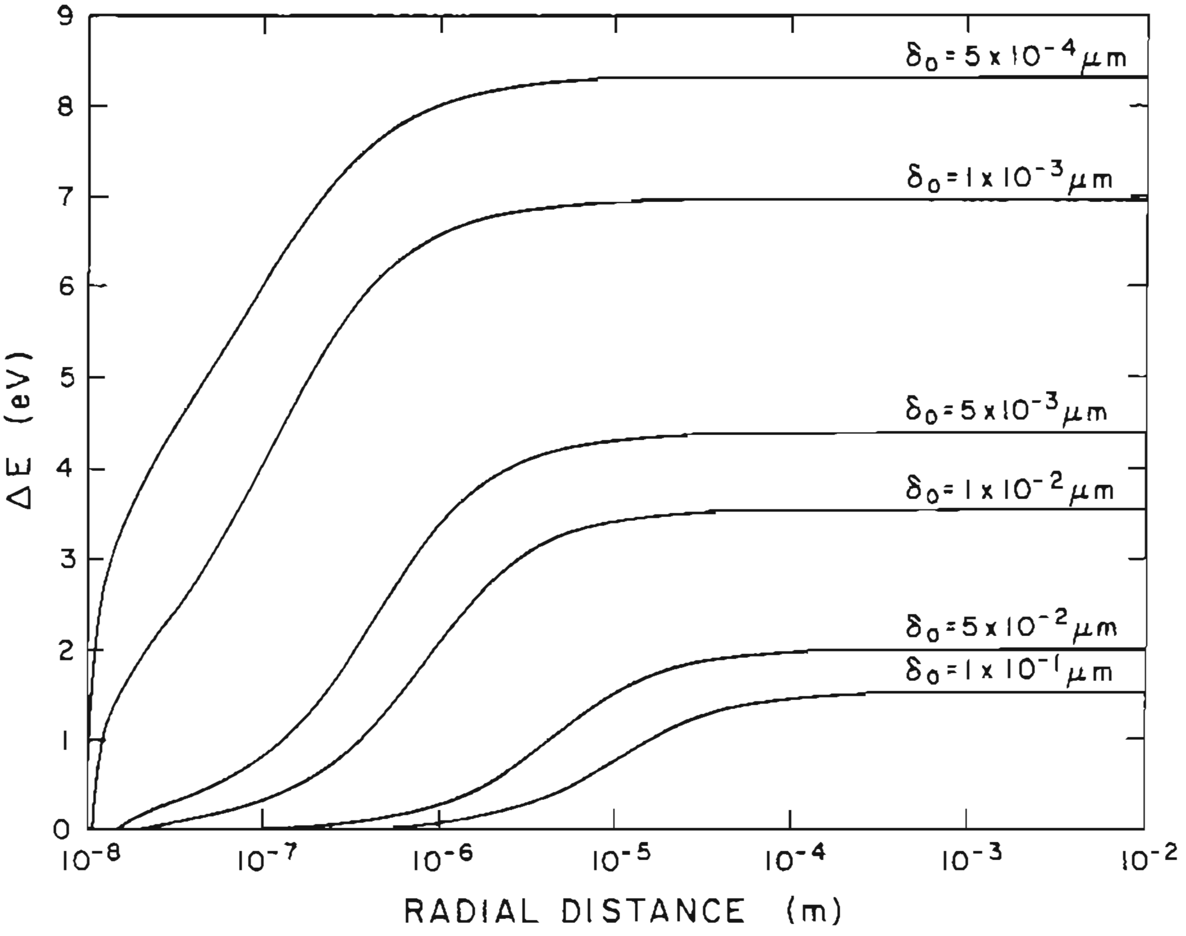

Figure 6. Sphere Model Electron Energy Spread vs. Distance. The contribution, ΔE_1, to the energy spread is shown as a function of distance for values of δ_0 ranging from 0.1μm to 5×10^{-4}μm. The data are for electrons with an emitter electric field strength of F_0=1.0V/Å on a sphere of radius r_a=0.01μm.

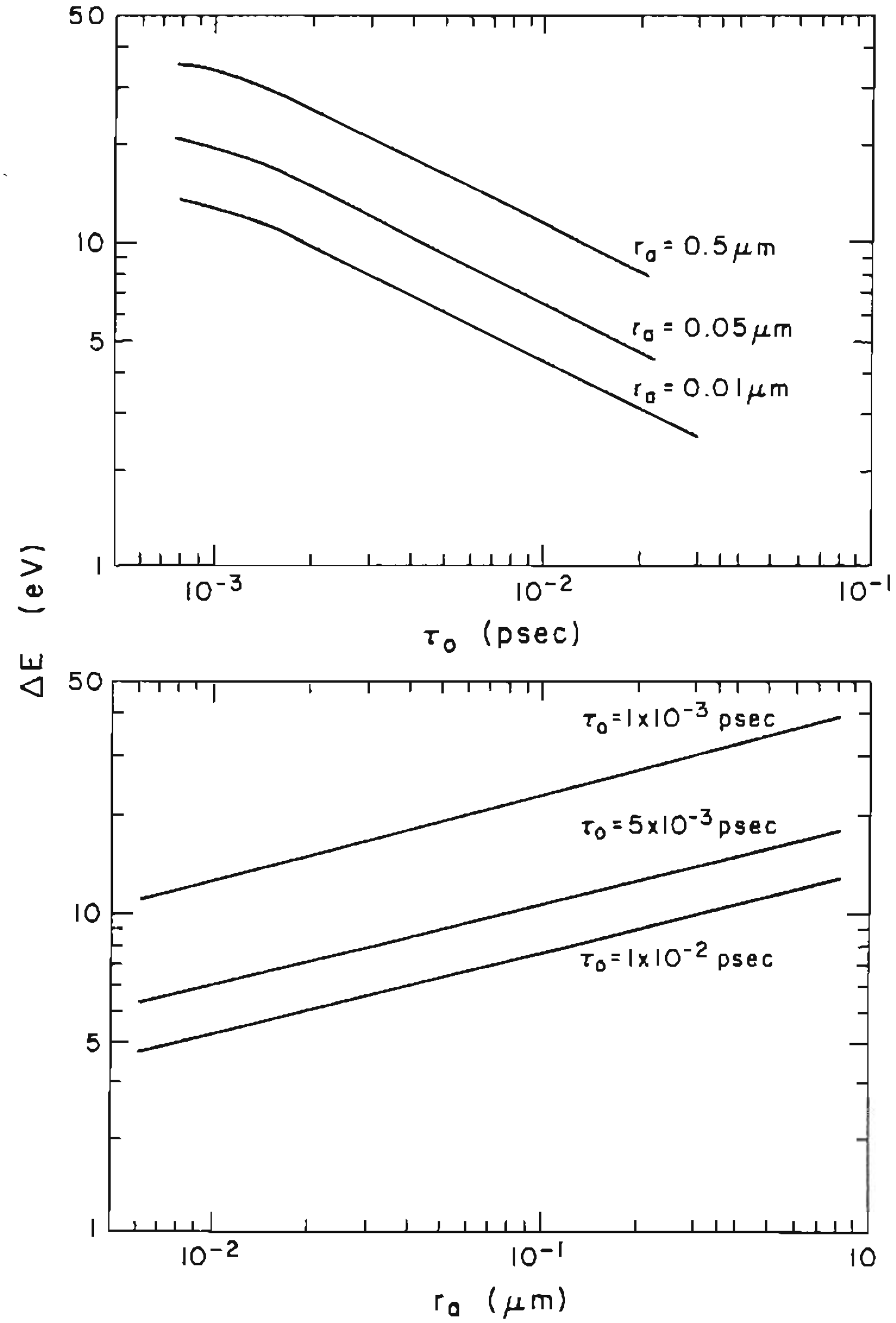

Figure 7. Sphere Model Electron Energy Spread vs. Emitter Radius. Total energy spread data for spheres of radius r_a=0.5, 0.05 and 0.01μm with F_0=1.0V/Å are shown.

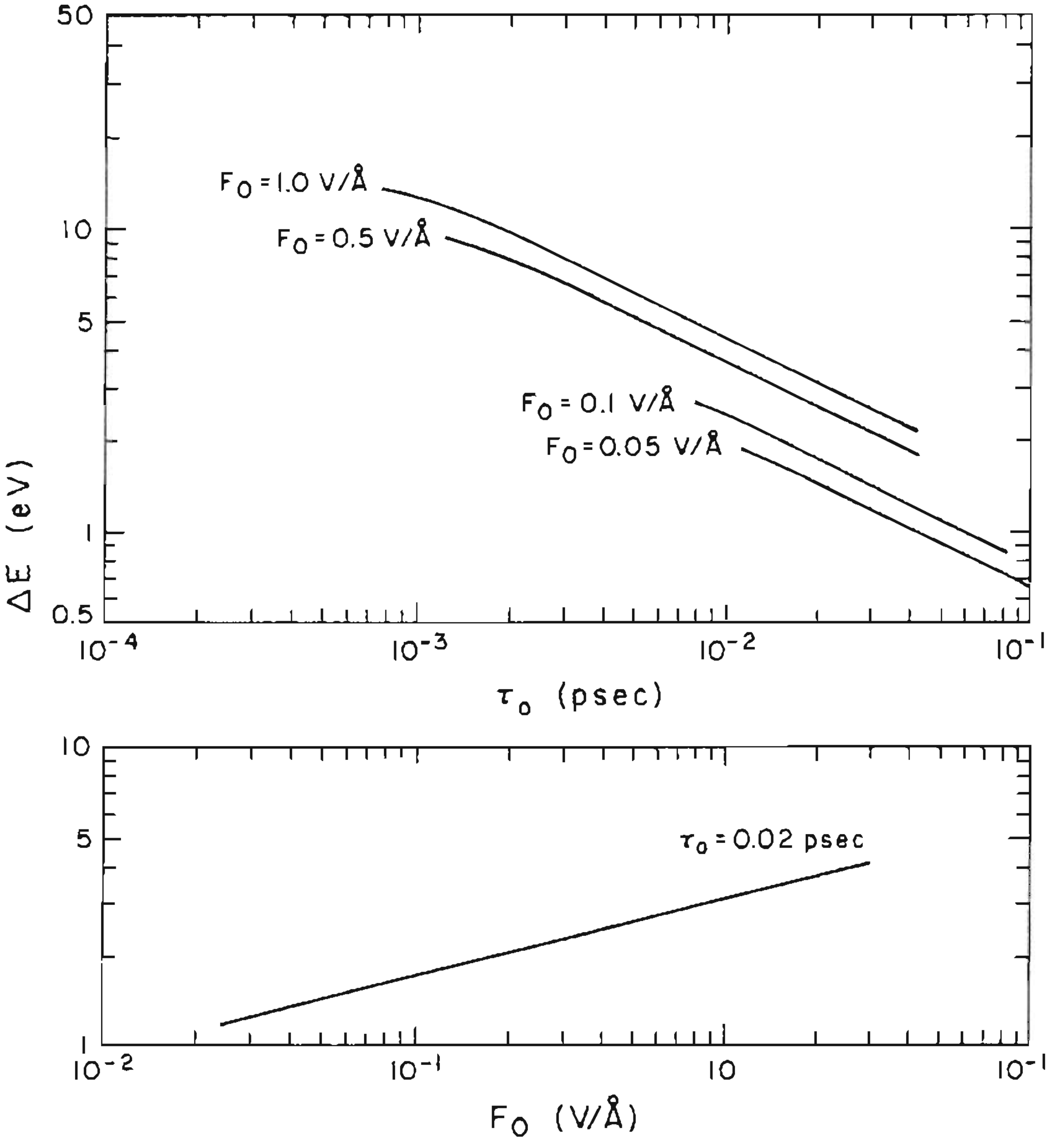

Figure 8. Sphere Model Electron Energy Spread vs. Field Strength. Total energy spread data for a sphere of radius r_a=0.01μm and field strengths of F_0=1.0, 0.5, 0.1 and 0.05V/Å are shown.

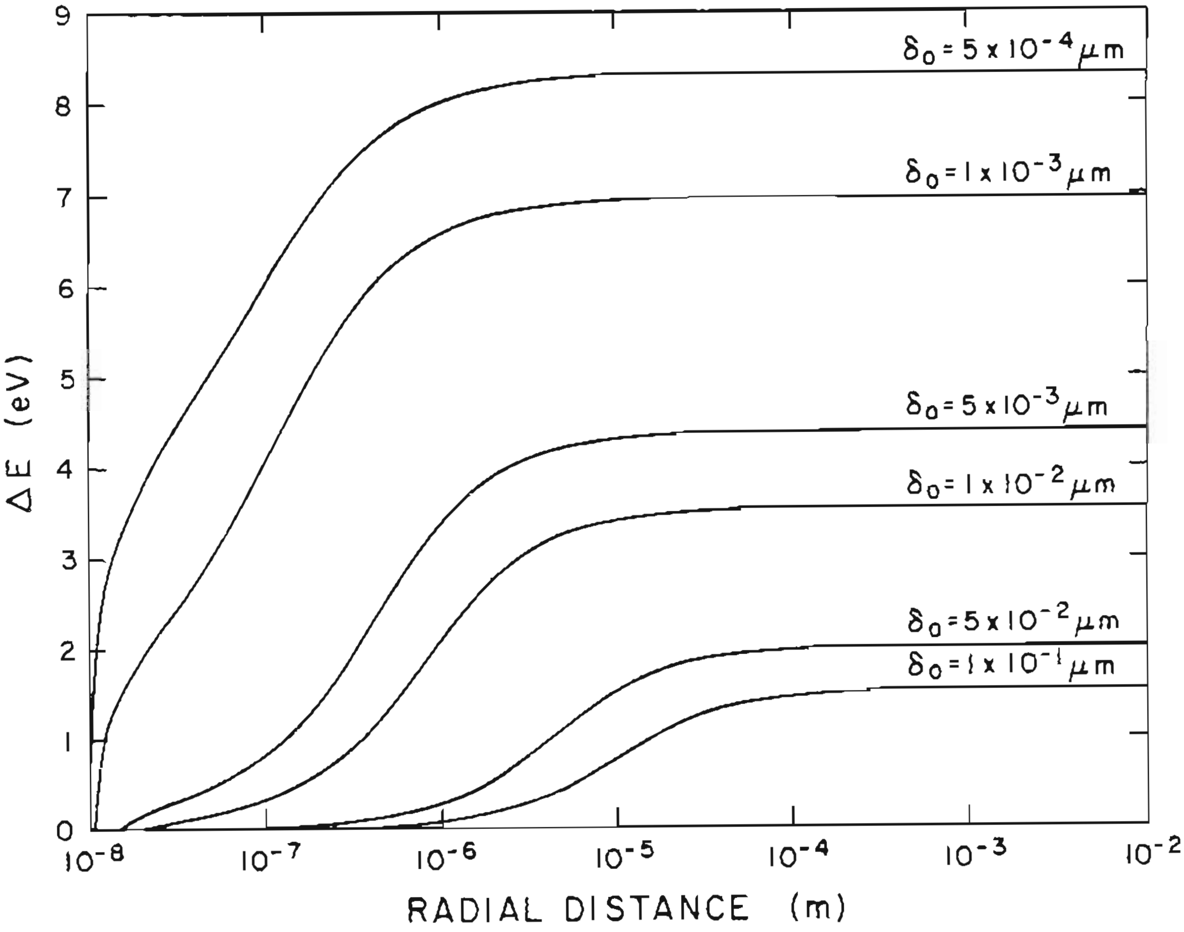

Figure 9. Sphere Model Ga^+ Energy Spread vs. Distance. The contribution, ΔE_1, to the energy spread is shown as a function of distance for values of δ_0 ranging from 0.1μm to 5×10^{-4} μm. The data are for gallium ions with an emitter electric field strength of F_0=1.0V/Å on a sphere of radius r_a=0.01μm.

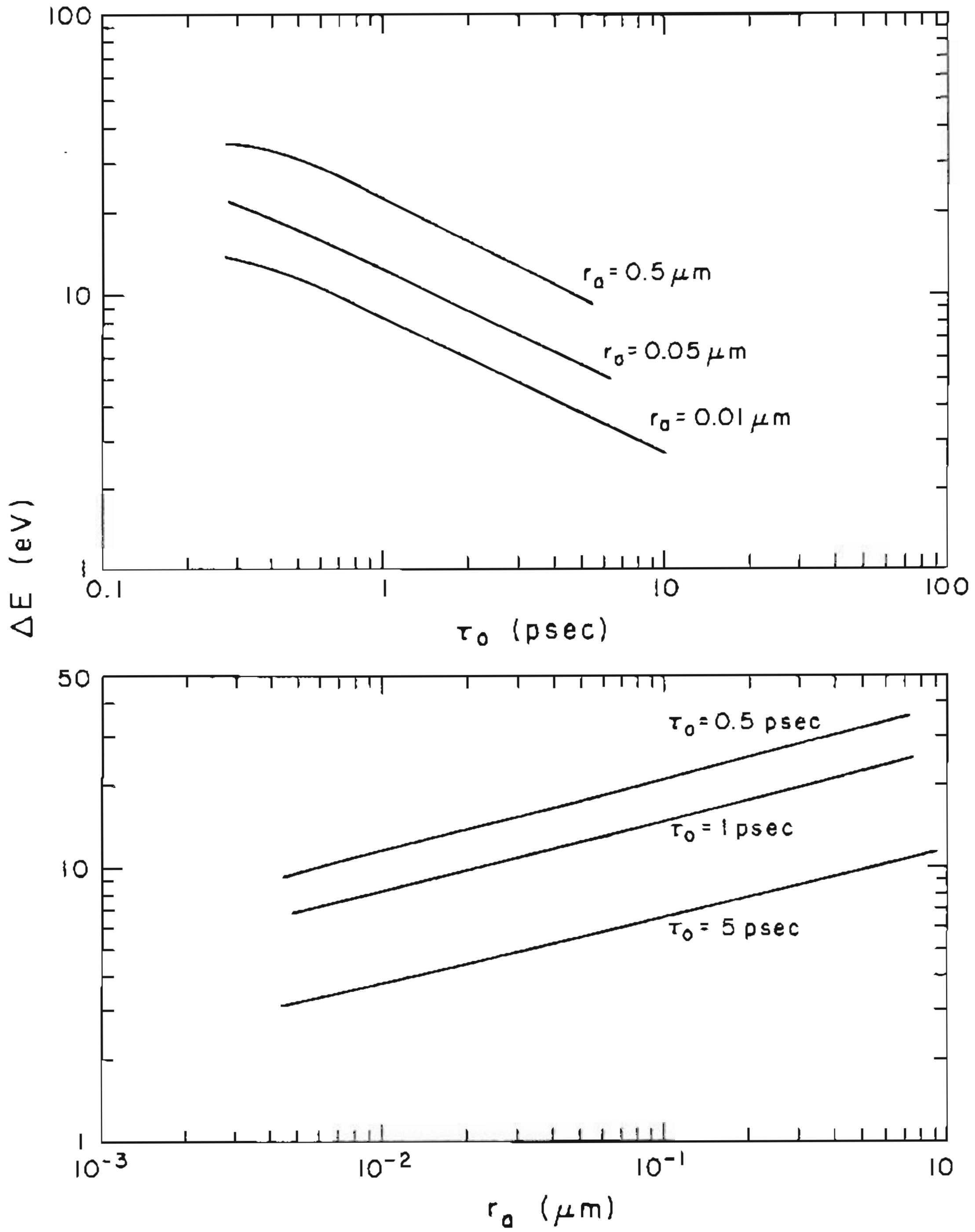

Figure 10. Sphere Model Ga^+ Energy Spread vs. Emitter Radius. Total energy spread data for spheres of radius r_a=0.5, 0.05 and 0.01μm with F_0=1.0V/Å are shown.

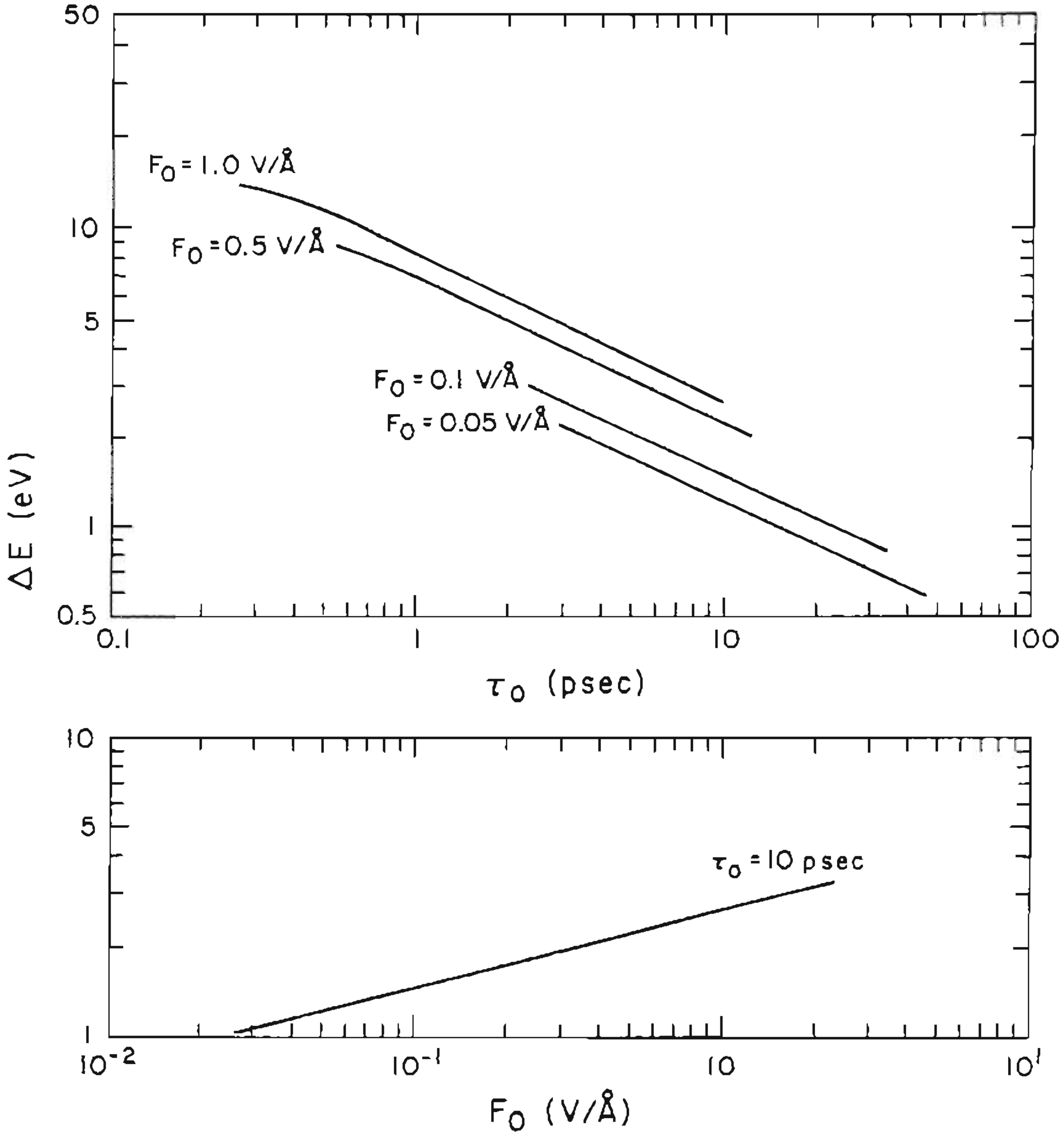

Figure 11. Sphere Model Ga^+ Energy Spread vs. Field Strength. Total energy spread data for a sphere of radius r_a=0.01µm and field strengths of F_0=1.0, 0.5, 0.1 and 0.05V/Å are shown.

emitter radius and then on emitter field strength are shown.

Choosing an emitter radius of 0.01 microns and a field strength of 1.0V/Å, results in the data of Figure 12 which shows the dependence of ΔE on the mass. Figure 13 shows ΔE as a function of the interevent time for four combinations of charge species. In this case bismuth ions were used. The four combinations shown, in order from lowest to highest curve are (+2,+1), (+1,+1), (+2,+2) and (+1,+2) where the first number in each ordered pair represents the charge on the first particle and the second represents the charge on the second particle emitted.

5.2.2 Average Energy Shift Studies

In this section data is presented on the shifts in the energy peak as functions of various parameters of interest. The change in the average kinetic energy of the two particle system is

$$\Phi = (\Delta E_1 + \Delta E_2)/2$$

Figure 14 is a plot of Φ as a function of distance from the center of the emitting sphere for the case where the sphere radius is 0.01 microns and the field strength is 1.0V/Å.

The data provided by the sphere model program show that the average energy shift Φ is independent of the emitting sphere radius, and therefore plots of the energy shift for various sphere radii will be omitted.

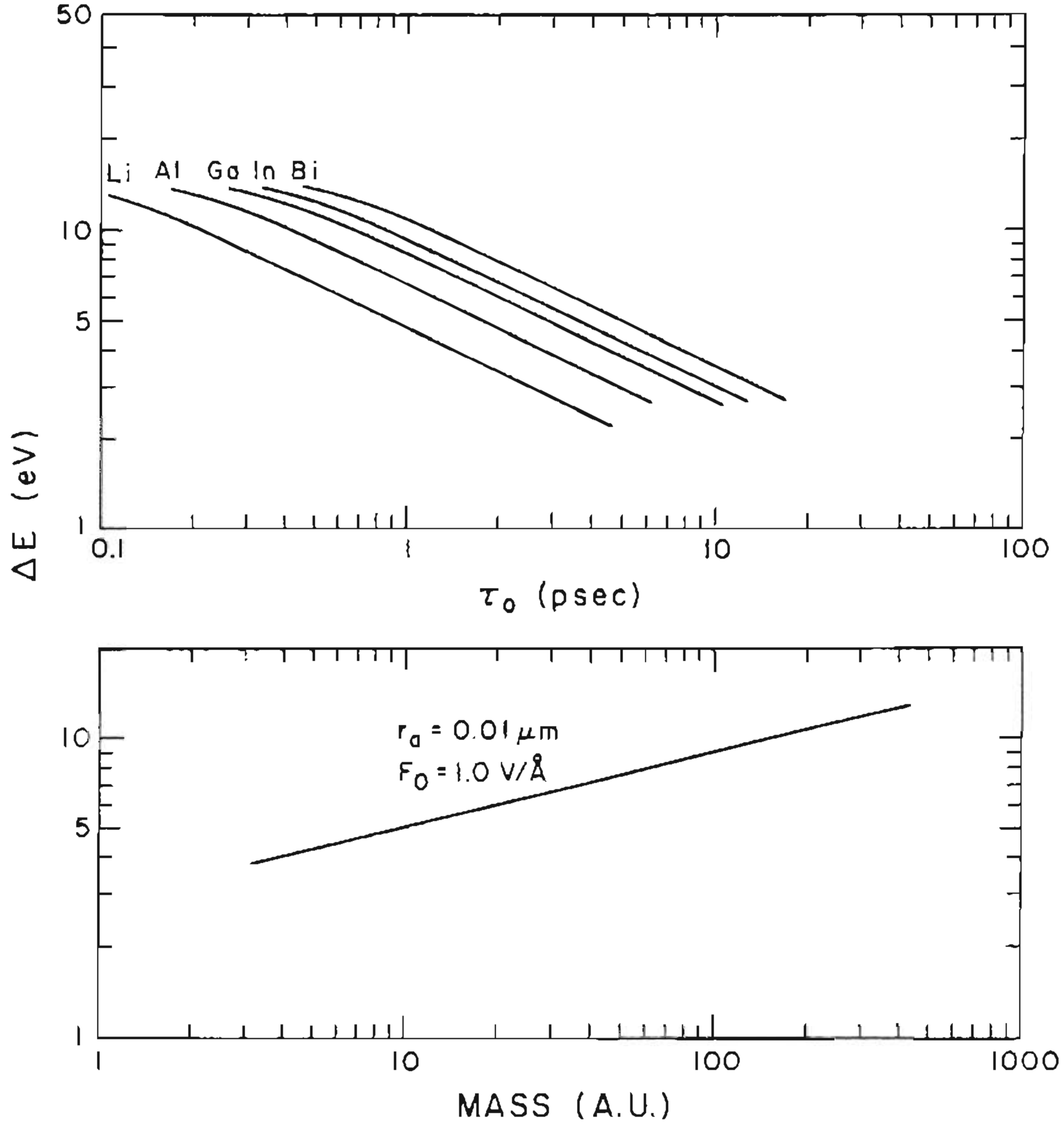

Figure 12. Sphere Model Energy Spread vs. Ionic Mass. Total energy spread data for the five ionic species Li^+, Al^+, Ga^+, In^+ and Bi^+ are plotted. An emitting sphere of radius r_a=0.01μm with a field strength of F_0=1.0V/Å was used.

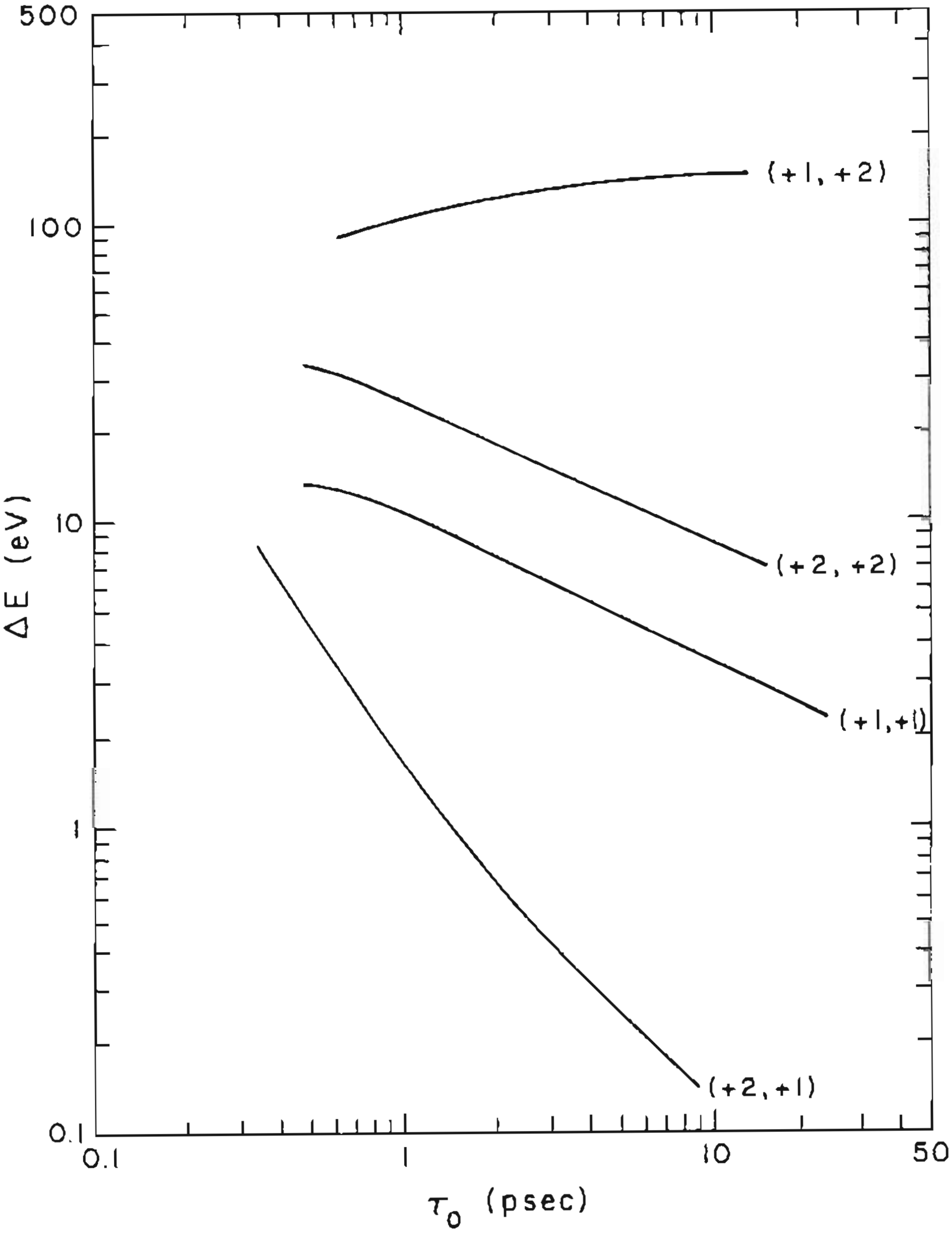

Figure 13. Sphere Model Energy Spread vs. Charge. Total energy spread data for four combinations of bismuth charge species are presented. A sphere of radius r_a=0.01µm with a field strength of F_0=1.0V/Å was used. The charged pairs shown are (n_1,n_2)=(+1,+1), (+1,+2), (+2,+1) and (+2,+2).

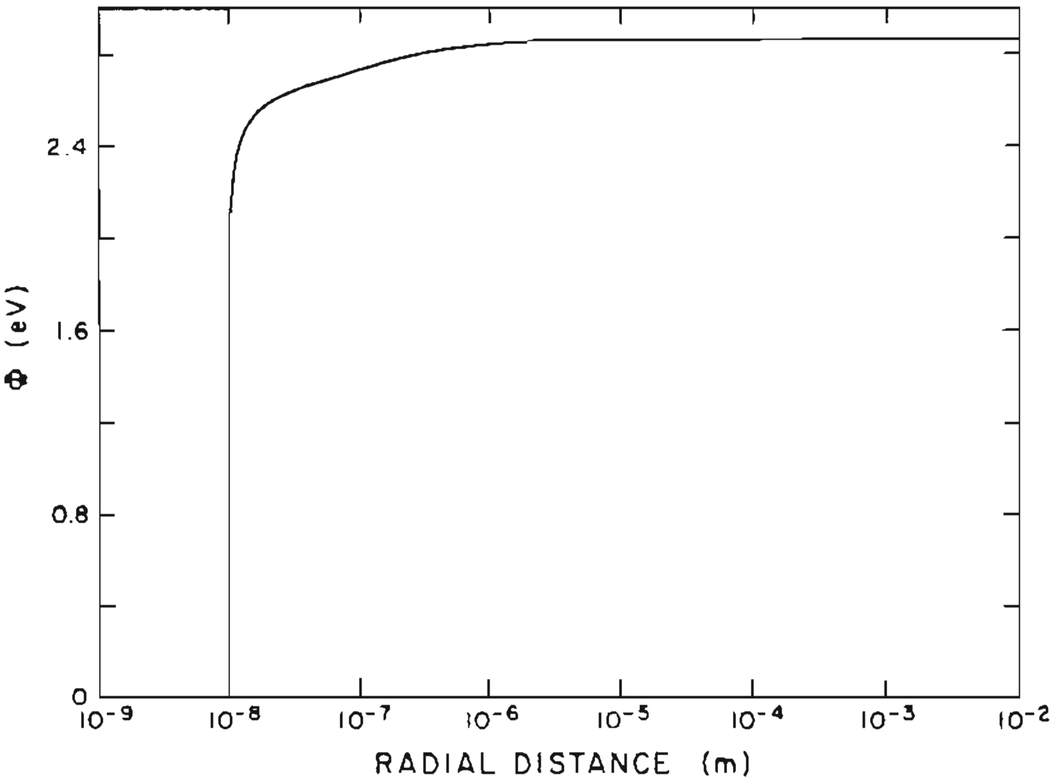

Figure 14. Sphere Model Energy Shift vs. Distance. The energy shift, Φ, is shown as a function of distance for δ_0=5Å. The data are for gallium ions with an emitter electric field strength of F_0=1.0V/Å on a sphere of radius r_a=0.01μm.

Figure 15 shows Φ for four values of emitter field strength at an emitter radius of 0.01 microns.

The shape of the curve for the energy shift experienced by the first Ga^+ ion as a function of radial distance from the emitter center is exactly the same as the electron curve, and therefore will not be shown separately.

Figure 16 presents the average energy shift as a function of the interevent time for ions of five different masses. The inset shows the dependence of Φ on mass at an interevent time of 1.0 picosecond.

Figure 17 shows Φ for bismuth with charges of (+1,+1), (+2,+1) and (+2,+2).

5.3 SOC Model Studies I: Colinear Emission

The first enhancement to the model calculations was the incorporation of a more realistic equipotential model for the emitting surface. The Sphere-on-Orthogonal-Cone equipotential model has been described in detail in Chapter 3. A major purpose of this part of the study was to determine the effect of including the emitter shank on the pairwise model results. Therefore, the same series of model experiments were conducted using the SOC model program that were conducted with the sphere model program. As before, the energy broadening ΔE data will be presented first and then the average energy peak shift data Φ.

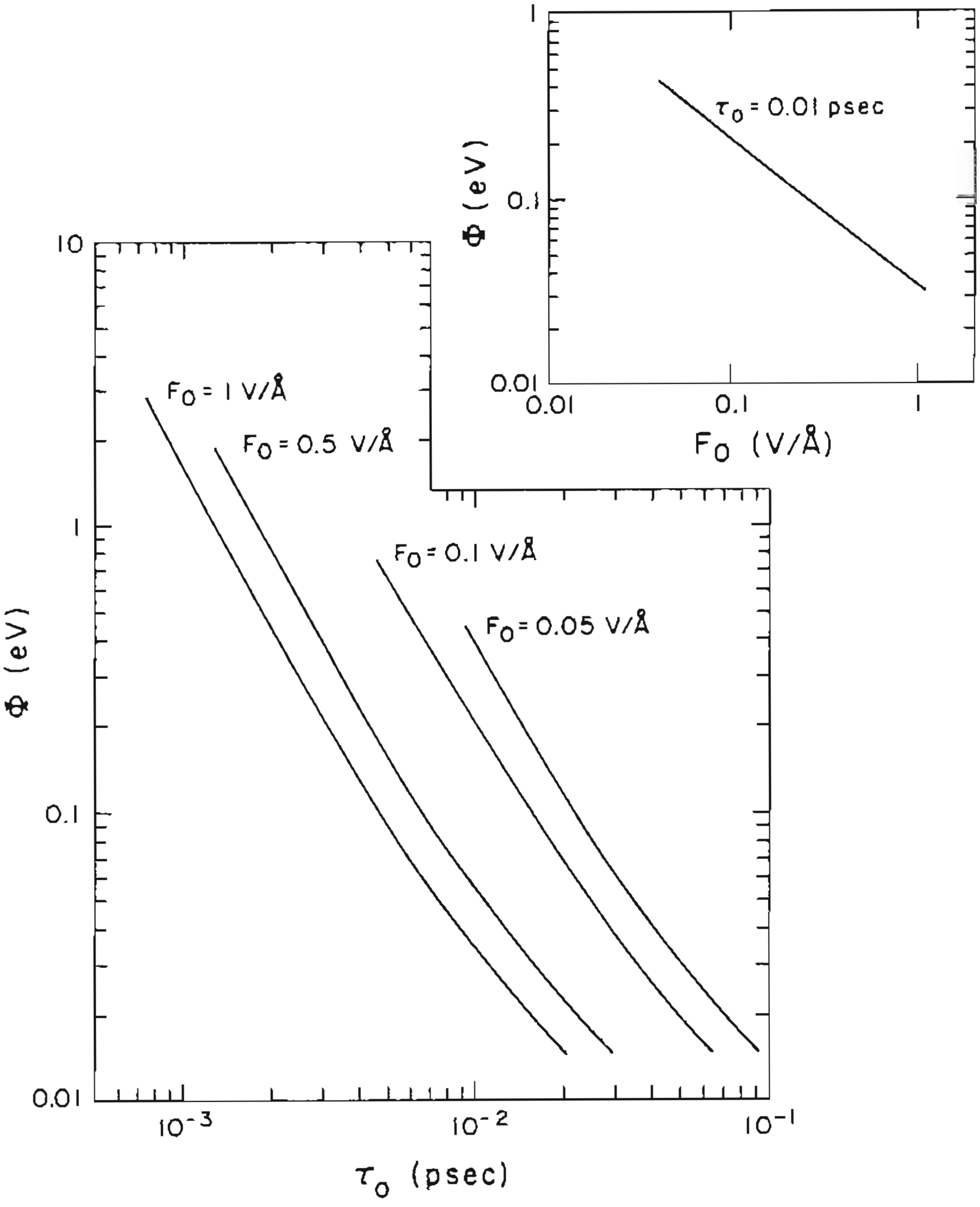

Figure 15. Sphere Model Electon Energy Shift vs. Field Strength. The energy shift data for a sphere of radius r_a=0.01μm and field strengths of F_0=1.0, 0.5, 0.1 and 0.05V/Å are shown.

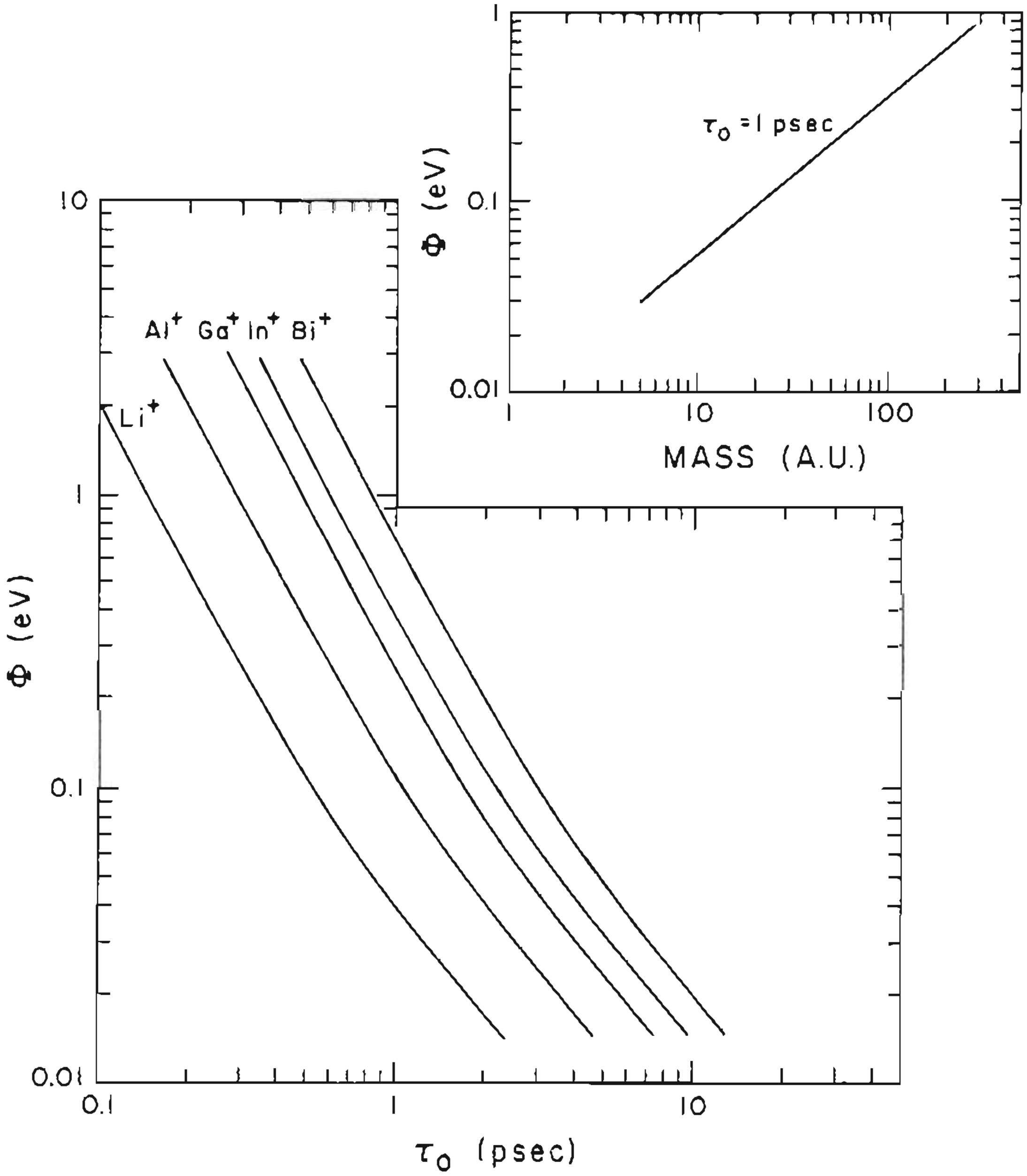

Figure 16. Sphere Model Energy Shift vs. Ionic Mass. The energy shift data for the five ionic species Li$^+$, Al$^+$, Ga$^+$, In$^+$ and Bi$^+$ are shown. An emitting sphere of radius r_a=0.01μm with a field strength of F_0=1.0V/Å was used.

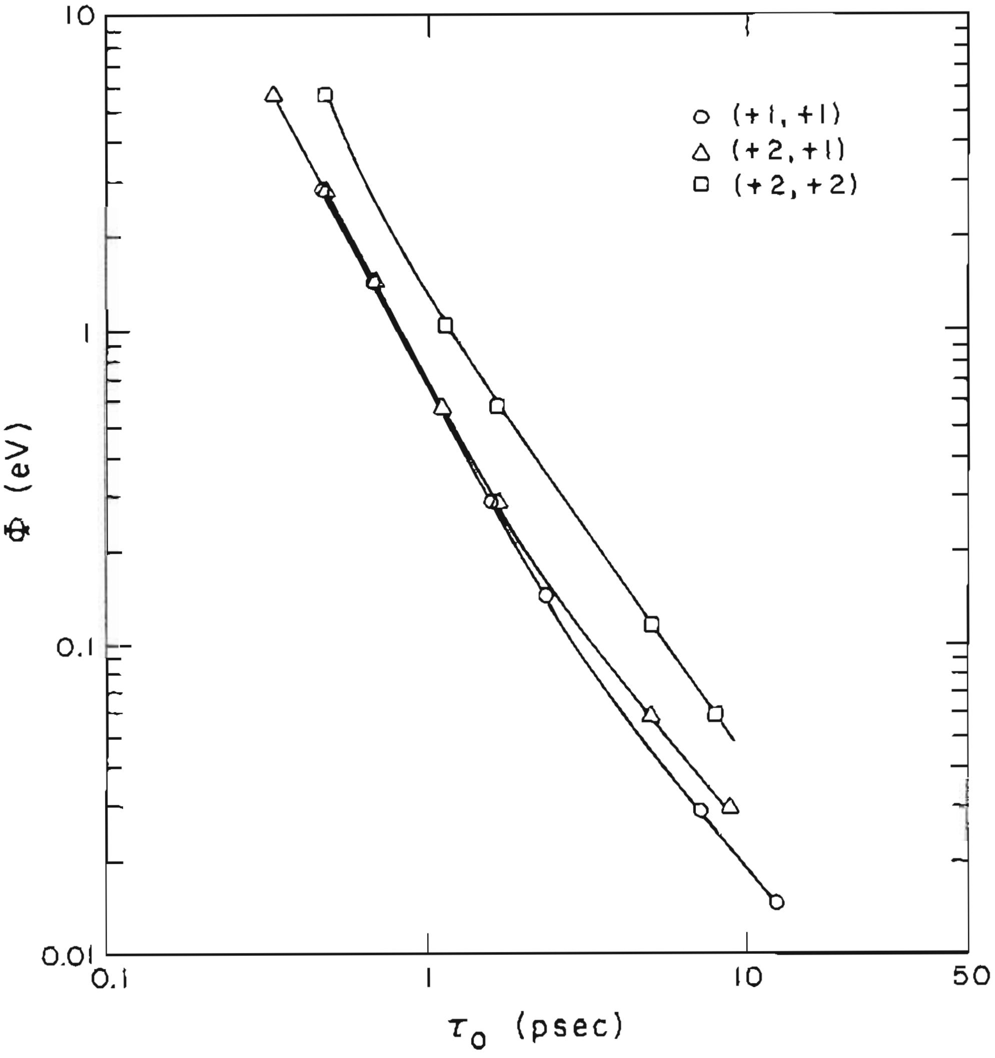

Figure 17. Sphere Model Energy Shift vs. Charge. The energy shift data for three combinations of bismuth charge species are presented. A sphere of radius r_a=0.01μm with a field strength of F_0=1.0V/Å was used. The charged pairs shown are (n_1,n_2)=(+1,+1), (+2,+1) and (+2,+2).

5.3.1 Energy Broadening Studies

Figure 18 shows the component of the total energy spread contributed by the first emitted electron as a function of its radial distance from the center of the core sphere. The values of n and γ for the electron model are 0.15 and 2.0 respectively. As in Figure 6, the curve with the highest energy values derives from the calculations using the smallest initial separation.

Figure 19 presents ΔE for electrons for three different emitter radii at a field strength of 1.0 V/Å. Figure 20 shows the ΔE results for four different values of the field strength at an emitter radius of 0.01 microns.

Turning to the data modeling the liquid metal ion emission, Figure 21 shows the component of the energy spread contributed by the first Ga^+ ion as a function of its radial distance from the center of the core sphere. The values of n and γ for this and all the ion studies are 0.5 and 3.0 respectively. Once again, the curve with the highest energy values derives from the calculations using the shortest initial separation. However, in contrast to the sphere model results of Figure 9, the value of ΔE_1 continues to increase with radial distance.

Figure 22 presents ΔE data for four different emitter radii at a field strength of 1.0 V/Å. Figure 23 presents the ΔE results for four different

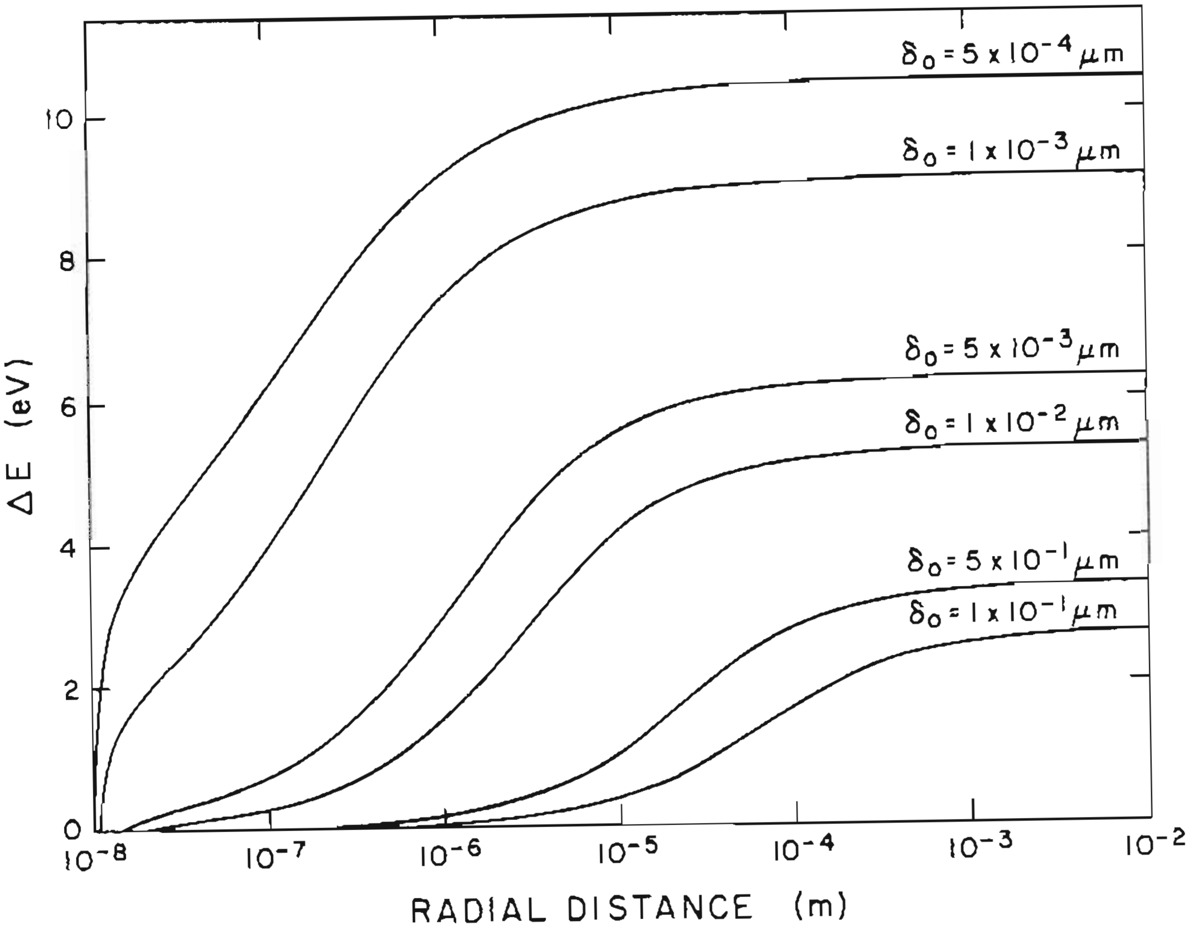

Figure 18. SOC Model Electron Energy Spread vs. Distance. The contribution, ΔE_1, to the energy spread is shown as a function of distance for values of δ_0 ranging from 0.1μm to 5×10^{-4}μm. The data are for electrons emitting from a SOC tip with r_a=0.01μm, n=0.15, γ=2.0 and F_0=1V/Å.

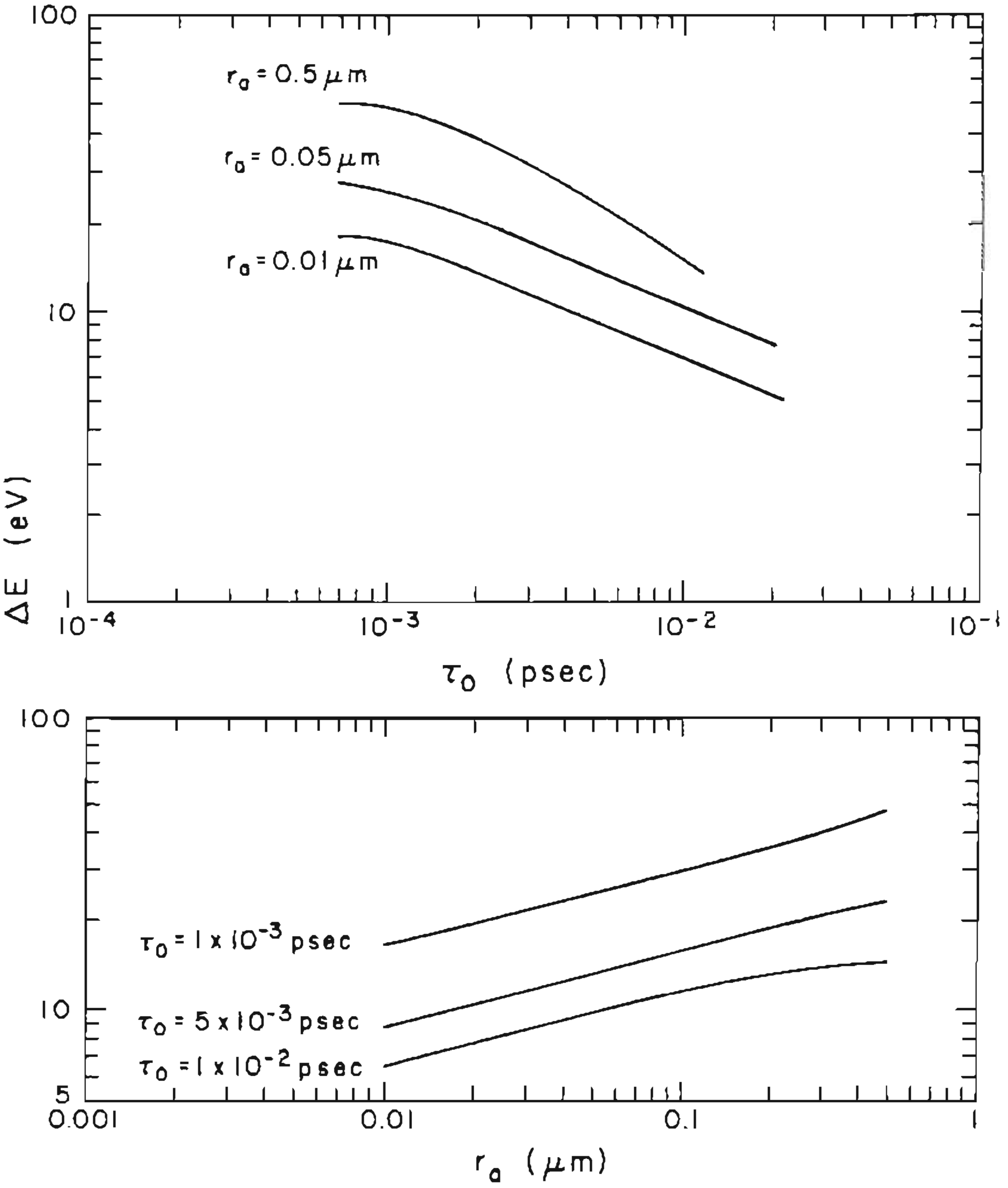

Figure 19. SOC Model Electron Energy Spread vs. Emitter Radius. Total energy spread data for SOC emitters of apex radius r_a=0.5. 0.05 and 0.01μm are shown. Other parameters are n=0.15, γ=2.0 and F_0=1V/Å.

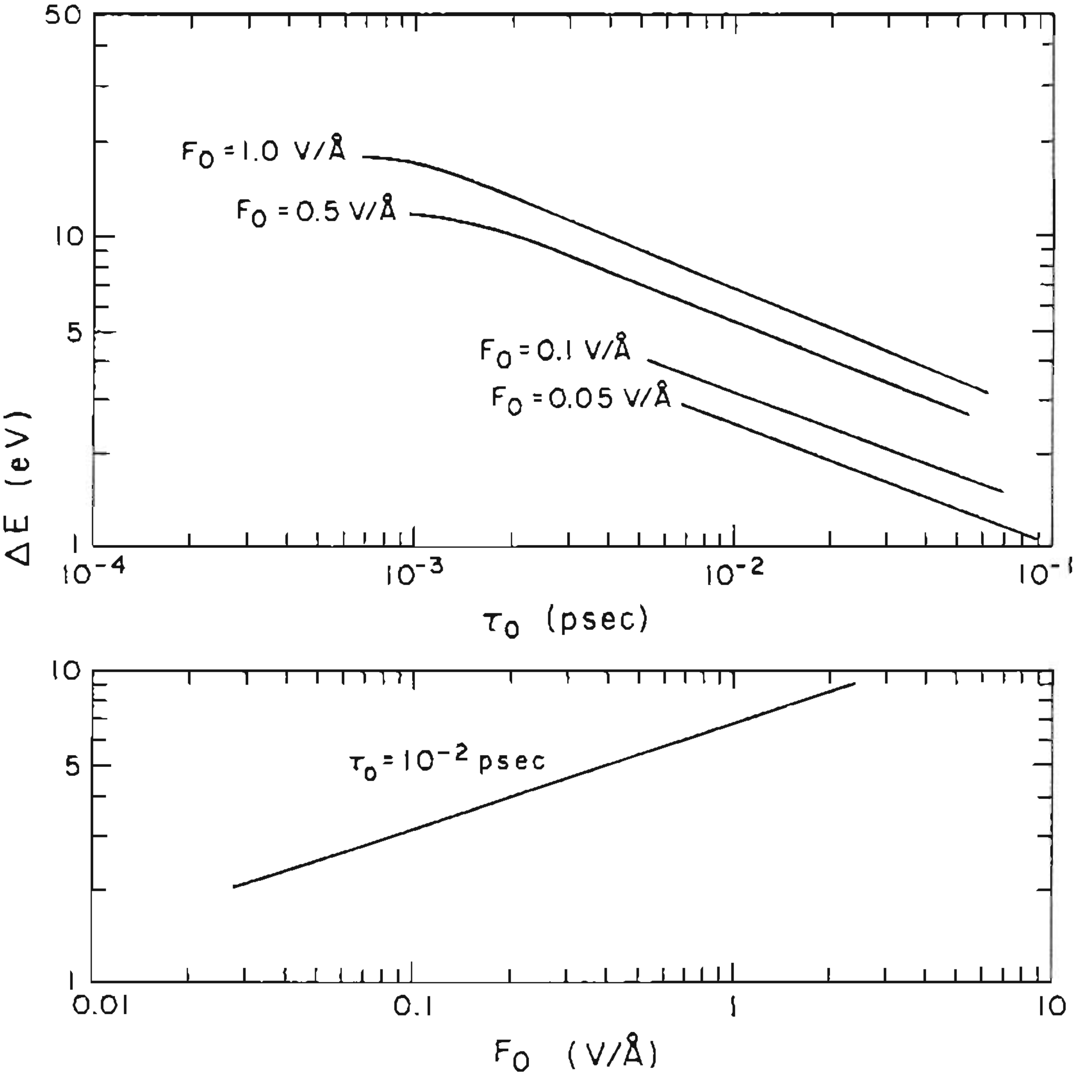

Figure 20. SOC Model Electron Energy Spread vs. Field Strength. Total energy spread data for an SOC emitter of n=0.15, γ=2.0 and r_a=0.01µm and field strengths of F_0=1.0, 0.5, 0.1 and 0.05V/Å are shown.

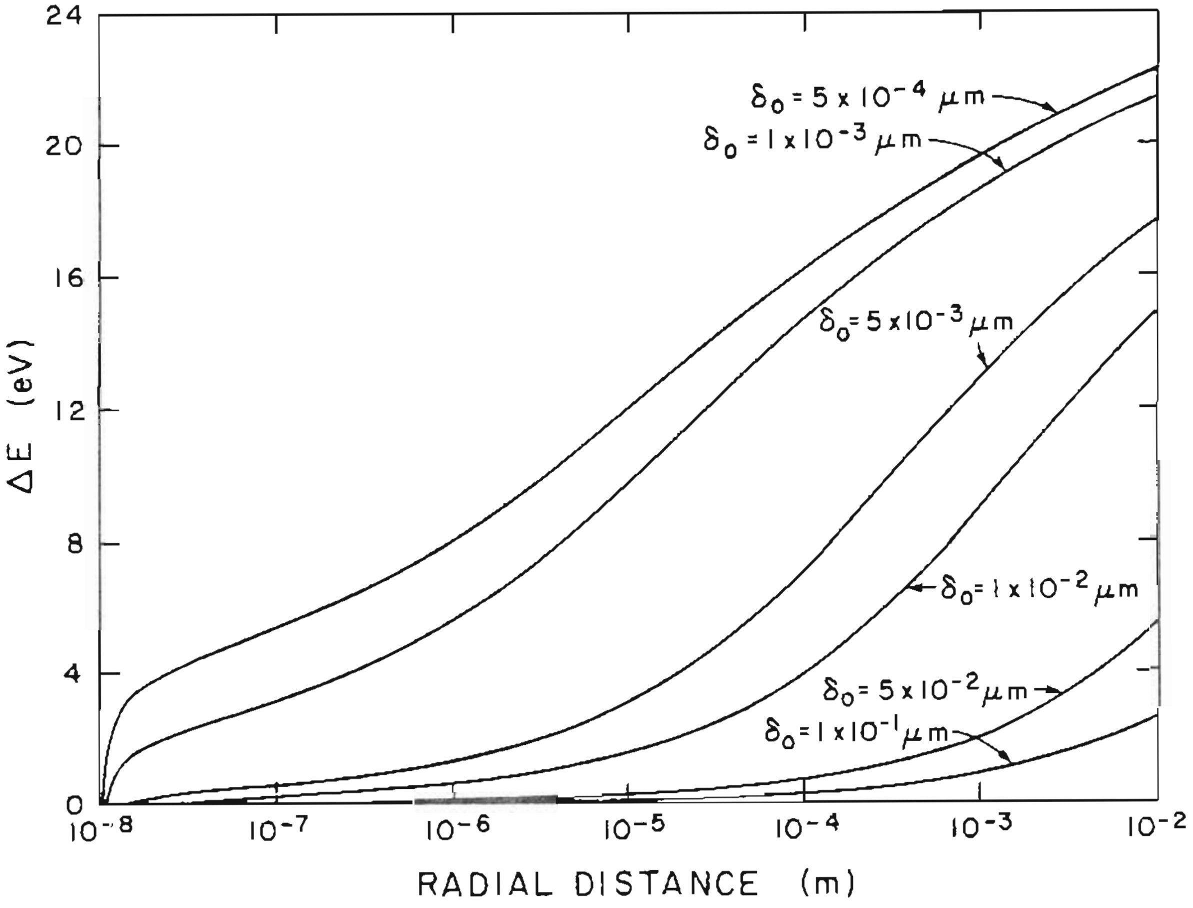

Figure 21. SOC Model Ga^+ Energy Spread vs. Distance. The contribution, ΔE_1, of the first emitted Ga^+ ion to the energy spread is shown as a function of distance for values of δ_0 ranging from 0.1 to $5\times10^{-4}\mu m$. Emitter parameters of r_a=0.01μm, n=0.5, γ=3.0 and F_0=1.0V/Å were used.

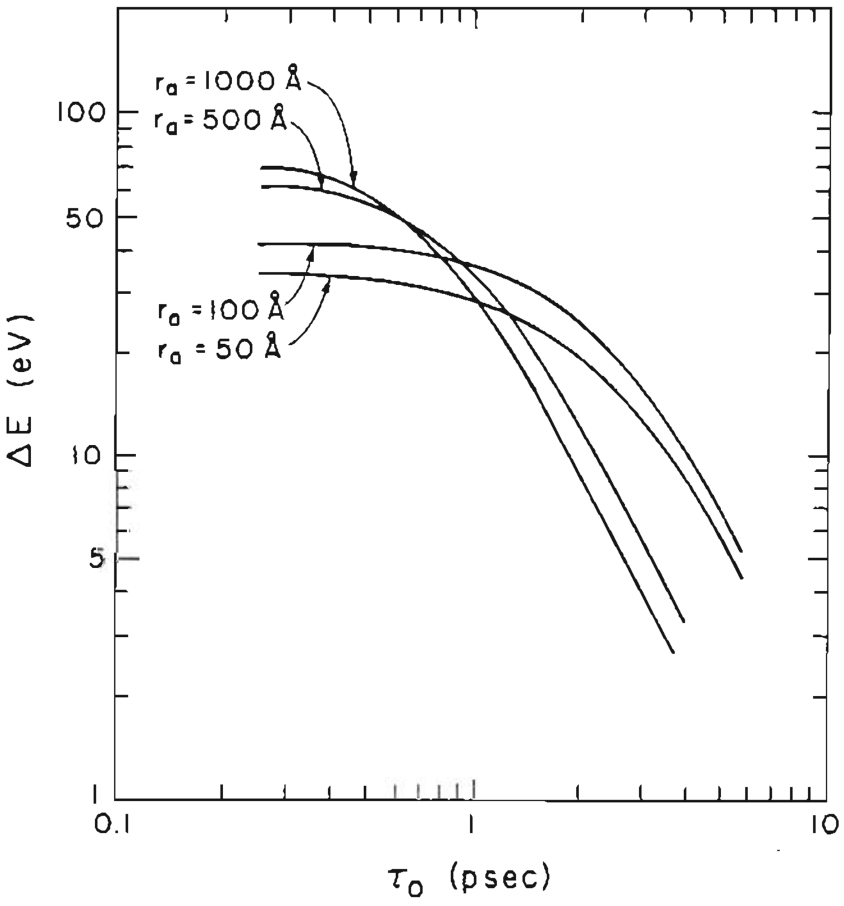

Figure 22. SOC Model Ga^+ Energy Spread vs. Emitter Radius. Total energy spread data for SOC emitters of apex radius r_a=0.5, 0.05 and 0.01μm, n=0.5, γ=3.0 and F_0=1.0V/Å are shown.

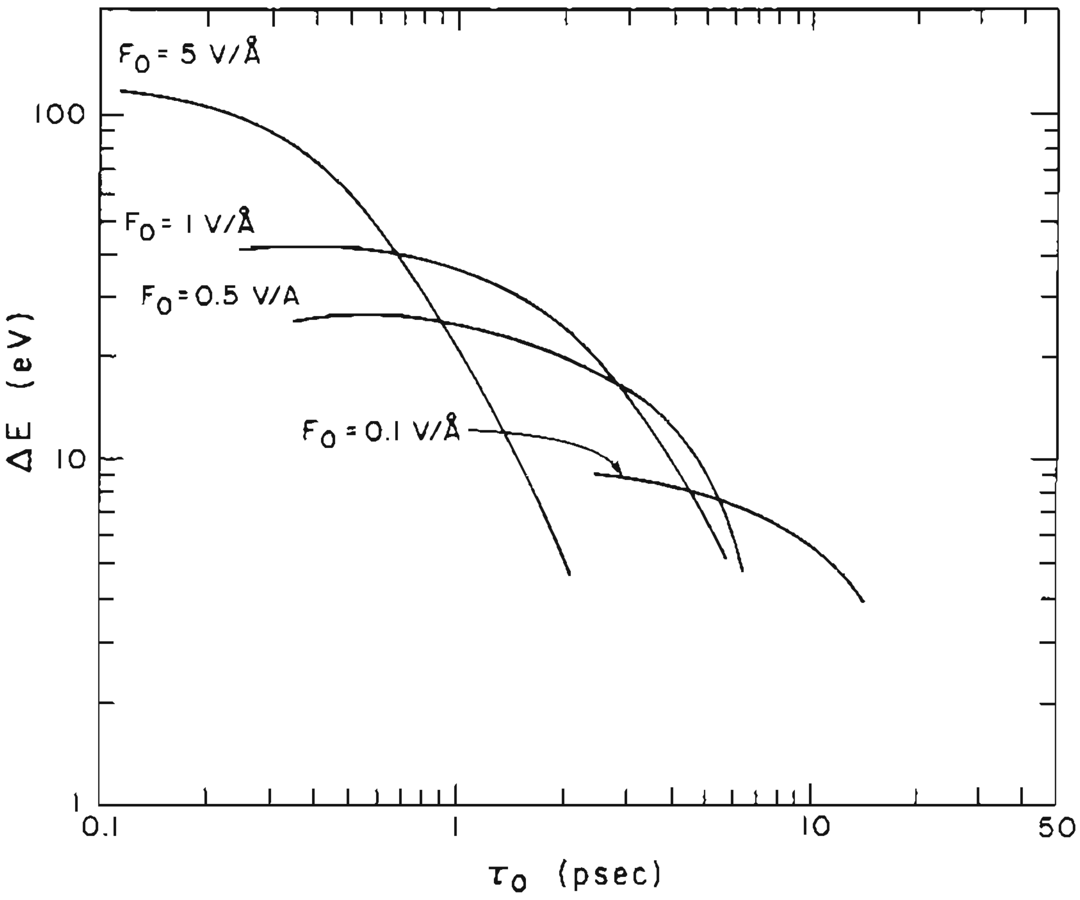

Figure 23. SOC Model Ga^+ Energy Spread vs. Field Strength. Total energy spread data for a SOC emitter of r_a=0.01µm, n=0.5, γ=3.0 and field strengths of F_0=5.0, 1.0, 0.5, and 0.1V/Å are shown.

values of the field strength for an emitter radius of 0.01 microns. Both of these graphs show data for Ga^+ ions.

The effect of mass on ΔE is shown in Figure 24 where curves for Li^+, Al^+, Ga^+, In^+ and Bi^+ are displayed. As before the values for the emitter radius and field strength for these graphs are 0.01 microns and 1.0 V/Å, respectively.

Figure 25 shows the energy spread as a function of the interevent time for six combinations of charge using bismuth ions. In this graph, unlike the data presented in Figure 13, the charge species included all combinations of +1, +2 and +3 ionic species.

5.3.2 Average Energy Shift Studies

The shift in the average energy was measured for the SOC model data as well as for the sphere model data. The sphere model data revealed that Φ is independent of the emitting sphere radius. The SOC model further shows that Φ is insensitive to emitter shape, at least for the two emitter equipotentials used in this study. Figure 26 shows Φ as a function of distance from the center of the core sphere for Ga^+ ions. The shape of the curve for electrons is essentially the same. The radius of curvature at the emitter apex was 0.01 microns, and the field strength on the emitter was 1.0V/Å for these data.

Figure 27 shows Φ for electrons at four values of field strength for an emitter of apex radius r_a=0.01 microns. Figure 28 shows Φ as a

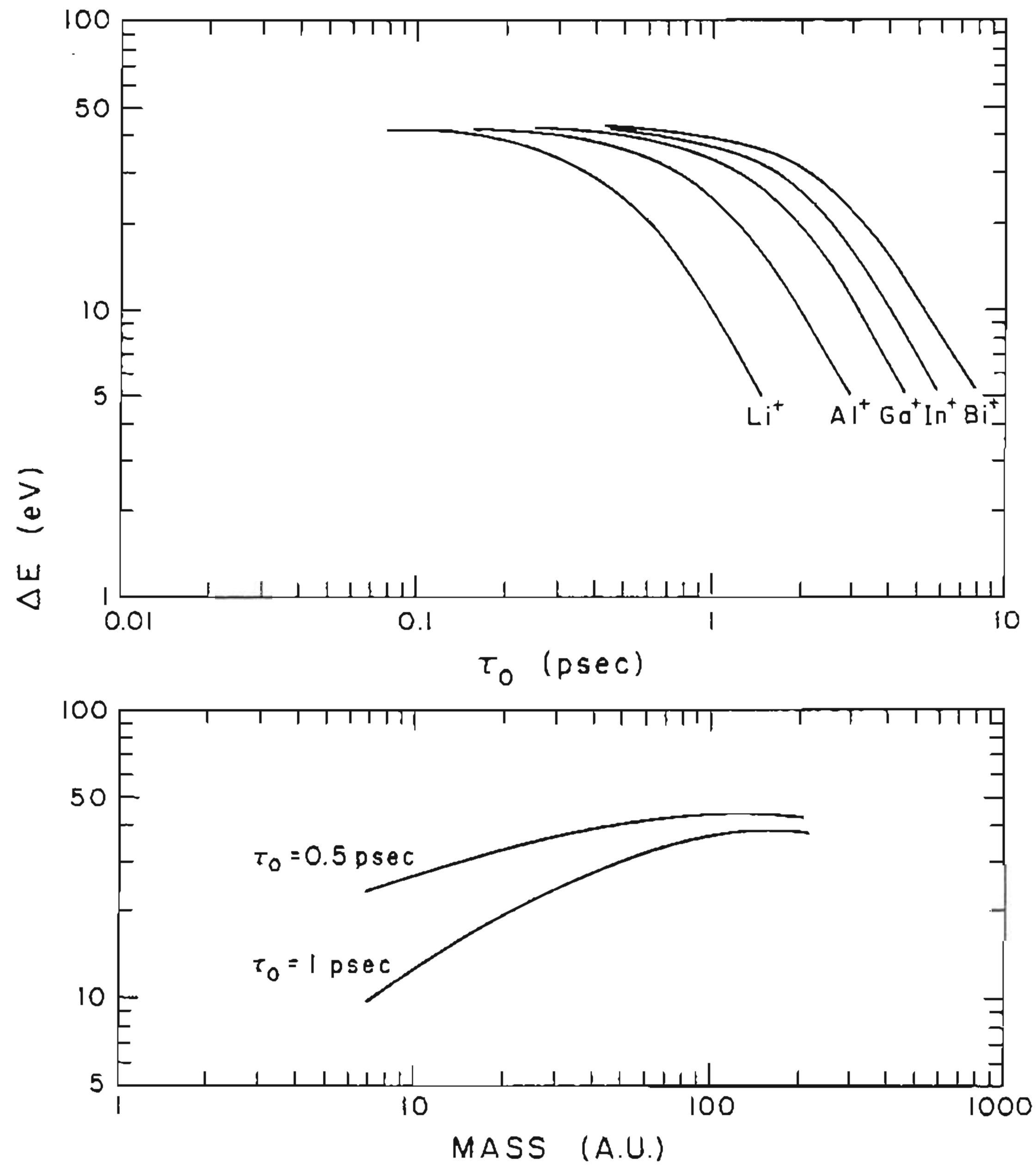

Figure 24. SOC Model Energy Spread vs. Ionic Mass. Total energy spread data for the five ionic species Li^+, Al^+, Ga^+, In^+ and Bi^+ are plotted. An SOC emitter of r_a=0.01µm, n=0.5, γ=3.0 and F_0=1.0V/Å was used.

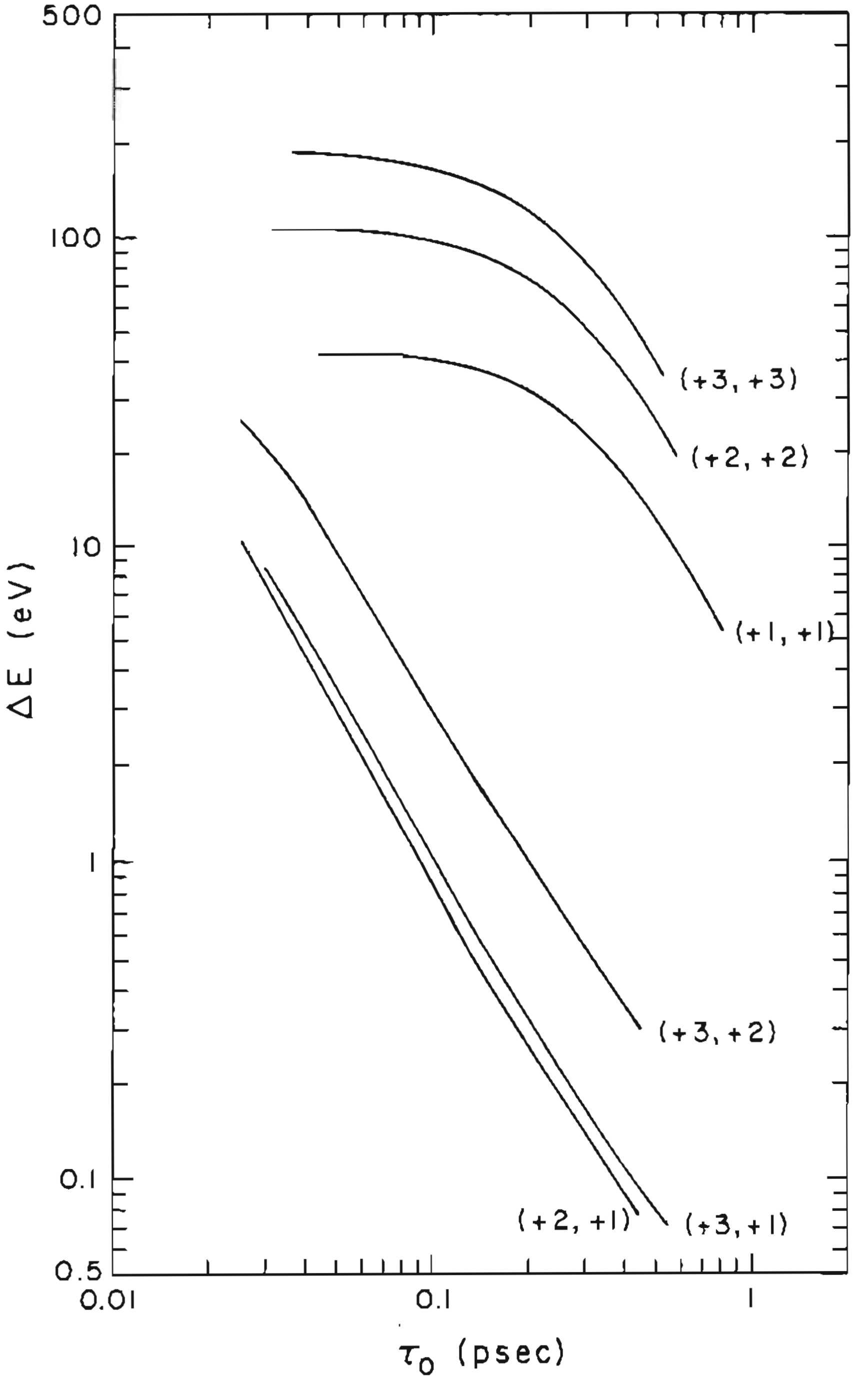

Figure 25. SOC Model Energy Spread vs. Charge. Total energy spread data for six combinations of bismuth charge species are presented. An SOC emitter of r_a=0.01µm, n=0.5, γ=3 0 and F_0=1.0V/Å was used. The charged pairs shown are (n_1,n_2)=(+1,+1), (+1,+2), (+2,+1) and (+2,+2).

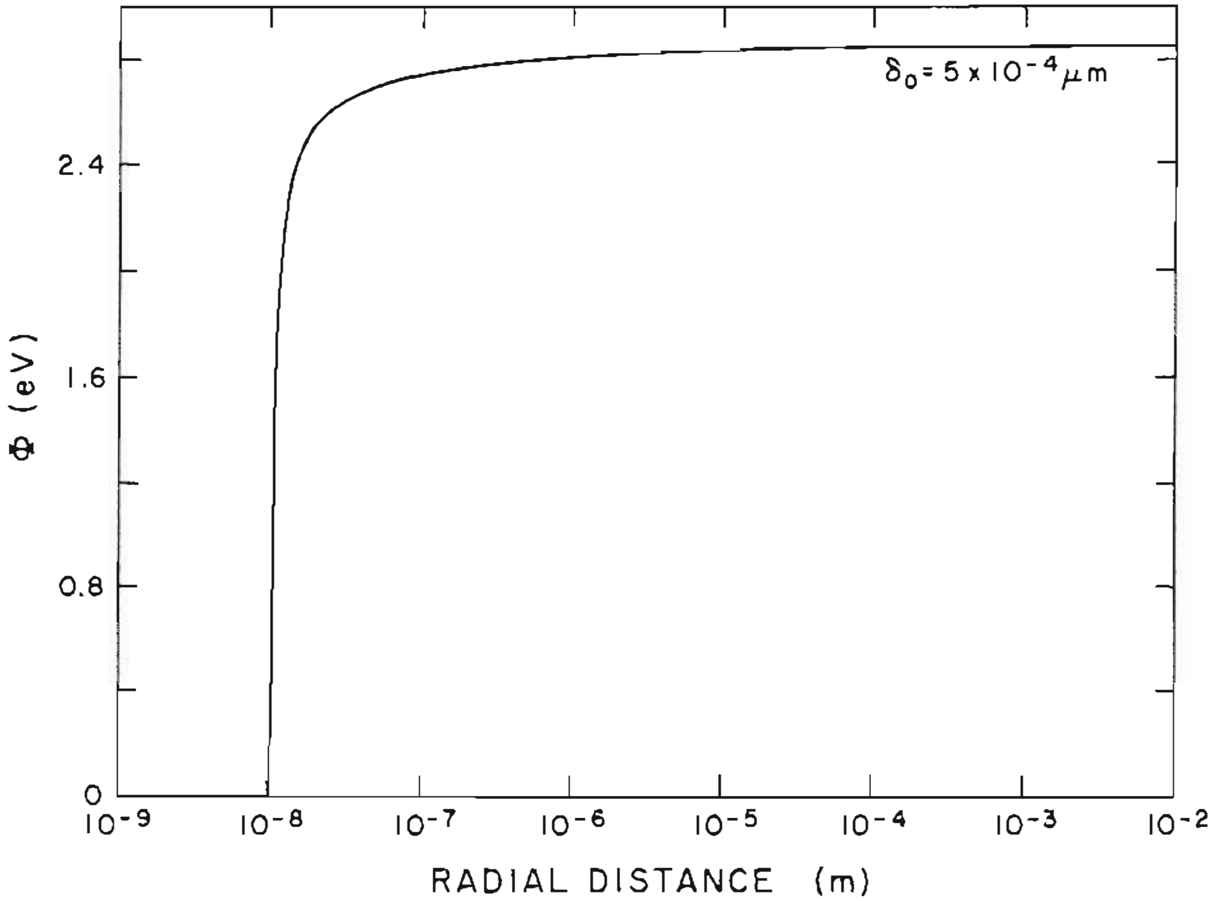

Figure 26. SOC Model Energy Shift vs. Distance. The energy shift, Φ, is shown as a function of distance with δ_0=5Å for gallium ions. The radius of the SOC emitter is 0.01μm and its other parameters are n=0.5, γ=3.0 and F_0=1.0V/Å.

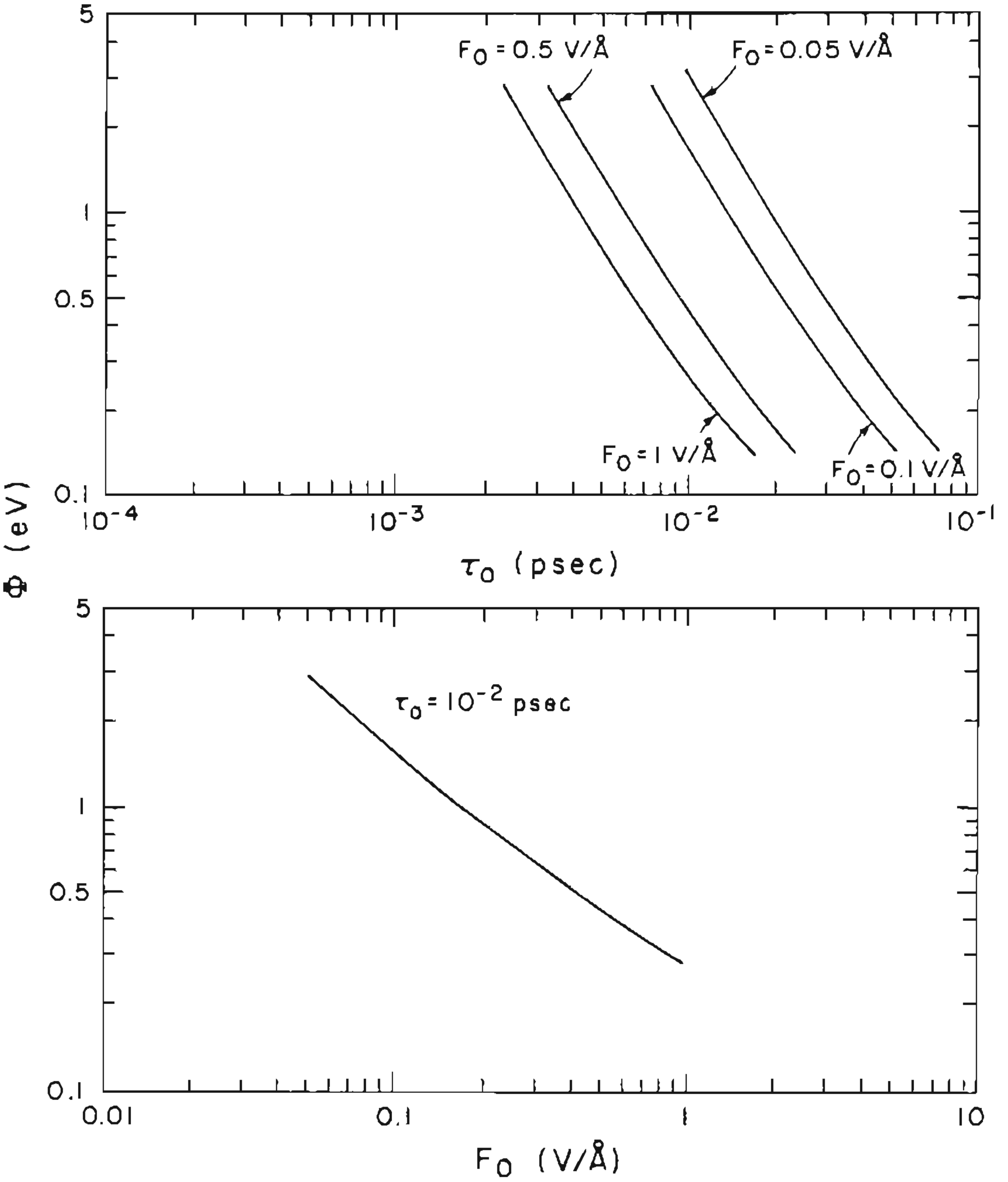

Figure 27. SOC Model Electon Energy Shift vs. Field Strength. The energy shift data for an SOC emitter of $n=0.15$, $\gamma=2.0$, $r_a=0.01\mu m$ and field strengths of $F_0=1.0$, 0.5, 0.1 and 0.05V/Å are shown.

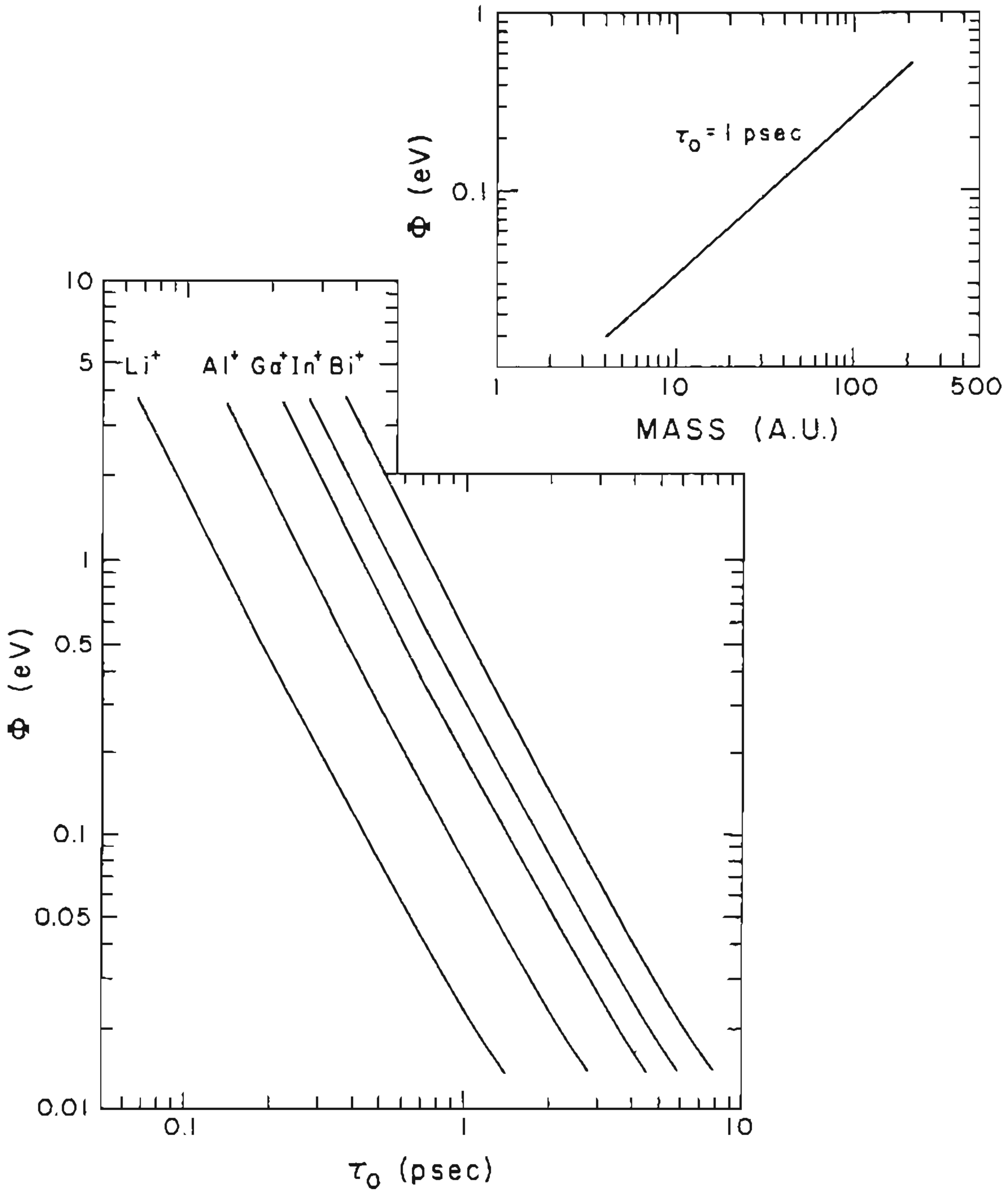

Figure 28. SOC Model Energy Shift vs. Ionic Mass. The energy shift data for the five ionic species Li^+, Al^+, Ga^+, In^+ and Bi^+ are shown. An SOC emitter of r_a=0.01μm, n=0.5, γ=3.0 and F_0=1.0V/Å was used.

function of mass for five different singly charged species. Figure 29 presents Φ corresponding to the charge species whose energy broadening data are shown on Figure 25. Figure 30 shows the same data as in Figure 29 except that the independent variable is δ_0 instead of τ_0.

This concludes the presentation of data for the SOC model colinear emission studies. The next section continues with trajectories having an initial angular separation emanating from an SOC model emitter.

5.4 SOC Model Studies II: Non-colinear Emission

The second enhancement to the model calculations was the inclusion of an initial angular separation, θ_0, between the particles in addition to the radial separation, δ_0. From the expression for the hypergeometric expansion for the Legendre function following Equation (43) in Section 3.3, for the case of colinear axial emission, where θ, $d\theta/dt$ and $d^2\theta/dt^2$ are all zero, the value of the Legendre function is equal to one. Thus the Equations (45c) and (45d) are not needed, the first terms drop out of Equations (45a) and (45b), and the hypergeometric expansions do not need to be evaluated. These simplifications were exploited for the colinear emission studies. When off-axial emission is permitted, however, Equations (45) cannot be simplified in these ways.

In all non-colinear cases studied, the launch angles for the two particles were equal in magnitude and of opposite sign. That is, the cone axis of symmetry bisects the angle between the two launch sites. Also,

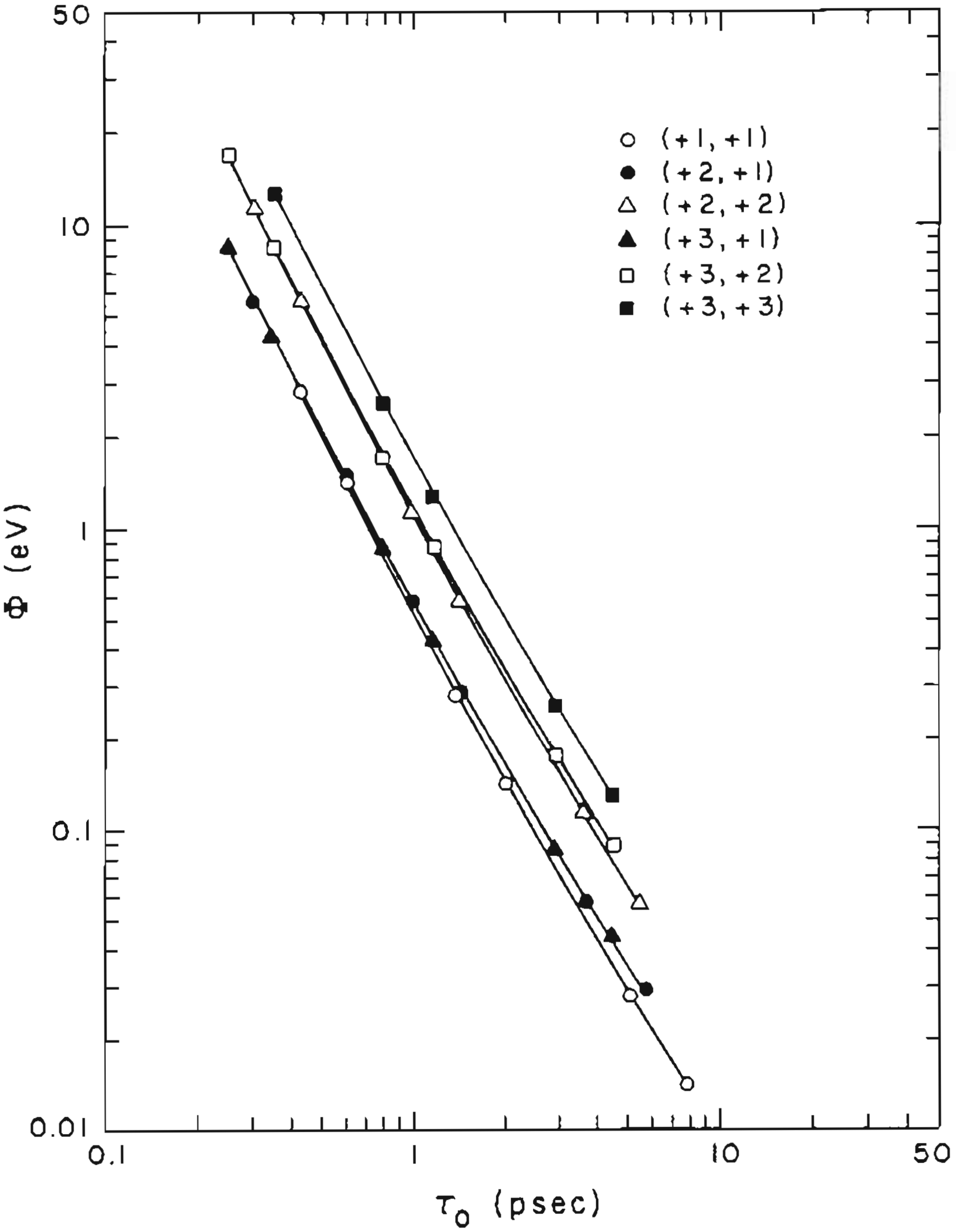

Figure 29. SOC Model Energy Shift vs. Charge. The energy shift data for six combinations of bismuth charge species are shown as a function of τ_0. An SOC emitter of r_a=0.01μm, n=0.5, γ=3.0 and F_0=1.0V/Å was used. The charged pairs shown are (n_1,n_2)=(+1,+1), (+2,+1), (+3,+1), (+2,+2), (+3,+2) and (+3,+3).

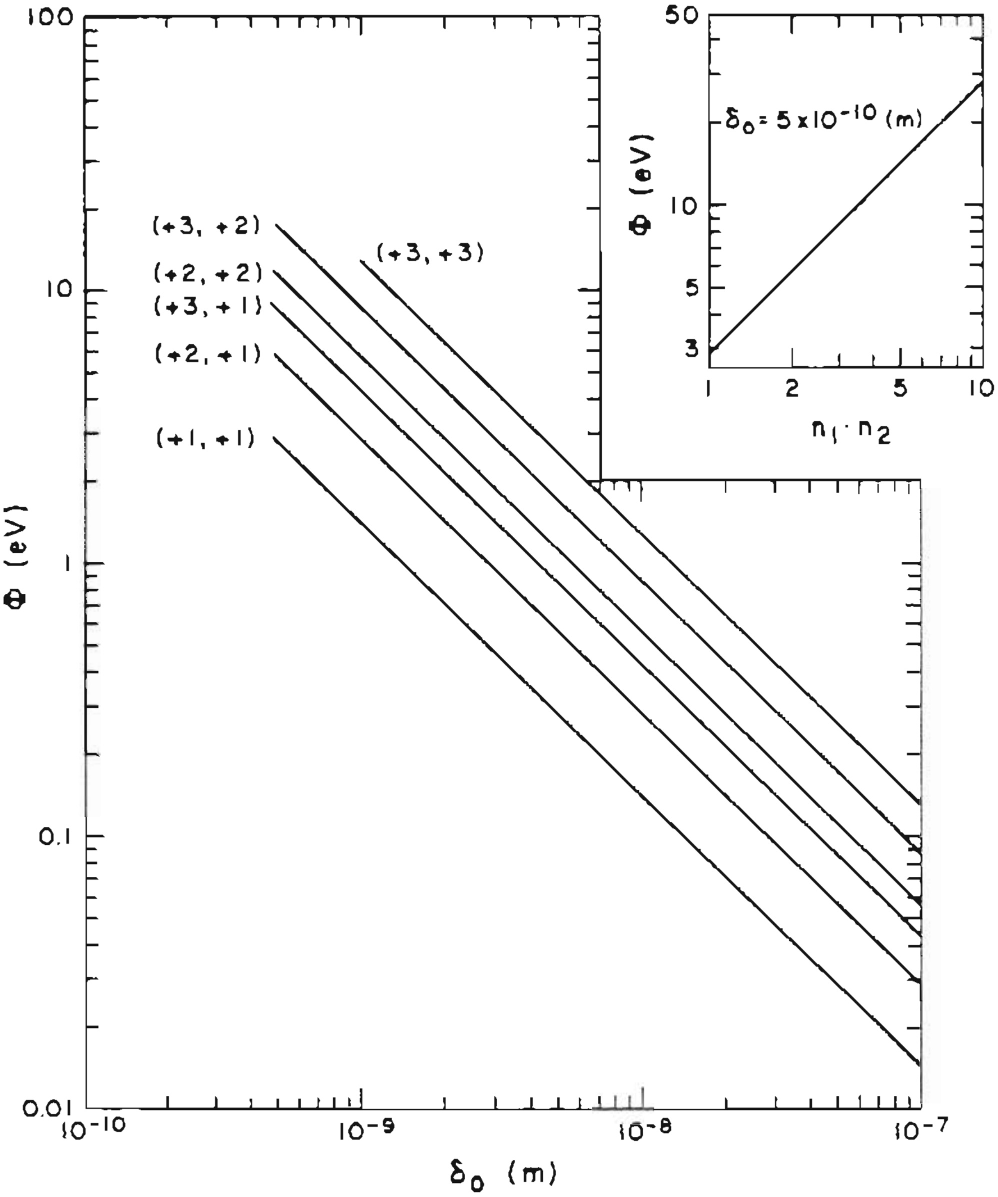

Figure 30. SOC Model Energy Shift vs. Charge. The energy shift data for six combinations of bismuth charge species are shown with δ_0 as the independent variable. An SOC emitter of r_a=0.01µm, n=0.5, γ=3.0 and F_0=1.0V/Å was used. The charged pairs shown are (n_1,n_2)=(+1,+1), (+2,+1), (+3,+1), (+2,+2), (+3,+2) and (+3,+3).

only Ga^+ ions were used in these studies. Furthermore, having already explored the effects of emitter radius and field strength on the energy broadening and energy shift, only one combination of radius and field strength was used: an emitter radius of 0.01 microns with a field strength of 1.0V/Å.

Since the data of this section are of such limited scope, this section will not be subdivided further, however, the order of presentation established in the preceding sections will be maintained. The energy broadening data will be shown first, followed by data on the average energy shift. Finally, the results of studies of the angular beam spreading will be presented.

Figure 31 presents energy broadening versus τ_0 data as a function of the emission half-angle, θ_0 and Figure 32 shows Φ also as a function of θ_0. The data in Figure 32 covers a somewhat broader range of θ_0 than does the data of Figure 31 in order to show how Φ falls off with distance.

For the next set of data showing angular beam spreading, a series of model calculations were conducted with the same set of initial conditions, but with the Coulomb interaction force set to zero.

The values of $\Delta\theta$ in Figure 33 are the amounts of angular dispersion without the pairwise interaction, $(\theta_2 - \theta_1)_{wo}$, subtracted from the angular dispersion with the pairwise interaction, $(\theta_2 - \theta_1)_c$, at a distance of $r_f = 1.0$ cm. That is, Figure 33 shows the amount of angular broadening arising solely from the Coulomb interaction.

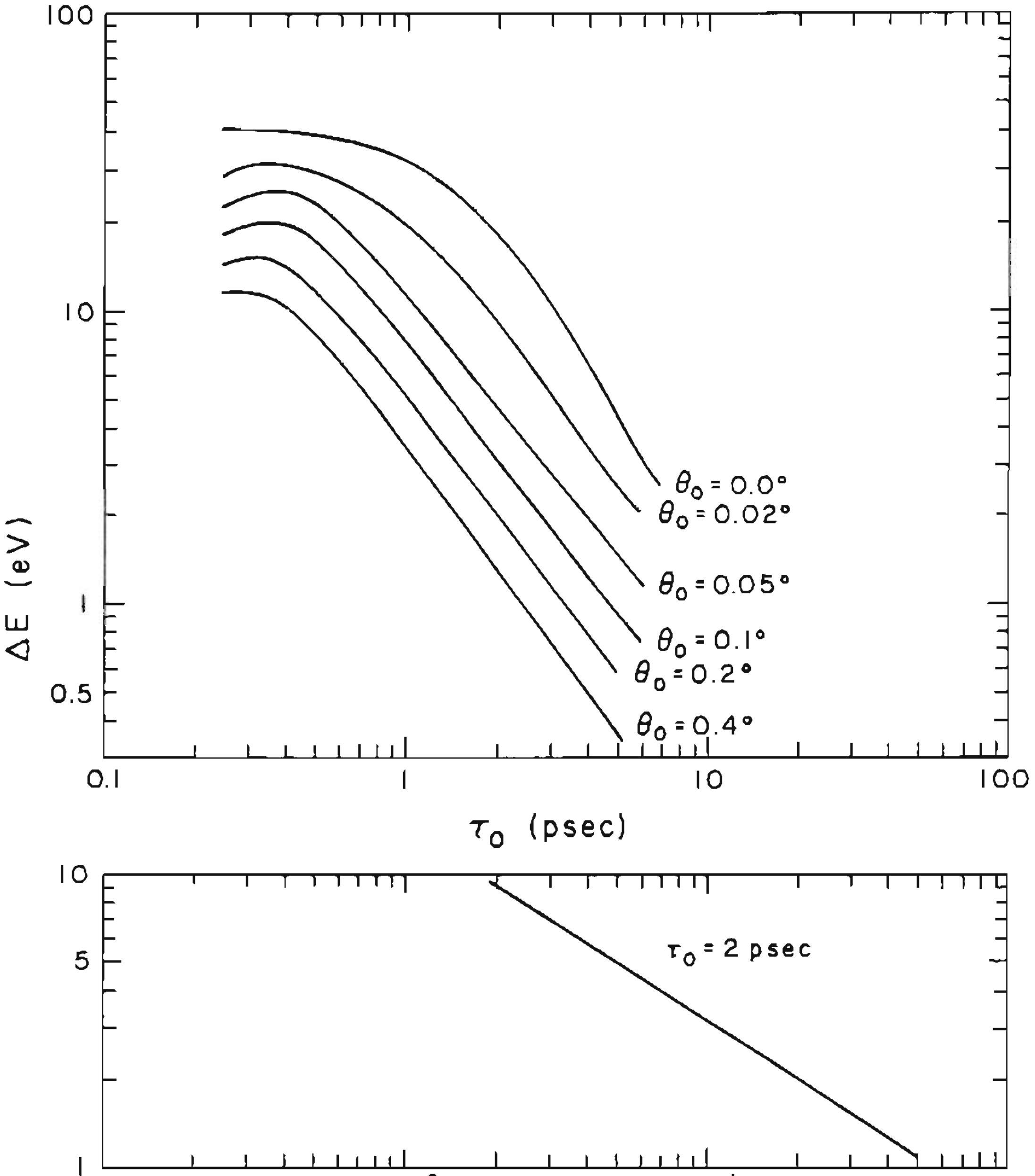

Figure 31. SOC Model Energy Spread vs. Emission Angle. The total energy spread data is shown for six values of emission half-angle, θ_0. Ga^+ ions were emitted from an SOC emitter of radius r_a=0.01μm, n=0.5, γ=3.0 and F_0=1.0V/Å. The values of θ_0 are 0°, 0.02°, 0.05°, 0.1°, 0.2° and 0.4°.

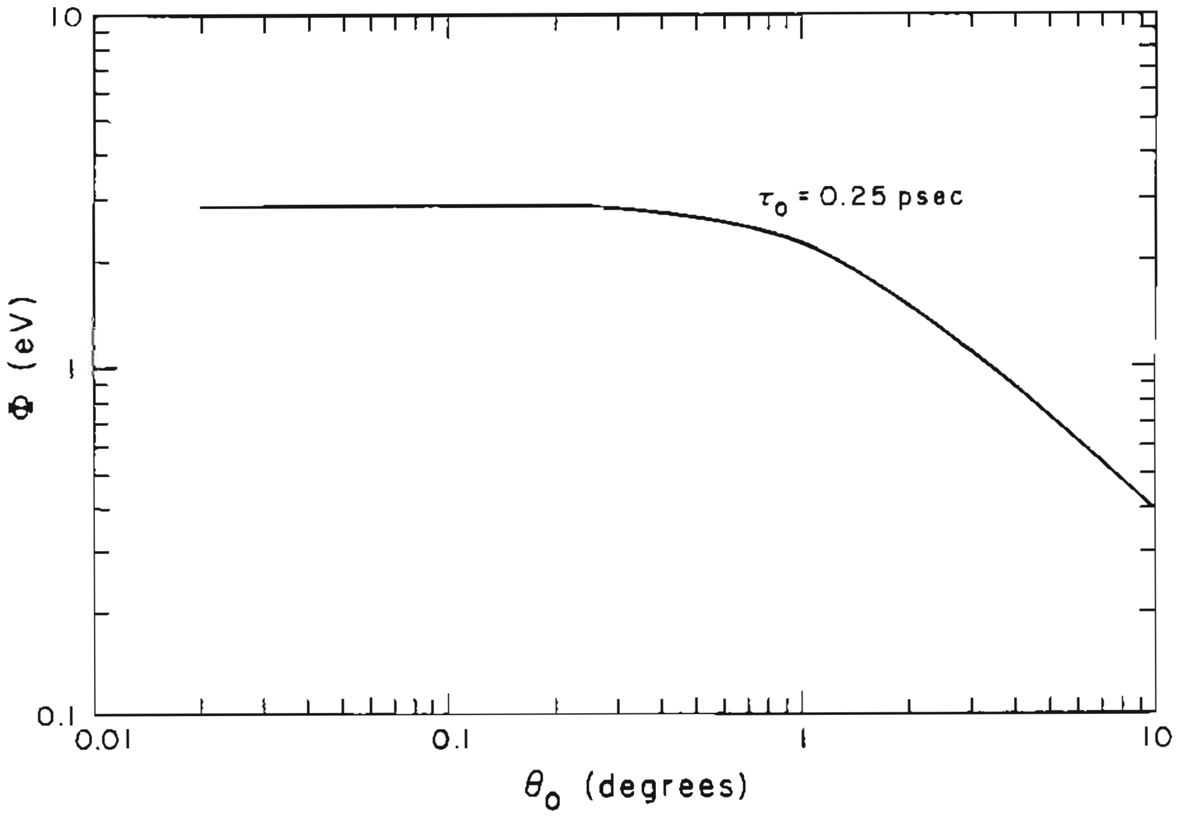

Figure 32. SOC Model Energy Shift vs. Emission Angle. The energy shift data is shown as a function of emission half-angle over the range θ_0=0.02° to 10.0° for τ_0=0.25psec. Ga$^+$ ions were used with emitter parameters of r_a=0.01μm, n=0.5, γ =3.0 and F_0=1.0V/Å.

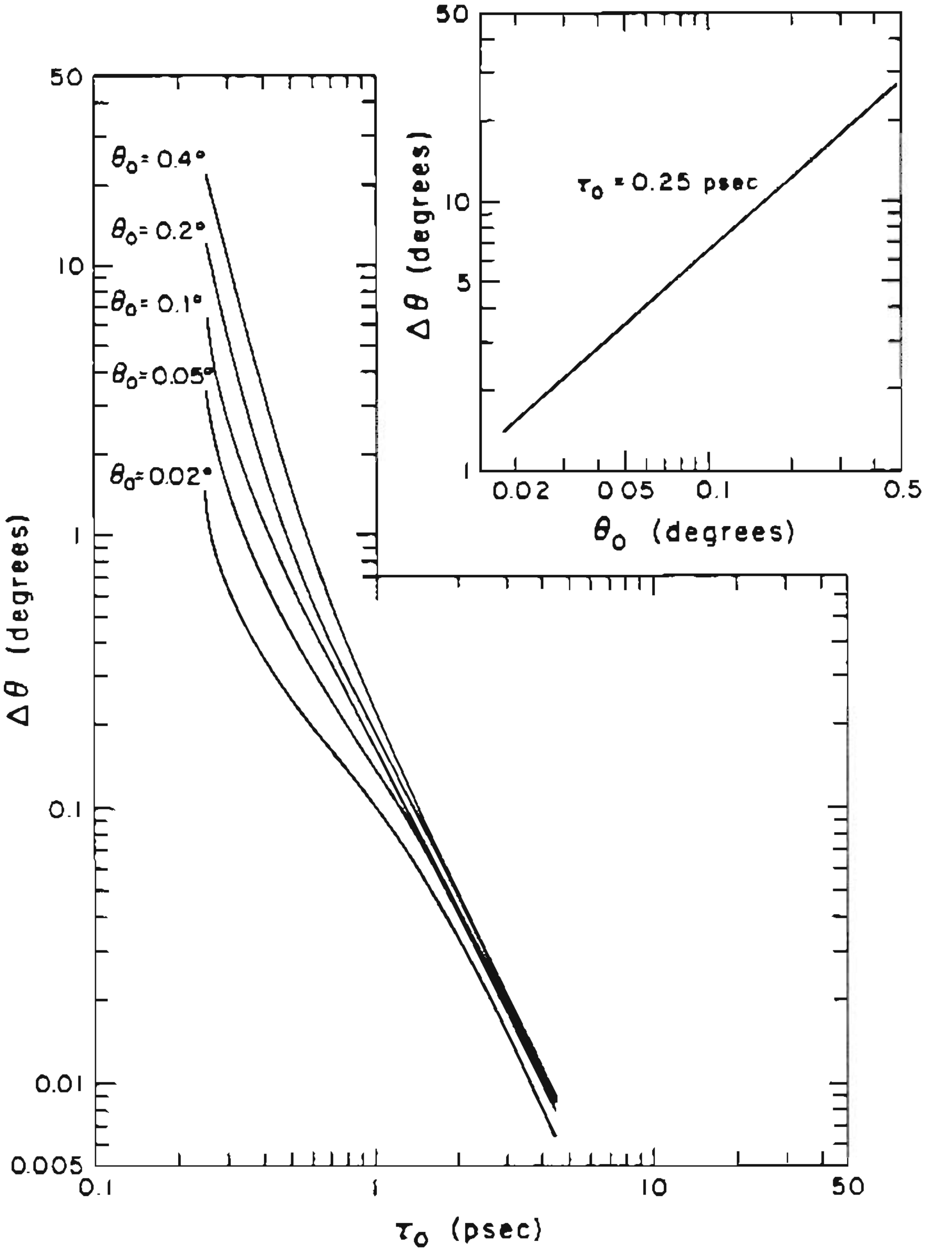

Figure 33. SOC Model Angular Spread vs. Emission Angle. The net angular spread arising from the coulomb interaction is shown for five values of emission half-angle, θ_0=0.02°, 0.05°, 0.1°, 0.2° and 0.4°. Ga^+ ions were used with emitter parameters of r_a=0.01μm, n=0.5, γ=3.0 and F_0=1.0V/Å.

This completes the presentation of the model calculations undertaken during the course of this study. A discussion of these data will be given in the next chapter. In the final section of the current chapter some experimental data for comparision with these theoretical studies will be presented.

CHAPTER SIX

Results and Discussion

6.1 Introduction

In Chapter 3 the emission process was discussed in terms of a Poisson distribution with respect to the time between emission events. The probability function for the interevent time, τ_0, according to the assumption of an exponential distribution is given by

$$P(\tau_0)=1-e^{-\lambda\tau_0} \tag{60}$$

From the data presented in Chapter 5 empirical relationships will be extracted for the total energy spread, ΔE, the energy shift, Φ and the angular beam spread, $\Delta\theta$, as functions of the interevent time τ_0, the emitter radius (or apex radius), r_a, the electric field strength, F_0, the atomic mass, m, and the charge, n. These empirical relationships will then be inserted into Equation (60) and the corresponding probability density functions will be derived. Then Equation (12) will be used to determine the model predictions for the average values of ΔE, Φ and $\Delta\theta$ as functions of experimentally measurable quantities such as current and atomic mass. These predictions will then be compared to experimental results.

6.2 Sphere Model Results

From Figures 6 and 9 the change in kinetic energy arising from the Coulomb interaction becomes essentially independent of distance for both electrons and ions for distances greater than about 0.1mm from the emitting sphere. The particles are interacting only very weakly in this region of the beam, indicating that the inter-particle separation, δ, has become large. Figure 14 shows that the process causing the average energy shift phenomenon occurs even closer to the emitting sphere. About 90% of the final magnitude is attained within a few hundred Angstroms from the emitting sphere.

6.2.1 Energy Broadening Results

The curves in the upper plots of Figures 7 and 8 represent data taken directly from model simulations. The curves in the lower plots are data extracted from the upper curves at the selected times shown. From measurements of the slopes of these curves, the dependence of the energy broadening on the interevent time, the emitter radius and the field strength for electrons is found to be exactly

$$\Delta E \propto \tau_0^{-1/2} (r_a F_0)^{1/4}$$

The same functional relationships may similarly be obtained from the data for gallium ions shown in Figures 10 and 11.

The dependence of the energy spread on ionic mass measured from the slope of the line in the bottom graph of Figure 12 is

$$\Delta E \propto m^{1/4}$$

The data of Figure 13 indicate a fairly complex relationship between the energy spread and the charges on the pair of interacting ions. In comparing the case where both ions have a single charge to the case of one of the ions carrying a double charge, the model predicts that the energy spread is very sensitive to the order of emission. This is primarily a result of the difference in acceleration between the particles in the electric field of the diode. If the second particles carries the double charge, then it will be driven toward the first particle, opposing their mutual repulsion and causing the Coulomb interaction to persist over a greater portion of the beam length. This will result in a corresponding increase in the energy broadening. However, if the first particle carries the double charge, then the converse will be observed. The particles will spend less time in close proximity and the strength of the Coulomb repulsion will be weaker. This is shown dramatically in Figure 13.

If only the two cases where both ions carry the same charge are considered, then the measured dependence of the energy spread on charge seen in Figure 13 is

$$\Delta E \propto n^{5/4}$$

Except for the tin LMIS[4], the relative abundance of multiply charged species is usually quite low, and the probability of an interaction event between two multiply charged particles is very small. A Monte-Carlo study involving a distribution of charge species would better be able to characterize the charge dependence of the energy spread than the present two-particle simulations, however, the effects of spacing and geometry can be clearly seen with the present model.

Combining the results of the preceding paragraphs gives the following empirical relationships:

$$\Delta E \propto \tau_0^{-1/2} (r_a F_0 m)^{1/4} n^{5/4}$$

Solving for τ_0 yields

$$\begin{aligned} \tau_0 &= c_1 (r_a F_0 m)^{1/2} n^{5/2} \Delta E^{-2} \\ &= K_E \Delta E^{-2} \end{aligned} \tag{61}$$

By substituting this expression for τ_0 into Equation (60) and taking the derivative with respect to ΔE, the following expression for the probability density function in terms of the total energy spread is obtained:

$$f(\Delta E) = 2K_E \lambda \Delta E^{-3} \exp(-K_E \lambda \Delta E^{-2}) \tag{62}$$

The mean value of ΔE for this distribution is then given by

$$<\Delta E> = \int_0^\infty \Delta E \, f(\Delta E) \, d(\Delta E) \tag{63}$$

If the integration is carried out the following relationship for <ΔE> is obtained:

$$\begin{aligned} <\Delta E> &= (\lambda K_E \pi)^{1/2} \\ &= c(r_a F_0 m)^{1/4} n^{3/4} I^{1/2} \end{aligned} \tag{64}$$

where $c = (\pi c_1/e)^{1/2}$. By expressing the field strength at the emitter surface, F_0, in terms of a voltage V_0, Equation (64) may be written as

$$<\Delta E> = c(V_0 m)^{1/4} \, n^{3/4} \, I^{1/2} \qquad (65)$$

Thus the sphere model predicts a simple relationship between $<\Delta E>$ and the given measurable experimental parameters for electron beams and for LMIS.

6.2.2 Energy Shift Results

As pointed out in Section 5.2.2 the energy shift was found to be independent of emitter radius over the range 0.01 to 1.0μm. Again, by measuring the slopes of the lines shown in Figures 15 through 17, the following empirical relationship is obtained:

$$\Phi \propto \tau_0^{-2} \, F_0^{-3/4} \, mn$$

By solving for τ_0 the following relationship is obtained:

$$\begin{aligned} \tau_0 &= c_2(mn/F_0^{3/4} \, \Phi)^{1/2} \\ &= K_\Phi \, \Phi^{-1/2} \qquad (66) \end{aligned}$$

By substituting this expression into Equation (60) and taking the derivative with respect to Φ, the following expression for the probability density function in terms of Φ is obtained:

$$f(\Phi) = (K_\Phi \, \lambda \, \Phi^{-3/2} /2) \exp[-K_\Phi \, \lambda \, \Phi^{-1/2}] \qquad (67)$$

The average value of Φ is obtained from the integral

$$<\Phi> = \int_0^\infty \Phi \, f(\Phi) \, d(\Phi) \qquad (68)$$

As pointed out by Gesley et al.[49], the integral of Equation (68) is divergent and it is necessary to place an upper bound on Φ which is equivalent to limiting the current. In the limit of $I \rightarrow 0$ they obtain

$$\lim_{I \rightarrow 0} \langle \Phi \rangle = c_2 (nm/4\pi\epsilon_0 \, \delta_C)^{1/2} \, I \tag{69}$$

where a limiting value equal to the initial Coulomb potential energy

$$\Phi_C = (ne)^2 / 4\pi\epsilon_0 \, \delta_C \tag{70}$$

was used, with δ_C equal to some minimum allowable initial separation. In this development, an additional factor of $F_0^{-3/8}$ is obtained as a result of the inclusion of a more complete set of model data, so that

$$\lim_{I \rightarrow 0} \langle \Phi \rangle = c_2 (nm/F_0^{3/4} \, 4\pi\epsilon_0 \, \delta_C)^{1/2} \, I \tag{71}$$

6.2.3 Comparisons with Experimental Data

Figure 34, reproduced from Bell and Swanson[6] shows experimentally measured data for the dependence of electron energy spread as a function of a field factor β which is inversely proportional to the emitter radius. Measurements of the slopes of the lines of these data plotted on logarithmic axes show that $\Delta E \propto r_a^{-2/3}$, which does not agree well with the sphere model result of $\Delta E \propto r_a^{1/4}$. In the next section it will be found that when the emitter shank is included with the SOC model, an inverse relationship is predicted for high currents, although for low currents the SOC model agrees with the sphere model in predicting a

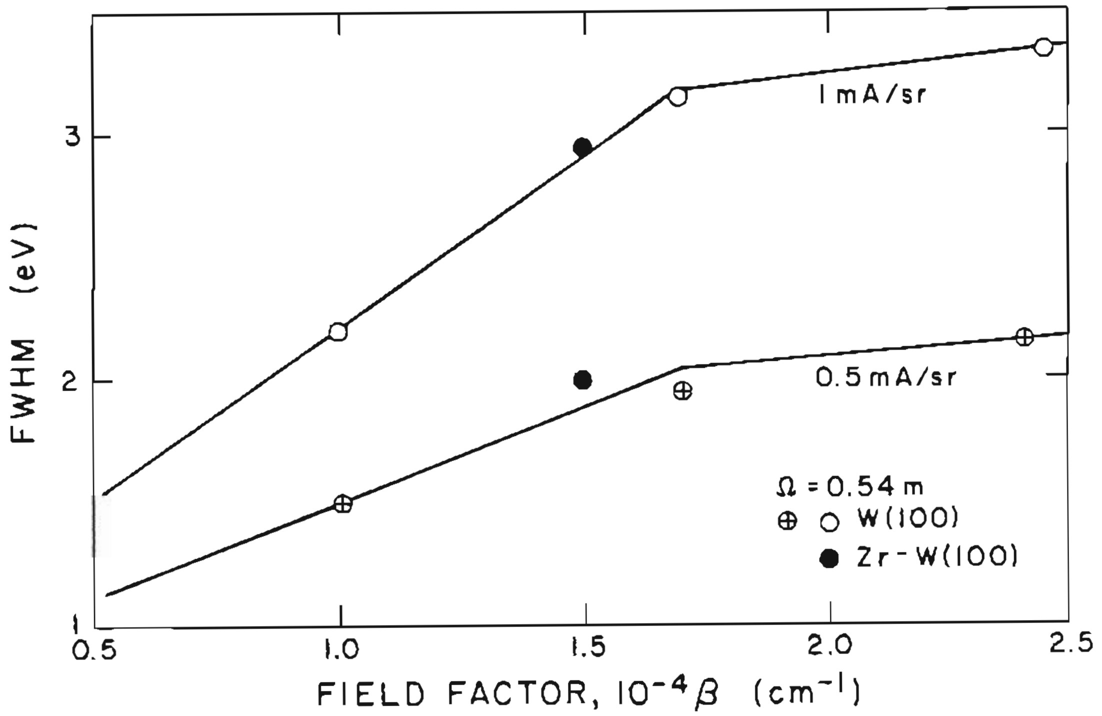

Figure 34. Experimental Energy Spread vs. Field Factor. The data in this figure are taken from Reference 6, and show the dependence of the FWHM of the energy distribution on the field factor β which is proportional to $1/r_a$.

direct dependence.

Turning to the field dependence, Figure 35, also reproduced from Bell and Swanson[6] shows experimental electron energy spread data as a function of emitter field strength. However, these data are not at constant current as are the data presented in Figures 8 and 11 for the sphere model, and it is therefore difficult to make a correlation. From Löffler's theoretical analysis[27] of the sphere model an $F_0^{-1/4}$ dependence would be expected, whereas the sphere model calculations exhibit an $F_0^{1/4}$ relationship. As in the case with the tip radius dependence, the SOC model calculations exhibit either a direct or inverse relationship, depending on the emitter shape and the total current.

Figures 36 through 38 are reproduced from Gesley, Larson and Swanson [49]. Figure 36 shows plots of experimental total energy broadening for several singly charged ionic species from LMIS, and Figure 37 shows similar plots for doubly charged ionic species. Their comparison of model predictions to experimental data with respect to mass, charge and current takes into account the intrinsic energy spread $<\Delta E>_{int}$ associated with the ion formation process. Using a value of $<\Delta E>_{int} = 5$ eV for all species except Ga^{++} where a value of 1 eV was used they obtained the results reproduced in Figure 38. The sphere model was found to agree with experiment in predicting $\Delta E \propto I^{1/2} m^{1/4}$ and disagree with respect to the charge dependence. The model predicts $\Delta E \propto n^{3/4}$ whereas the observed dependence is $n^{-1/2}$. A glance at Figure 13 shows that the disagreement with respect to the charge dependence

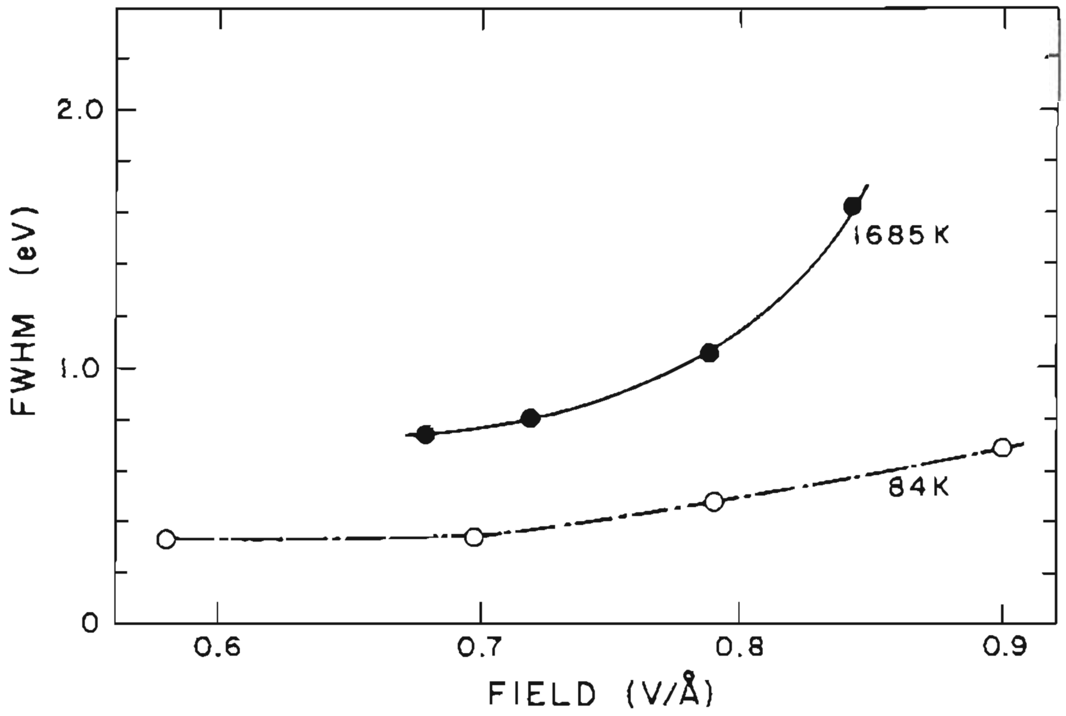

Figure 35. Experimental Energy Spread vs. Field Strength. The data in this figure are taken from Reference 6, and show the variation of the FWHM of the energy distribution with the emitter field strength, F_0.

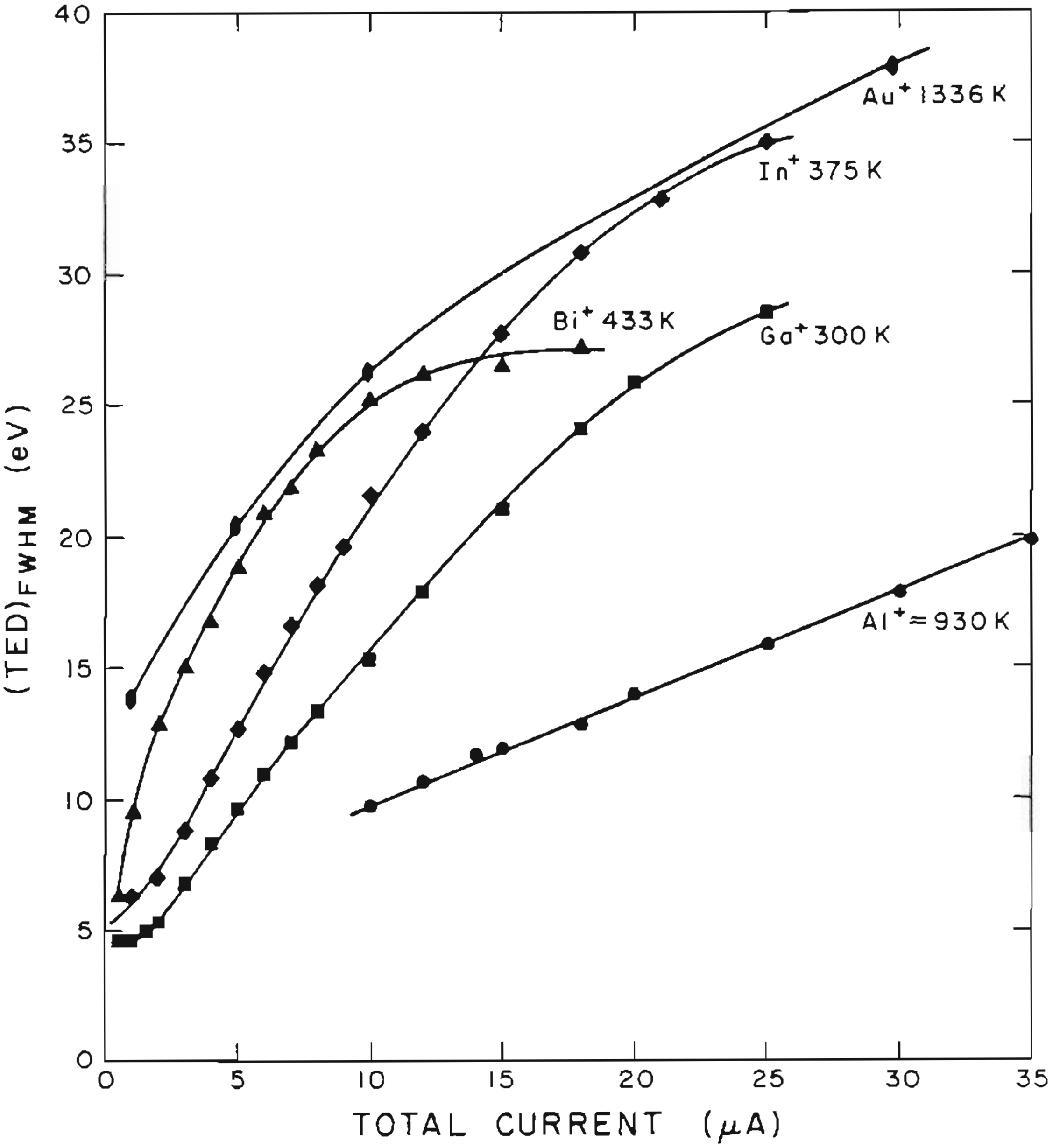

Figure 36. Experimental Energy Spread vs. Mass. Experimental data for Al$^+$, Ga$^+$, In$^+$ and Bi$^+$ are shown as a function of total current for LMIS emission. This figure was reproduced from Reference 49.

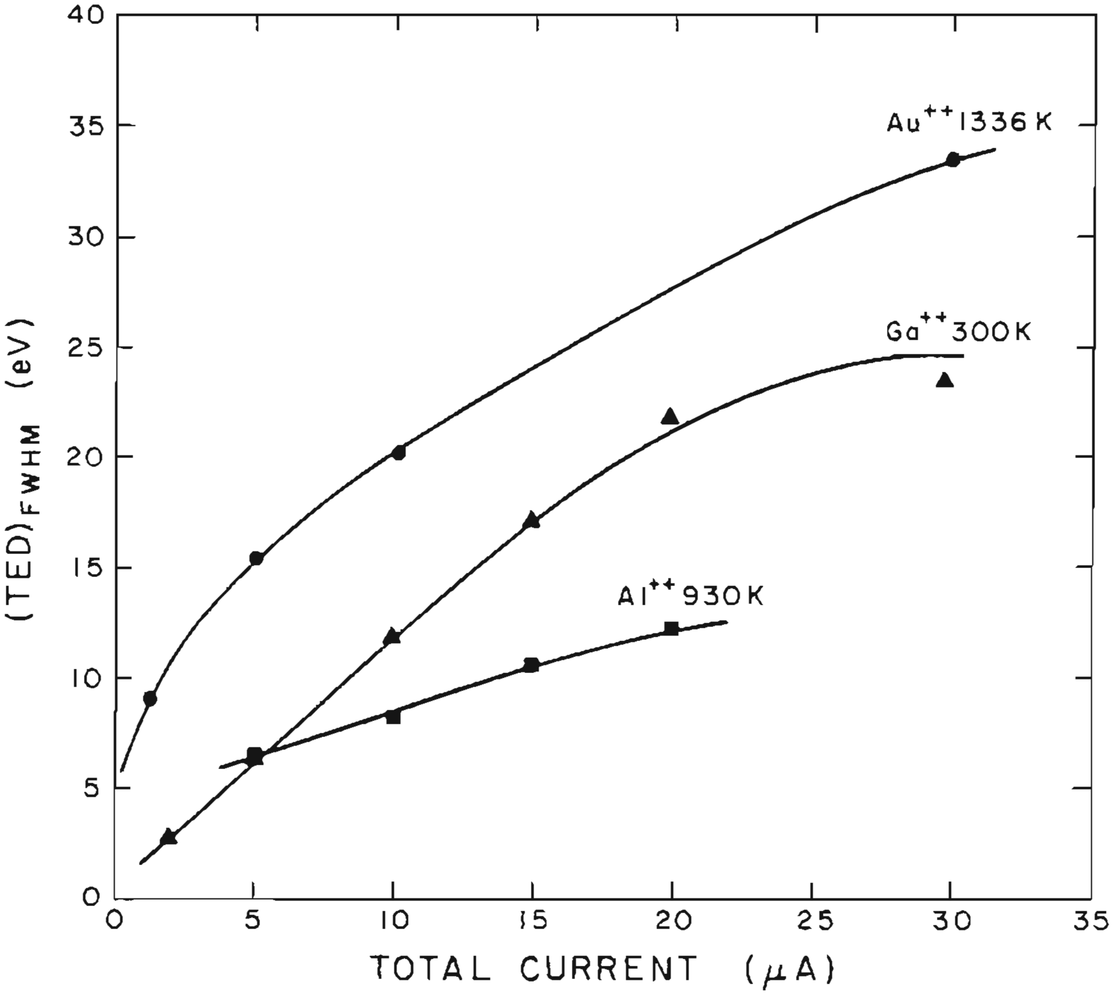

Figure 37. Experimental Energy Spread vs. Mass. Experimental data for Al^{++} and Ga^{++} are shown as a function of total current for LMIS emission. This figure was reproduced from Reference 49.

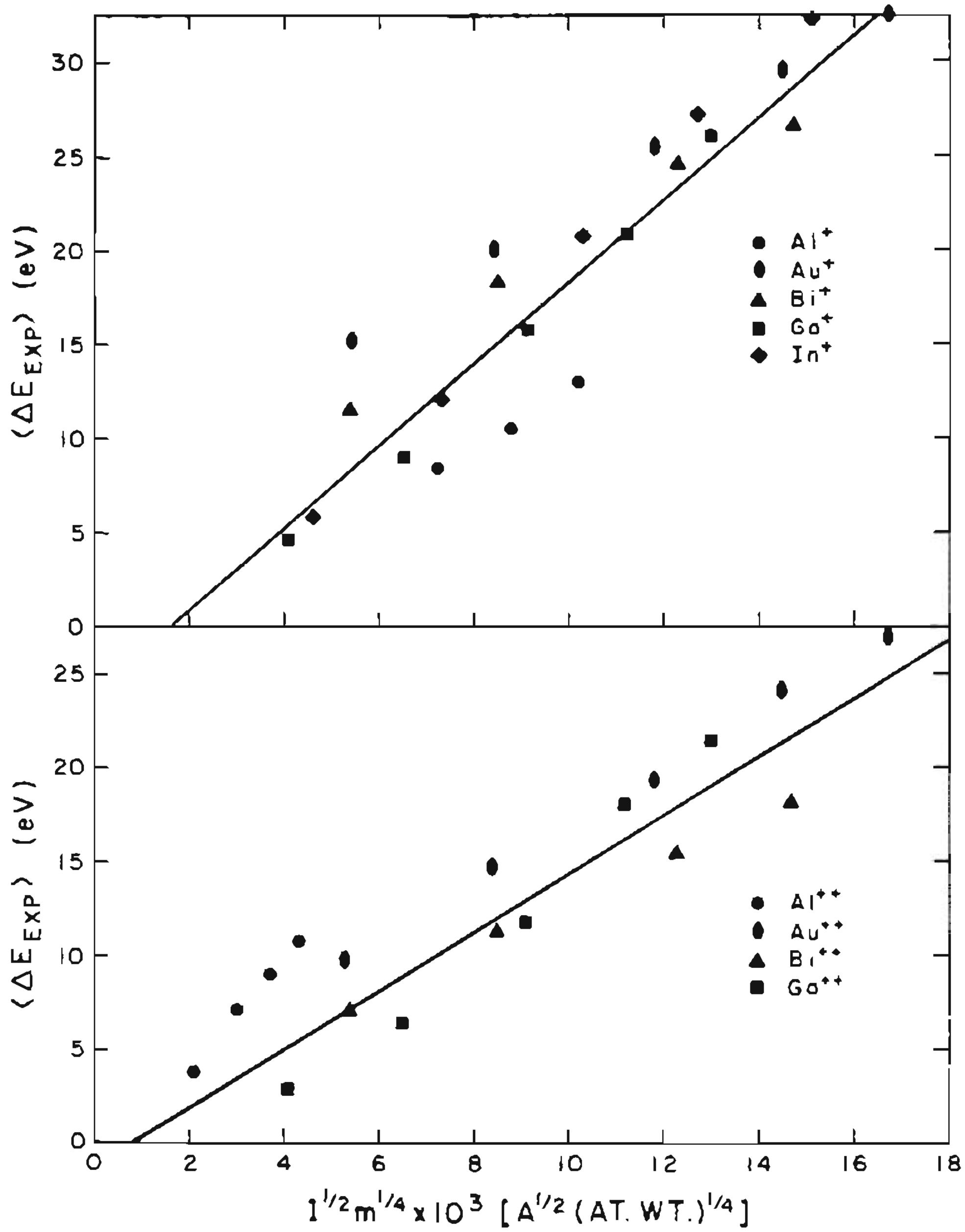

Figure 38. Corrected Experimental vs. Sphere Model Predicted Energy Spread. Plots of experimental values of the corrected energy spread versus the sphere model predictions based on Equation (65). This figure was reproduced from Reference 49.

is to be expected in view of the complexities involved with the mixed charge data, and that only pairs of equally charged particles were used in arriving at these model predictions.

In summary, a spherical model for the emitter shape together with the limitations of single file emission and pairwise interactions gives good qualitative agreement with experiment for the current and mass dependence of the energy spread in electron and ion beams.

A discussion of the comparison between the model predictions for the average energy shift and the experimental results will be deferred until the end of Section 6.3.

6.3 SOC Model Results

The investigation of the sphere on orthogonal cone electric field model, revealed some interesting differences from the sphere model results. In the electron studies values of $n = 0.15$ and $\gamma = 2.0$ were selected. Figure 18 shows the development of the contribution to the energy spread from the first particle. Comparing this with the corresponding sphere model data of Figure 6 shows two things. Firstly, although the interaction has again become negligible by the time the particles have reached the collector, the region of significant interaction has extended further away from the emitter surface. Secondly, the values of ΔE attained with the SOC model are generally higher than those attained with the sphere model. This, of course, is because the particles are interacting throughout a larger region in space.

In the ion studies values for n and γ of 0.5 and 3.0, respectively, were chosen and here the effect just beginning to appear in the electron case is even more pronounced. In Figure 21, which shows data for gallium ions, the Coulomb interaction is not over even at a typical practical working distance of 1.0 cm, particularly for larger values of δ_0 which correspond to low current values according to Equation (16). The effect appears to be more a matter of emitter shape than of particle mass. More particularly, the model studies suggest that not only the magnitude of the electric field but also the shape of the electric field in the region close to the emitter strongly influences the degree to which the Coulomb interaction broadens the energy distribution in the beam.

A comparison of Figure 21 to the sphere model gallium ion data of Figure 9 shows that, as in the electron studies, the total energy spread attains much higher values with the SOC model than with the sphere model because the ions in the SOC model interact over a much larger distance.

The simple models used in this study do not include the capability of inserting lenses or apertures in the tip region. Such electric field altering devices are used, however, in many practical applications, and the model data suggest that these will influence the magnitude of the energy spread in a beam of electrons or ions.

6.3.1 Energy Broadening Results

From measurements of the slopes of Figure 19 the dependence of the electron energy broadening on both the interevent time and the emitter radius vary slightly about the values found from the sphere model data of Figure 7. The dependencies are again given approximately by $\Delta E \propto \tau_0^{1/2} r_a^{1/4}$. The dependence on field strength as measured from the slope of the line on the bottom half of Figure 20, however, has grown from $F_0^{1/4}$ for the sphere data of Figure 8 to $F_0^{1/3}$ for the SOC data.

An examination of the SOC model data for gallium ions, shows that the situation is quite different from the sphere model results. It is no longer possible to find a simple power law relationship between the total energy spread and either the emitter apex radius or the field strength. Figures 22 and 23 show that ΔE increases with r_a and F_0 for higher current (lower τ_0), but decreases with r_a and F_0 for lower currents. If it is assumed that the total energy spread for a given set of initial conditions will asymptotically approach a limiting value, the behavior in Figures 22 and 24 results from placing the collector in a position that yields different percentages of the limiting value for different values of τ_0. This is clearly the import of Figure 21. A similar effect could have been observed with the sphere model data had the collector been positioned at 0.5μm from the emitter rather than 1.0cm. This serves to point out the limitations of modeling a real electron or ion optical problem with a simple sphere model, and the care that must be taken in selecting a more appropriate electric field model.

Figures 24 and 25 show the mass and charge dependence of the energy spread. Like the dependence on r_a and F_0, the mass dependence is influenced by the emitter geometry, although to a lesser extent. The mass dependence ranges from almost no dependence for high currents to $\Delta E \propto m^{1/2}$ for lower currents. The dependence on charge for the cases of both ions having the same charge is the same for the SOC model as for the sphere model, namely $\Delta E \propto n^{5/4}$.

In summary, then, the emitter geometry appears to play a significant role in determining the behavior of the energy broadening on other parameters. For the assumed electron emitter shape with no nearby electron optical elements, the energy broadening is comparable to the sphere model results. But for the assumed LMIS shape, the mass, field strength and emitter radius dependencies are complicated functions of the emitter-collector spacing and of the beam current. This may help to explain some of the differences in experimental dependencies reported in the literature.

The magnitude of the predicted energy spread is higher for both SOC models than for the sphere model emitter.

6.3.2 Energy Shift Results

Figure 26 shows the energy shift as a function of distance from the emitter for gallium ions. The shape of the curve for electrons, as mentioned in Section 5.3.2 is essentially the same. Note that the energy shift remains constant for both electrons and ions for distances greater than about 0.1mm just as it did in the sphere model studies. This is in contrast to the SOC model results discussed in the preceding section.

Comparing Figures 27-29 with the corresponding sphere model data of Figures 15-17 reveals that the same empirical relationships hold for both sets of data, namely

$$\Phi \propto \tau_0^{-2} F_0^{-3/4} mn.$$

In other words, the energy shift is independent of emitter shape as well as emitter size.

In the data presented thus far τ_0 has been used as the independent variable in accordance with the program set forth in Chapter 3 and in the introduction to this chapter. However, in view ot the independence of the energy shift on the emitter parameters, and the inverse square law dependence on τ_0, intuition suggested plotting energy shift data as a function of the initial interparticle spacing δ_0. The results are shown in Figure 30, for the same six combinations of charge plotted in Figure 29. By plotting the data in this way it becomes immediately obvious that

$$\Phi \propto n_1 n_2/\delta \tag{72}$$

and that the proportionality constant is, in fact $e^2/4\pi\epsilon_0$ which is to say that the observed energy shift is identically equal to the initial Coulomb potential energy of the two particle system at the instant of the creation of the second particle. Experimentally measured values of Φ

thus provide a means of determining δ_0, the initial spacing between the particles dominating the Coulomb interactions within the beam.

The mass dependence of Φ arises from the fact that the conversion of the electical potential energy into kinetic energy imparts a velocity which is inversely proportional to the mass of the particles. As an illustration of this, the model predicts that the first bismuth ion requires approximately 1.4 psec to reach a distance of 50Å accelerating from rest in the field of the emitter. In the same amount of time in the same field, a lithium ion would have travelled 1000Å. The Coulomb potential energy between the bismuth ions would be 20 times greater than the energy between the lithium ions which are further apart, even though the total current, which is inversely proportional to time, would be about the same. Thus it would be expected that a beam of bismuth ions would have an energy shift twenty times greater than a beam of lithium ions at the same current. By the same reasoning, the model predicts that bismuth would show an energy shift five times larger than gallium and twice as large as indium.

6.3.3 Comparisons with Experimental Data

With respect to the energy broadening data of Figures 34 and 36, one of the main differences between the SOC model and the sphere model is that the magnitude of energy broadening with the SOC model is comparable to the experimentally measured values. Knauer[48] defines the single file regime as those currents that correspond to an average initial interparticle spacing $<\delta_0>$ greater than the beam radius. The spacings used in the single file emission model studies were in the range 0.5nm to 100nm. According to the assumed LMIS conditions[49], $<\delta_0>$ must be greater than 0.8nm to satisfy Knauer's criterion. Only the very smallest initial spacing used in these studies was less than 0.8nm, and since the spacings used represent unusually close pairs that are fluctuations from the average, it is clear that these results support Knauer's conclusion that field emission sources belong in the single file regime shown in Figure 39 reproduced from his paper.

The other main result is that the functional relationships predicted by the SOC model are largely the same as for the sphere model for the emitter shape used with the electron studies, but become more complicated with larger cone angles, allowing for the possibility of bringing the dependencies on emitter radius and field strength, as well as the current and mass relationships, into agreement with experiment.

In the concluding remarks of Section 6.3.2 several predictions were made with respect to the relative values of energy shift in LMIS beams of different mass. These predictions depend on the conclusion that the apparent mass dependence of Φ is caused by the implicit mass dependence of δ_C, the minimum allowable initial interparticle separation discussed in connection with Equation (69). Examination of Figure 40 shows that these predictions are indeed correct. It is concluded, therefore, that the shift in average peak energy observed in LMIS

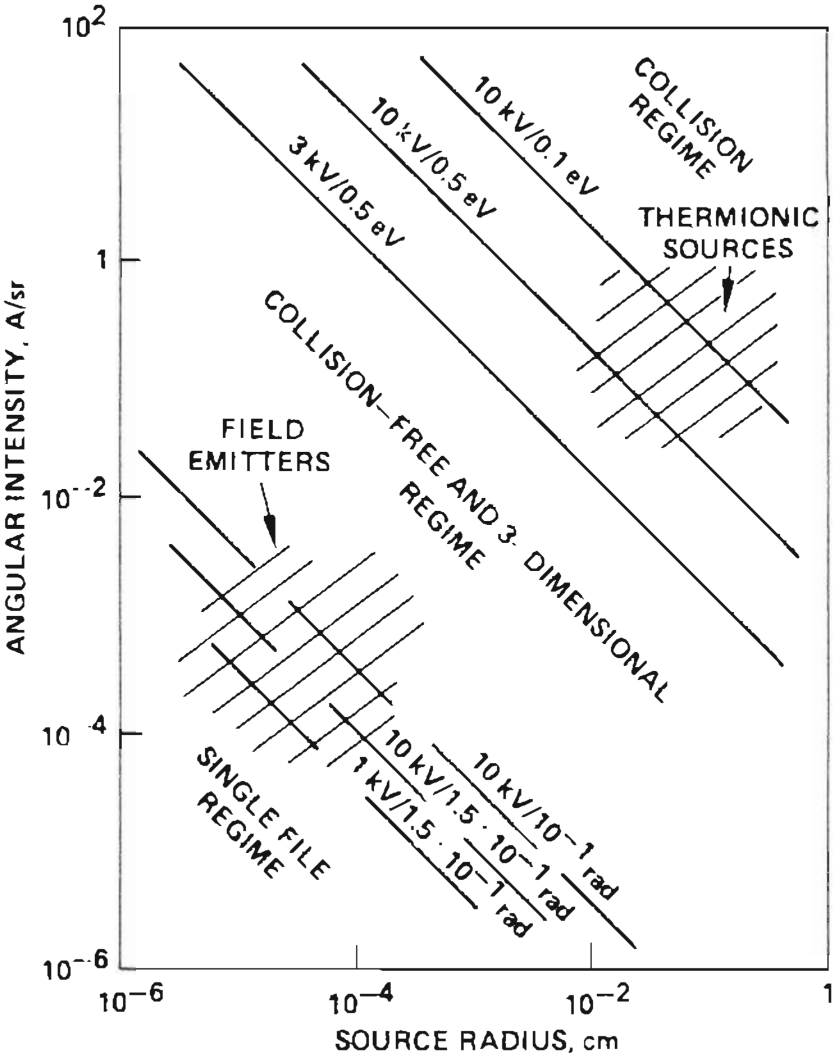

Figure 39. Electron Collision Regimes. This figure is taken from Reference 48 and shows various emission processes and the degree to which generated particles interact with one another. Electron field emission sources are found in the "single file" regime.

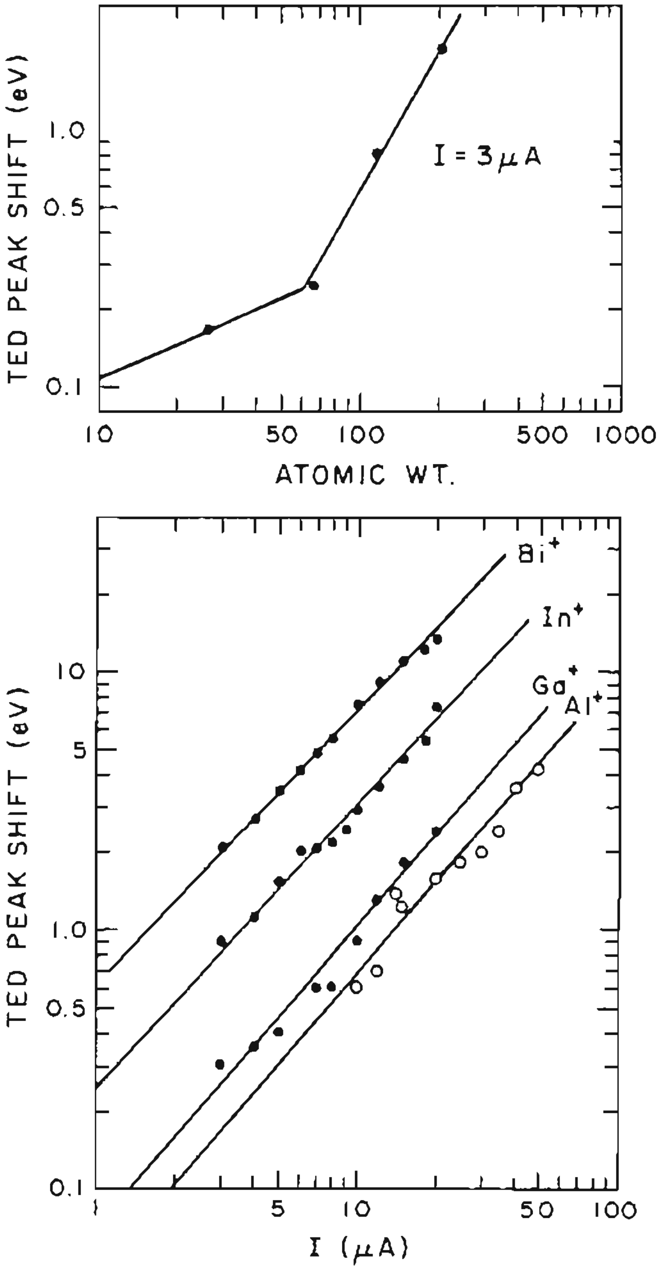

Figure 40. Experimental Energy Shift vs. Mass. Experimental shifts in the TED peak position is shown as a function of mass for the ionic species Al$^+$, Ga$^+$, In$^+$ and Bi$^+$. The results for Ga$^+$, In$^+$ and Bi$^+$were taken from Reference 49.

emission is entirely the result of the relaxation of the initial Coulomb potential energy between pairs of ions into kinetic energy.

6.4 SOC Model Non-colinear Results

Figures 31 and 32 show that the total energy spread and energy shift can attain significant values even when the condition of colinear emission is relaxed, allowing an angular separation between the interacting pair. The energy broadening falls off approximately as $\theta_0^{-1/2}$, while the energy shift, arising as it does from the initial Coulomb potential energy, depends on θ_0 according to

$$\Phi \propto (r_1^2 + r_2^2 - 2r_1r_2 \cos \theta_{12})^{-1/2} \tag{73}$$

where r_1 and r_2 are the radial coordinates of the two particles and θ_{12} is the angle $\theta_1 - \theta_2 = 2\theta_0$ in these studies.

From Figure 33 the amount of angular beam broadening caused by the Coulomb interaction varies as τ_0^{-2} for most of the data covered. The dependence of $\Delta\theta$ on initial angular separation is less straight forward. At low values of τ_0, $\Delta\theta \propto \theta_0$, but at high values $\Delta\theta$ is almost independent of θ_0. For the high current value case (low τ_0)

$$\Delta\theta \propto \tau_0^{-2}\,\theta_0 \tag{74}$$

In order to relate the angular broadening to beam current, it would be necessary to develop a multi-dimensional probability density function based on the assumptions that the emission process follows a Poisson distribution in time as in the colinear studies, and that a similar spatial distribution exists over the emission region of the LMIS. Such a treatment is far too sophisticated for use with the simple two particle system and will be omitted. However, it may be noted that qualitative agreement with the experimental data of Figure 41 is obtained with the pairwise model. From the data of Figure 41 showing experimental angular broadening for gallium, indium and bismuth as a function of current, a dependence of $\Delta\theta \propto I^{1/4}$ is obtained. The SOC model predicts that $\Delta\theta$ does increase with current.

6.5 Summary

In summary, a spherical model for the emitter shape together with the limitations of single file emission and pairwise interactions gives good qualitative agreement with experiment for the current and mass dependence of the energy spread in electron and ion beams.

The SOC model provides quantitative agreement with experimental energy spread magnitudes. By incorporating this emitter shape into a more general electron/ion optical program it is expected that the dependencies on emitter radius and field strength, as well as the current and mass relationships, can be brought into agreement with experiment.

The pairwise Coulomb interaction used throughout these studies provides a simple mechanism for elucidating the observed energy shift

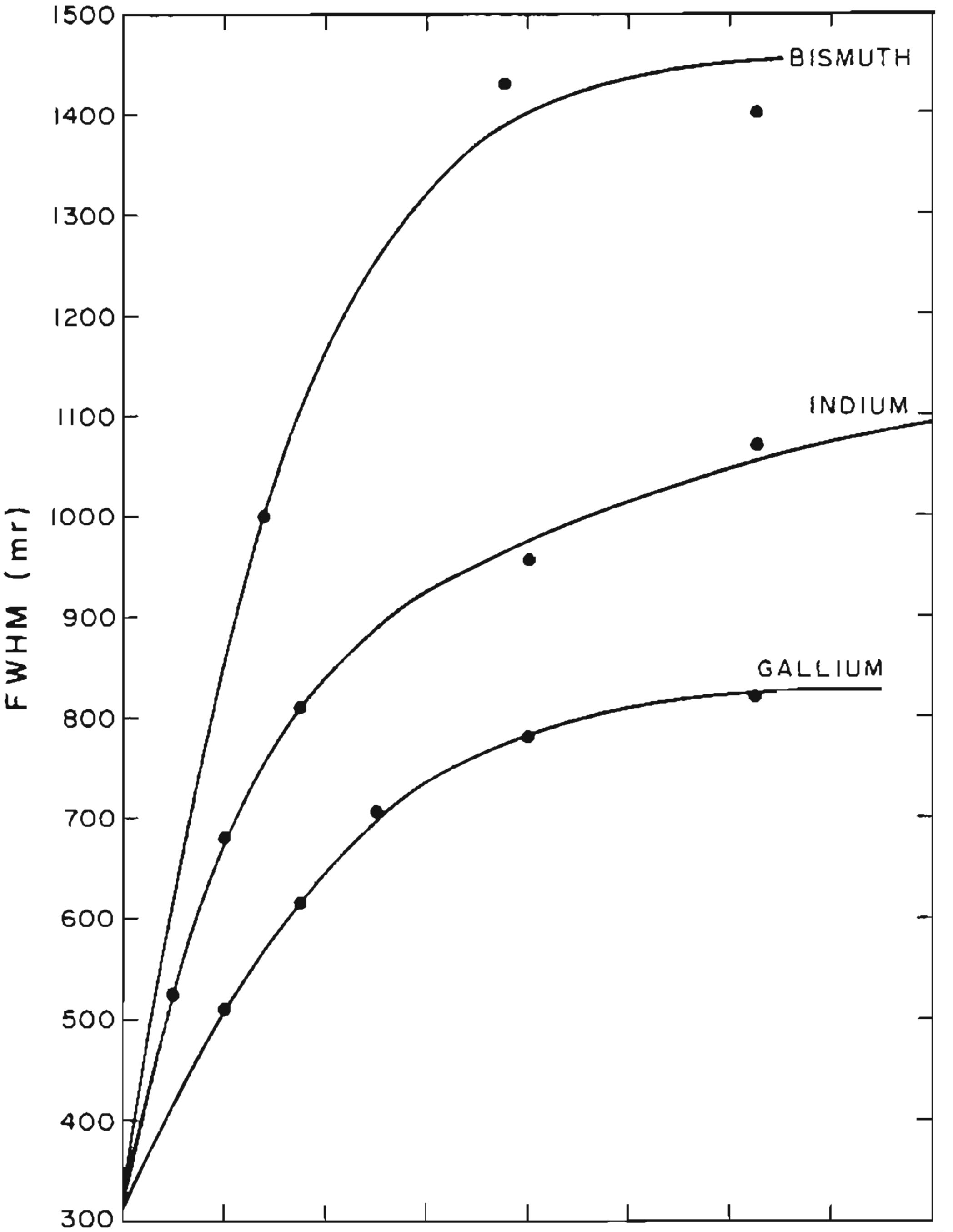

Figure 41. Experimental Angular Spread vs. Mass. Experimental values of the FWHM of the angular beam spread for gallium, indium and bismuth LMIS are plotted as a function of current.

phenomenon observed in LMIS beams. The shift in the peak of the energy distributions observed in LMIS emission is entirely the result of the relaxation of the initial Coulomb potential energy between pairs of ions into kinetic energy.

The Coulomb interaction also provides a mechanism for the angular beam spreading observed in electron and ion beams. The energy spread arises from the radial component of the Coulomb repulsion force between pairs of particles. The angular spread arises from the lateral component of the same force.

References

1. V. E. Krohn and G. R. Ringo, Appl. Phys. Lett. 27, 479 (1975).
2. R. Clampitt and D. K. Jeffries, Nucl. Instru. Meth. 149, 739 (1978).
3. L. W. Swanson, G. A. Schwind and A. E. Bell, J. Appl. Phys. 51, 3453 (1980).
4. A. Dixon, C. Colliex, R. Ohana, P. Sudraud and J. Van de Walle, Surf. Sci. Letters. 108, L424 (1981).
5. G. A. Massey, M. D. Jones and B. P. P.ummer, J. Appl. Phys. 52, 3780 (1981).
6. A. E. Bell and L. W. Swanson, Phys. Rev. B 19, 3353 (1979).
7. R. H. Fowler and L. W. Nordheim, Proc. R. Soc. London A 119, 173 (1928).
8. R. H. Good and E. W. Müller, Handb. Phys. 21, 176 (1956).
9. J. W. Gadzuk and E. W. Plummer, Rev. Mod. Phys. 45, 487 (1973).
10. N. Froman and P.O. Froman, JWKB Approximation: Contributions to the Theory (North-Holland, Amsterdam, 1965).
11. E. C. Kemble, The Fundamental Principles of Quantum Mechanics (McGraw-Hill, New York, 1937), p. 100.
12. R. Stratton, Phys. Rev. 135, A794 (1964).
13. E. W. Plummer and R. D. Young, Phys. Rev. B 1, 2088 (1970).
14. P. H. Cutler and J. J. Gibbons, Phys. Rev. 111, 394 (1958).
15. I. J. D'Haenens and E. A. Coomes, Phys. Rev. Lett. 17, 516 (1966).
16. H. F. Gray, Phys. Rev. B 1, 2842 (1970).
17. R. D. Young, Phys. Rev 113, 110 (1959).
18. R. D. Young and E. W. Müller, Phys. Rev. 113, 115 (1959).

19. L. W. Swanson and L. C. Crouser, Phys. Rev. Lett. 19, 1179 (1967); Phys. Rev. 163, 622 (1967).

20. A. van Oöstrom, Phillips Res. Rep. Suppl. 11, 102 (1966).

21. R. D. Young and C. E. Kuyatt, Rev. Sci. Instru. 39, 1477 (1968).

22. C. Lea and R. Gomer, J. Chem. Phys. 54, 3349 (1971).

23. H. Börsch, Z. Phys. 139, 115 (1954).

24. J. A. Simpson and C. E. Kuyatt, J. Appl. Phys. 37, 3805 (1966).

25. A. H. Beck and C. E. Maloney, Brit. J. Appl. Phys. 18, 845 (1967).

26. T. Ichinokawa, Jap. J. Appl. Phys. 8, 137, (1969).

27. K. H. Löffler, Z. angew. Phys. 27, 145 (1969).

28. C. Lea and R. Gomer, Phys. REv. Lett. 25, 804 (1970).

29. J. W. Gadzuk and E. W. Plummer, Phys. Rev. Lett. 26, 92 (1971).

30. J. W. Gadzuk and E. W. Plummer, Phys. Rev. B 3, 2125 (1971).

31. K. Kawasaki, K. Sensaki, Y. Kumashiro and A. Okada, Surf. Sci. 62, 313 (1977). .

32. J. E. Wolfe, private communication (1977).

33. M. Essig and J. Geiger, Appl. Phys. 25, 115 (1981).

34. R. L. Seliger, J. W. Ward, V. Wang and R. L. Kubena, Appl. Phys. Lett. 34, 310 (1979).

35. L. W. Swanson, G. A. Schwind, A. E. Bell and J. E. Brady, J. Vac. Sci. Technol. 16, 1864 (1979).

36. A. E. Bell, G. A. Schwind and L. W. Swanson, J. Appl. Phys. 53, 4602 (1982).

37. T. E. Fischer, 30th Annual Phys. Elec. Conf., Milwaukee WI (1970).

38. J. W. Gadzuk and A. A. Lucas, Phys. Rev. B 7, 4770 (1973).
39. B. Zimmermann, Adv. Elec. Elec. Phys. 29, 257 (1970).
40. W. Knauer, Optik 54, 211 (1979).
41. M. Fischer, J. Appl. Phys. 41, 3615 (1970).
42. A. V. Crewe, Optik 50, 205 (1978).
43. A. V. Crewe, Optik 52, 337 (1978/1979).
44. A. B. El-Kareh and M. A. Smither, J. Appl. Phys. 50, 5596 (1979).
45. T. Groves, D. L. Hammond and H. Kuo, Proc. 15th Symp. on Elec. Ion and Laser Beam Technol., Boston MA, 1689 (1979).
46. E. DeChambost and C. Hennion, Optik 55, 357 (1980).
47. H. Rose and R. Spehr, Optik 57, 339 (1980).
48. W. Knauer, Optik 59, 335 (1981).
49. M. A. Gesley, D. L. Larson, L. W. Swanson and C. H. Hinrichs, Proc. SPIE Int. Soc. Opt. Eng. 471, 66 (1984).
50. W. R. Smythe, Static and Dynamic Electricity (McGraw-Hill, New York, 1939), p. 205.
51. A. Ralston and H. S. Wilf, eds., Mathematical Methods for Digital Computers (Wiley, New York, 1967), p. 110.
52. R. Hesse, U. Littmark and P. Staib, Appl. Phys. 11, 233 (1976).
53. H. Spath, Spline Algorithms for the Construction of Smooth Curves and Functions (Oldenbourg Verlag, Munich, 1973).
54. J. C. Weisner and T. E. Everhart, J. Appl. Phys. 44, 2140 (1973).

APPENDIX

This appendix provides a function flow diagram for the Runge-Kutta trajectory program which generates data for the pairwise coulomb interactions.

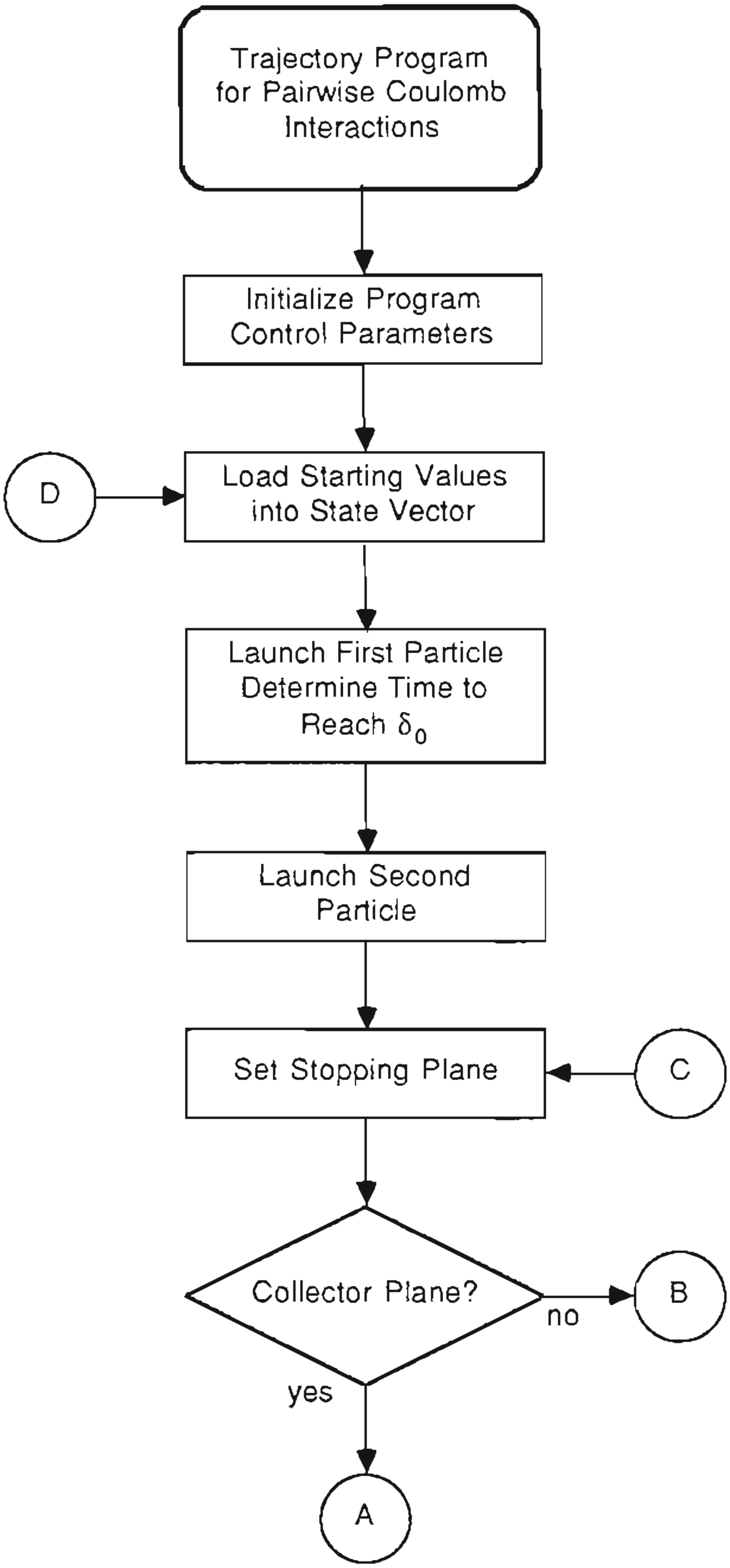
Trajectory Program for Pairwise Coulomb Interactions
Initialize Program Control Parameters
D
Load Starting Values into State Vector
Launch First Particle Determine Time to Reach δ_0
Launch Second Particle
Set Stopping Plane
C
Collector Plane?
no
B
yes
A

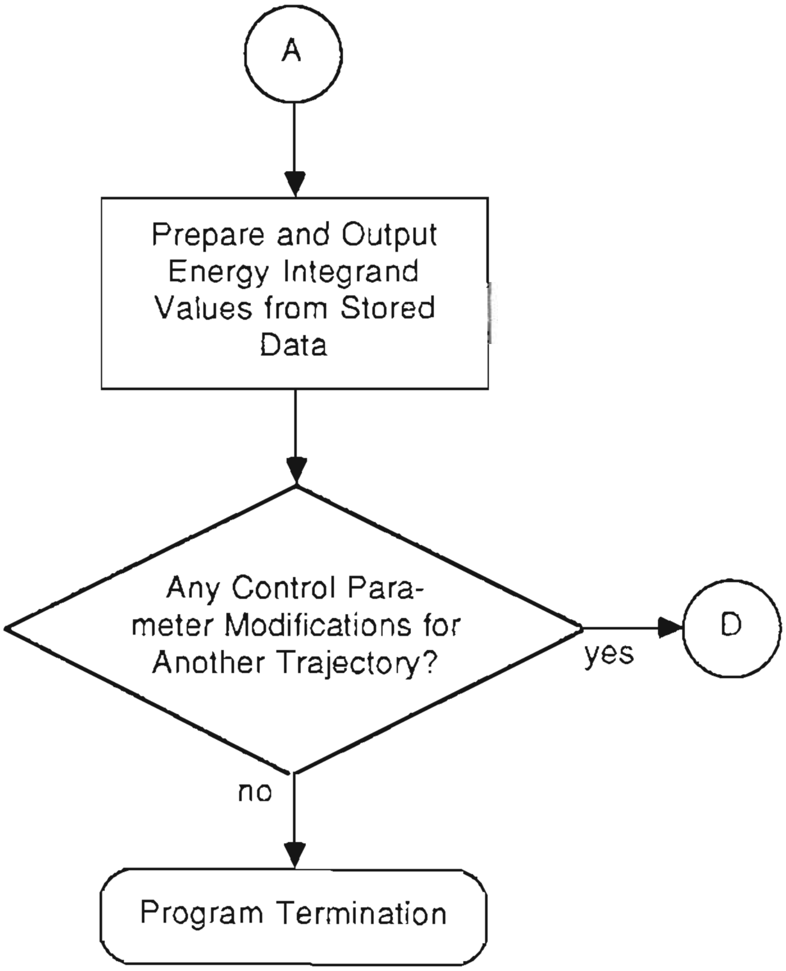
A
Prepare and Output Energy Integrand Values from Stored Data
Any Control Parameter Modifications for Another Trajectory?
yes
D
no
Program Termination

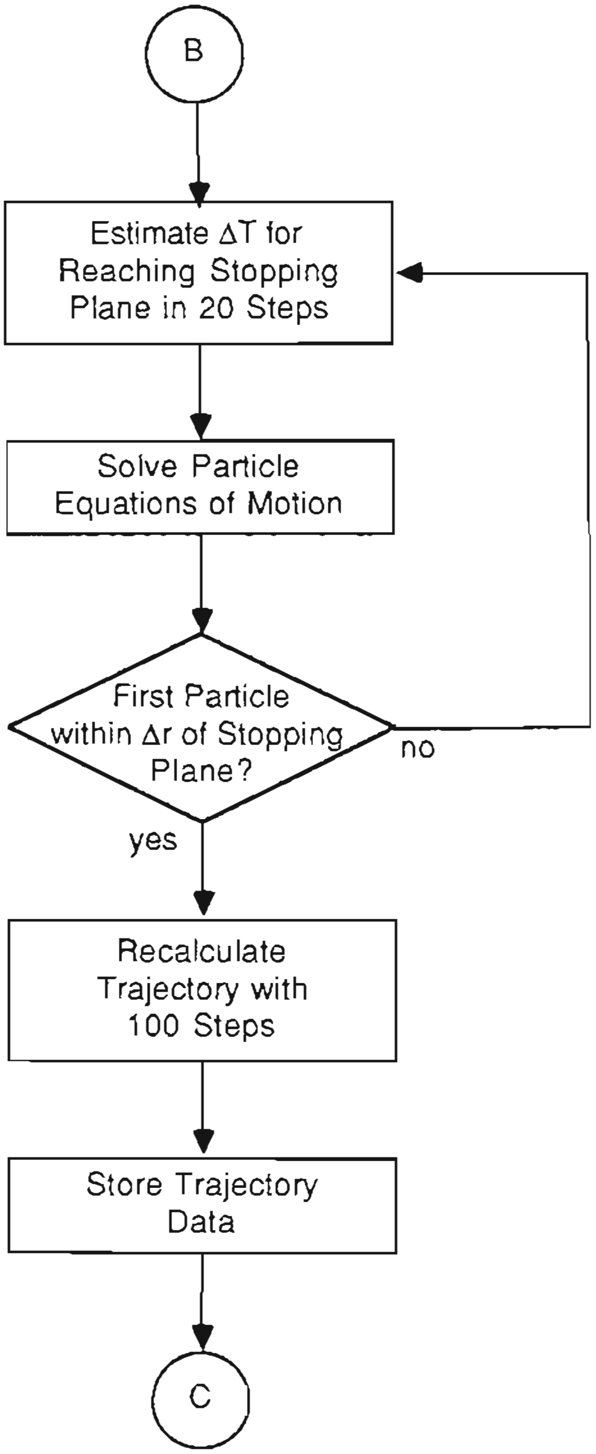
B
Estimate ΔT for Reaching Stopping Plane in 20 Steps
Solve Particle Equations of Motion
First Particle within Δr of Stopping Plane?
no
yes
Recalculate Trajectory with 100 Steps
Store Trajectory Data
C

BIOGRAPHICAL NOTE

The author was born November 6, 1953 in Jamestown, New York, and lived in Sinclairville, New York throughout his grammar and high school years. He graduated in 1971 from Cassadaga Valley Central School as salutatorian. He attended the State University College of Arts and Science at Plattsburgh, New York, where he received a Bachelor of Arts degree in May, 1975 where he was named a Hudson Scholar.

In September, 1975 he began graduate studies at the Oregon Graduate Center, which were continued until August, 1982 when he accepted a position as Staff Scientist at Electron Beam Corporation in San Diego, California. In November, 1984 the author accepted a position as Senior Engineer at the Space Systems Division of General Dynamics where he is presently employed. He completed the requirements for the degree Doctor of Philosophy in July, 1986.

The author has been married seven years to the former Lori Ann Phipps and they have two children, Linnea Kristen, age 3, and Ingebritt Elin, age 1.